Multi-modality imaging of atherosclerotic plaque using optical coherence tomography

Edouard Gerbaud

▶ **To cite this version:**

Edouard Gerbaud. Multi-modality imaging of atherosclerotic plaque using optical coherence tomography. Bioengineering. Université de Bordeaux, 2016. English. NNT : 2016BORD0132 . tel-01394901

HAL Id: tel-01394901
https://theses.hal.science/tel-01394901

Submitted on 10 Nov 2016

HAL is a multi-disciplinary open access archive for the deposit and dissemination of scientific research documents, whether they are published or not. The documents may come from teaching and research institutions in France or abroad, or from public or private research centers.

L'archive ouverte pluridisciplinaire **HAL**, est destinée au dépôt et à la diffusion de documents scientifiques de niveau recherche, publiés ou non, émanant des établissements d'enseignement et de recherche français ou étrangers, des laboratoires publics ou privés.

université de BORDEAUX

THÈSE
pour le
DOCTORAT DE L'UNIVERSITÉ DE BORDEAUX

Ecole doctorale: Sciences de la Vie et de la Santé
Mention: Bioimagerie

Presented and publicy defended on September the 15th 2016

By

Edouard Gerbaud

MULTI-MODALITY IMAGING OF ATHEROSCLEROTIC PLAQUE USING OPTICAL COHERENCE TOMOGRAPHY

Members of the Jury 15/09/ 2016

Mr. le Professeur Roger MARTHAN, CHU Bordeaux	Président
Mr. le Professeur Pascal MOTREFF, CHU Clermont-Ferrand	Rapporteur
Mr. le Professeur Nicolas MENEVEAU, CHU Besançon	Rapporteur
Mr. le Professeur Michel MONTAUDON, CHU Bordeaux	Examinateur
Mr. le Professeur Pierre DOS SANTOS, CHU de Bordeaux	Directeur de Thèse
Mr. le Professeur Guillermo J. TEARNEY, Harvard Medical School	Directeur de Thèse
Mr. le Professeur Pierre COSTE, CHU Bordeaux	Membre invité

Titre : Imagerie multi-modalité en tomographie par cohérence optique de la plaque d'athérosclérose

Résumé :

Les technologies d'imagerie intravasculaire c'est à dire l'échographie endo-coronaire (IVUS) et la tomographie par cohérence optique (IV-OCT) sont des outils précieux pour aider au diagnostic de la plaque d'athérosclérose et guider les gestes thérapeutiques.
Le chapitre 1 présente les inconvénients de la coronarographie dans la pratique clinique. Dans plusieurs circonstances, l'IVUS et l'OCT ont clairement une valeur supplémentaire quand ils sont utilisés comme un outil diagnostique en cas d'ambiguïtés angiographiques. Nous avons récemment rapporté la première observation utilisant l'OCT pour décrire une dissection coronaire d'une branche septale perforante responsable d'un infarctus du myocarde.
Le chapitre 2 porte sur la reproductibilité de l'OCT entre différents instituts concernant de nombreux paramètres qualitatifs et quantitatifs de la plaque d'athérome. Le but de notre étude était d'étudier en plus de la reproductibilité inter- et intra-observateur, la variabilité inter-instituts de l'OCT concernant les mesures quantitatives et qualitatives et de la comparer à celle de l'IVUS. Dans ce travail, nous avons observé que, dans la mesure de la surface de la lumière endocoronaire, des diamètres minimum et maximum de cette même lumière endocoronaire, de la surface endo-luminale du stent, des diamètres minimum et maximum endo-luminaux du stent, par des analystes provenant de 2 laboratoires différents, la reproductibilité inter-instituts de l'OCT était nettement supérieure à celle de l'IVUS.
Le Chapitre 3 présente 2 nouvelles technologies robustes d'imagerie intravasculaire hybrides développées dans le laboratoire du Professeur Guillermo J. Tearney: l'OCT couplée à la spectroscopie dans le proche infra-rouge (OFDI-NIRS) et l'OCT couplée à l'autofluorescence dans le proche infra-rouge (OFDI-NIRAF). Les premières procédures d'OFDI-NIRS chez l'homme sont prévues dans un avenir proche. Les premières procédures chez l'homme ont été réalisées chez 12 patients porteurs d'un angor stable entre Juillet 2014 et Janvier 2015. Les résultats de cette étude pilote ont montré que le signal d'autofluorescence recueilli (NIRAF) a été focalement trés élevé dans des endroits de la plaque d'athérome où la plupart des phénotypes morphologiques en OCT d'une plaque à haut risque de rupture étaient évidents. Les substrats biochimiques de ce signal d'autofluorescence (NIRAF) sont encore à élucider.

Mots clés : athéroclérose, plaque vulnérable, imagerie intracoronaire, échographie endocoronaire, tomographie par cohérence optique, imagerie hybride, spectroscopie dans le proche infra-rouge, autofluorescence dans le proche infra-rouge.

Title : Multi-modality imaging of atherosclerotic plaque using optical coherence tomography

Abstract :

Intravascular imaging technologies i.e. IVUS and IV-OCT are valuable tools for intervention guidance and diagnostic plaque imaging.

Chapter 1 introduces the drawbacks of coronary angiography in the clinical practice. In several circumstances, IVUS and IV-OCT have clearly an additional value when they are used as a diagnosis tool in case of angiographic ambiguities. We recently reported the first observation using IV-OCT to describe a coronary dissection of a septal perforating branch causing AMI.

Chapter 2 focuses on the inter-institute reliability of IV-OCT to determine qualitative and quantitative parameters of atherosclerotic plaque. The purpose of our study was to investigate further inter- and intra-observer reproducibility, the inter-institute variability for IV-OCT (OFDI) quantitative and qualitative measurements vs. IVUS measurements using published consensus document definitions. In our work, we observed that in the measurement of lumen CSA, maximum and minimum lumen diameters, stent CSA, maximum and minimum stent diameters by analysts from 2 different laboratories, inter-institute reproducibility of OFDI was found to be more consistent than IVUS.

Chapter 3 present 2 new robust hybrid intravascular imaging technologies developed in Dr. Tearney's laboratory i.e. OFDI-NIRS and OFDI-NIRAF, which may offer supplementary criteria for plaque vulnerability. First-in-human OFDI-NIRS imaging procedures are anticipated in the near future. First-in-human OFDI-NIRAF imaging procedures have been performed in a first pioneering series of 12 stable patients between July 2014 and January 2015. Findings of this pilot study showed that NIRAF was focally elevated in plaque locations where most high-risk morphologic phenotypes were evident. The biochemical substrates of the NIRAF signal still have to be elucidated.

Keywords : atheroclerosis, vulnerable plaque, intracoronary imaging, intravascular ultrasound studies, optical coherence tomography, hybrid imaging, near-infrared spectroscopy, near-infrared autofluorescence.

Les technologies d'imagerie intravasculaire c'est à dire l'échographie endo-coronaire (IVUS) et la tomographie par cohérence optique (IV-OCT) sont des outils précieux pour aider au diagnostic de la plaque d'athérosclérose et guider les gestes thérapeutiques.
Le chapitre 1 présente les inconvénients de la coronarographie dans la pratique clinique. L'IVUS et l'OCT sont des technologies d'imagerie intra-coronaire qui se sont développées pour guider l'angioplastie coronaire percutanée, étudier l'évolution de la plaque d'athérosclérose et apprécier le remodelage vasculaire des artères coronaires. Dans plusieurs circonstances, l'IVUS et l'OCT ont clairement une valeur supplémentaire quand ils sont utilisés comme un outil diagnostique en cas d'ambiguïtés angiographiques. Nous avons récemment rapporté la première observation utilisant l'OCT pour décrire une dissection coronaire d'une branche septale perforante responsable d'un infarctus du myocarde.
Le chapitre 2 porte sur la reproductibilité de l'OCT entre différents instituts concernant de nombreux paramètres qualitatifs et quantitatifs de la plaque d'athérome. Les reproductibilités inter- et intra-observateur ont déjà été largement étudiées dans de nombreuses études. Il existe des documents de consensus regroupant de nombreux experts internationaux qui font référence dans ce domaine notamment pour les méthodes de mesure de la plaque d'athérome intracoronaire. Le but de notre étude était d'étudier en plus de la reproductibilité inter- et intra-observateur, la variabilité inter-instituts de l'OCT concernant les mesures quantitatives et qualitatives et de la comparer à celle de l'IVUS. Dans ce travail, nous avons observé que, dans la mesure de la surface de la lumière endocoronaire, des diamètres minimum et maximum de cette même lumière endocoronaire, de la surface endo-luminale du stent, des diamètres minimum et maximum endo-luminaux du stent, par des analystes provenant de 2 laboratoires différents, la reproductibilité inter-instituts de l'OCT était nettement supérieure à celle de l'IVUS.
Le Chapitre 3 présente 2 nouvelles technologies robustes d'imagerie intravasculaire hybrides développées dans le laboratoire du Professeur Guillermo J. Tearney: l'OCT couplée à la spectroscopie dans le proche infra-rouge (OFDI-NIRS) et l'OCT couplée à l'autofluorescence dans le proche infra-rouge (OFDI-NIRAF). Un cathéter d'imagerie hybride intracoronaire OFDI-NIRS a déjà été expérimenté et évalué sur des artères coronaires cadavériques. Les premières procédures d'OFDI-NIRS chez l'homme sont prévues dans un avenir proche. Les premières procédures d'OFDI-NIRAF chez l'homme ont été réalisées chez 12 patients porteurs d'un angor stable entre Juillet 2014 et Janvier 2015 au Massachusetts General Hospital (Boston, Harvard Medical School, Etats-Unis). Les résultats de cette étude pilote prometteuse ont montré que le signal d'autofluorescence recueilli (NIRAF) a été focalement trés élevé dans des endroits de la plaque d'athérome où la plupart des phénotypes morphologiques en OCT d'une plaque à haut risque de rupture étaient évidents. Ces premières procédures d'imagerie hybride intracoronaire couplant l'OCT à une autre modalité

chez l’homme ont été simples à réaliser et aucun événement indésirable n’est survenu lors de leurs réalisations. Les substrats biochimiques de ce signal d’autofluorescence (NIRAF) sont encore à élucider. Différentes hypothèses ont été émises et sont en cours d’évaluation.

Mots clés : athéroclérose, plaque vulnérable, imagerie intracoronaire, échographie endocoronaire, tomographie par cohérence optique, imagerie hybride, spectroscopie dans le proche infra-rouge, autofluorescence dans le proche infra-rouge.

ACKNOWLEGEMENTS

To Professor Guillermo J. Tearney,
I want to give you my sincere gratitude. Thank you for giving me the opportunity to join your team in the Wellman Center for Photomedicine. Thank you for accepting to supervise my PhD and for checking my manuscripts down to details. Your inlimited knowledge can always inspire me which direction to go. Thank you for taking the time to join us in Bordeaux for my PhD defense. I hope we will continue to collaborate in the future.

A Monsieur le Professeur Pierre Domingues Dos Santos,
Pour avoir accepté d'être directeur de ce travail et m'avoir accueilli en tant que chef de clinique dans ton service hospitalier. Merci de m'avoir toujours fait confiance et de m'avoir transmis ta passion pour l'innovation et la recherche.

A Monsieur le Professeur Roger Marthan,
Merci pour l'honneur que vous me faites d'avoir accepté de présider le jury de cette thèse. Merci de m'avoir donné l'opportunité de réaliser cette aventure américaine. J'espère continuer avec votre aide à tisser des liens étroits entre le Centre de Recherche Cardio-thoracique bordelais et le Wellman Center for Photomedicine à Boston.

A Monsieur le Professeur Pascal Motreff,
Merci pour l'honneur que vous me faites de juger ce travail en y apportant votre expérience et votre grande expertise en tomographie par cohérence optique. J'espère avoir l'occasion de collaborer activement avec votre équipe à Clermont-Ferrand et avec vous pour vous aider à faire vivre nos sociétés savantes. Veuillez trouver ici le témoignage de ma profonde admiration.

A Monsieur le Professeur Nicolas Méneveau,
Merci pour l'honneur que vous me faites de juger ce travail en y apportant votre grande expertise en cardiologie interventionnelle. J'espère avoir l'occasion de collaborer activement avec votre équipe à Besançon sur de nouveaux projets multicentriques dans le domaine de l'imagerie intracoronaire. Veuillez trouver ici le témoignage de ma profonde admiration.

ACKNOWLEGEMENTS

A Monsieur le Professeur Michel Montaudon,
Merci pour l'honneur que tu me fais de juger ce travail. Merci pour ces quelques années d'intense collaboration en imagerie cardio-vasculaire qui ont permis le développement de l'IRM cardiaque et de réaliser de beaux projets de recherche clinique. Merci pour ton soutien constant et tes conseils méthodologiques inestimables. J'espère pouvoir à l'avenir continuer à travailler avec toi et ton équipe.

A Monsieur le Professeur Pierre Coste,
Merci pour l'honneur que vous me faites de juger ce travail en y apportant votre grande expérience en cardiologie interventionnelle. Merci pour votre enseignement quotidien en salle de cathétérisme. Merci de m'avoir fait confiance en acceptant que je rejoigne votre équipe. Avec votre soutien, j'espère pouvoir continuer à l'avenir mon activité de recherche au sein de votre service. Veuillez trouver ici le témoignage de ma sincère gratitude.

Aux membres du Tearney lab et du Wellman Center for Photomedicine qui m'ont accueilli avec bienveillance et avec qui j'ai vécu une année riche en rencontres et découvertes. Au Docteur Giovanni J. Ughi pour toutes ces heures passées sur le prototype OFDI-NIRAF. Au Docteur Gabriela Apiou pour ses encouragements et ses conseils. Au Docteur Mireille Rosenberg pour son calme, sa rigueur et sa gentillesse.
Au Docteur Christine P. Hendon (Columbia University) pour son accueil à New York. Aux Docteurs Akiko Maehara (Columbia Research Foundation) et Atsushi Tanaka (Wakayama Medical University) pour leur efficace collaboration.

Aux membres du Centre de Recherche Cardio-thoracique pour leur accueil au début de ma thèse.

A l'équipe du Service des Soins intensifs de Cardiologie et du Plateau de Cardiologie Interventionnelle pour leur amical soutien.

A la Fédération Française de Cardiologie et à la Commission franco-américaine Fullbright pour le financement qu'ils m'ont apporté pour interrompre mon activité clinique et me permettre de réaliser une année de recherche à Boston.

ACKNOWLEGEMENTS

A mon épouse qui m'a encouragé en permanence. Cela est certain; ce travail n'aurait pas pu se réaliser sans toi.

A ma fille qui nous a accompagné pendant notre séjour américain et qui a sans aucun doute maintenant « le meilleur accent » de la famille,
A ma mère : tu es toujours là à mes côtés,
A mon père,
A mon parrain : je pense que tu aurais aimé être présent le jour de ma soutenance,

A celles et ceux qui sont venus partager un moment à Boston.

CONTENTS

CONTENTS

List of abbreviations

LDL: low density lipoprotein

MMPs: metalloproteinases

ESS: endothelial shear stress

IVUS: intravascular ultrasound studies

NURD: non uniform rotational distortion

OCT: optical coherence tomography

IVOCT: intravascular optical coherence tomography

OFDI: optical frequency domain imaging

FD-OCT: frequency domain optical coherence tomography

DES: drug eluting stent

SCAD: spontaneous coronary artery dissection

ACS: acute coronary syndrome

NSTEMI: non-ST segment elevation myocardial infarction

STEMI: ST segment elevation myocardial infarction

AMI: acute myocardial infarction

TIMI: Thrombolysis In Myocardial Infarction

PCI: percutaneous coronary intervention

CMR : cardiac magnetic resonance

LGE : late gadolinium enhancement

CSA: cross section area

EEM: external elastic membrane

IEM: internal elastic membrane

ICC: intra-class coefficient correlation

TCFA: thin-cap fibroatheroma

ThCFA: thick-cap fibroatheroma

RCP: ruptured culprit plaque

RNCP: ruptured nonculprit plaque

NIR: near-infrared

NIRS: near-infrared spectroscopy

SOCT: spectroscopic optical coherence tomography

OCT-NIRS: optical coherence tomography - near-infrared spectroscopy

ABBREVIATIONS

IVUS-NIRS: intravascular ultrasound – near-infrared spectroscopy

LCBI: lipid core burden index

NIRF: near-infrared fluorescence

NIRAF: near-infrared autofluorescence

OCT- NIRAF: optical coherence tomography - near-infrared autofluorescence

NSD: normalized standard deviation

SMF: single-mode fiber

MMF: multi-mode fiber

DCF: double clad fiber

1. Natural history of atherosclerotic plaque

1.1 Interaction between several factors including inflammation and biomechanical forces in the development of atherosclerotic plaque

Atherosclerosis has one of the longest incubation periods among the human diseases [1]. The description of its origin and progression is documented predominantly from observations of the arteries of persons autopsied at various ages. It is based on the assumption that any type of lesion occurring in one age group (for example, fatty streaks in adolescents) may be transformed into another type of lesion occurring at the similar anatomic site in an older age group [2]. Atherosclerosis is a chronic inflammatory process resulting from interactions between plasma lipoproteins, cellular components (monocyte, macrophages, T lymphocytes, endothelial cells and smooth muscle cells) and the extracellular matrix of the arterial wall.

Histologically, atherosclerotic lesions from the early-stage (fatty streak) to more complicated lesions present all the features of chronic inflammation. Initially, the elevation of plasma atherogenic lipoproteins i.e. oxidized low density lipoprotein (LDL), remnant lipoprotein (β-VLDL) and lipoprotein (a) may lead to their deposition in the intima [3]. Fatty streak development is characterized by the accumulation of lipid-loaded cells underlying the endothelium of large arteries. These lipid-loaded cells mainly originate from blood-born monocytes subsequently differentiated into macrophages. Initially their adherence to endothelial cells is triggered by a number of adhesion molecules on endothelial cells, such as vascular cell adhesion molecule-1 (VCAM-1), intra-cellular adhesion molecule-1 (ICAM-1), P-selectin and E-selectin [4,5]. Expression of adhesion molecules is highly up-regulated by the elevation of the levels of atherogenic lipoproteins [(oxidized LDL and lipoprotein (a)]. After monocytes and T lymphocytes bind to the surface of the arterial wall, they migrate into the subendothelial space, where they differentiate and are transformed into macrophages and foam cells. This migration is induced by several chemoattractants such as cytokines (monocyte chemoattractant protein (MCP-1), interleukin-1 (IL-1), and tumor necrosis factor-alpha (TNF-∝). Among all the chemoattractants reported thus far, MCP-1 and Lyso-PC (a component of oxidized LDL) may be the most important chemoattractants in the atherosclerotic lesions [6,7]. Monocytes may differentiate into macrophages under the action of granulocyte macrophage colony-stimulating factor (GM-CSF). Macrophages may take up

deposited atherogenic lipoproteins through scavenger receptors and be transformed into foam cells. In addition to acting as a chemoattractant for monocytes, oxidized LDL can inhibit macrophage mobility. Close interactions among foam cells, T lymphocytes and smooth muscle cells together with diverse cytokines and other biological effects may take place, ultimately deciding the fate of the lesions. Basically, atherosclerotic plaque contains a lipid or necrotic core covered by a fibrotic cap consisting of a mixture of smooth muscle cells and extracellular matrix. The base of the lesion called “the shoulder” contains a number of macrophages-derived foam cells and T lymphocytes. Two kinds of common plaque are usually differentiated: the stable plaque and the unstable or vulnerable plaque. Schematically, the stable plaque is composed of a small lipid core and covered by a thick fibromuscular cap with more smooth muscle cells and extracellular matrix, whereas the vulnerable plaque is composed of a large necrotic core covered by a thin cap, and a large number of inflammatory cells, especially at the shoulder may be present. The mechanism of plaque rupture is explained by the accumulation of macrophages and T lymphocytes who may play a critical role in this regard because macrophages can produce matrix metalloproteinases (MMPs), which may thin or destruct the cap and then potentiate the rupture [8,9].

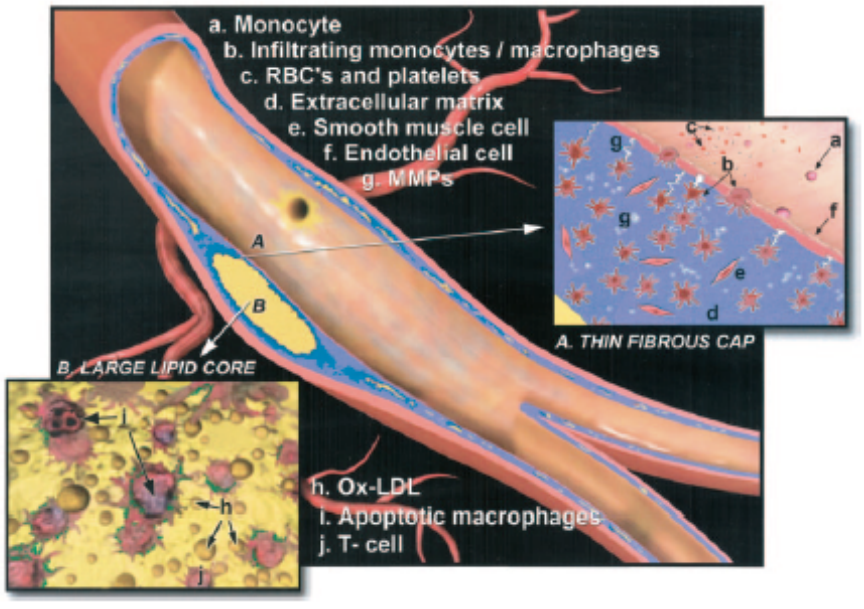

Schematic figure illustrating a common type of atherosclerotic plaque. Adapted from Naghavi M. et al. Circulation 2003; 108:1664-1672.

It is now well recognized that at least three subtypes of macrophages can be found in atherosclerotic lesions: M1, the most common form, is a pro-inflammatory macrophage subtype, activated by cytokines secreted by T cells, while M2 seems to play an anti-inflammatory role, promoting tissue repair [10]. The activation of M1 macrophages is mediated by toll-like receptor-4 (TLR-4) [11]. A novel third atheroprotective macrophage phenotype, haemoglobin-stimulated macrophage (M(Hb)), induced by intraplaque haemorrhage, has also been isolated in atheromas [12]. Cumulative experimental and clinical evidence imply an important role of adaptive immunity in atherosclerosis progression and destabilization. Indeed, the cells of adaptive immunity, namely T and B lymphocytes, reside in atherosclerotic plaques. A novel link between cholesterol metabolism and local atherosclerotic plaque inflammation has also been proposed. It has recently been shown that phagocytosis of cholesterol crystals by human macrophages leads to a dose-dependent secretion of mature human pro-inflammatory cytokine interleukin (IL)-1, through an inflammasome-mediated pathway [13]. Moreover, cholesterol crystallization alone, due to shift in local plaque temperature, pH, and hydration status, has been proposed to cause plaque fissure and thrombosis through acute volume expansion [14]. Recent advances in higher resolution modalities such as micro-optical coherence tomography (mOCT) could detect in vivo such structures, shedding light in vulnerable plaque evolution [13]. Furthermore, in advanced atherosclerosis, inflammation and angiogenesis often co-exist. The new microvessels usually originate from the vasa vasorum in adventitia. Intra-plaque bleedings increase significantly the levels of free cholesterol and lead to rapid necrotic core expansion and plaque progression, increasing its vulnerability. Thus, an association between intra-plaque haemorrhage, cholesterol crystals, and inflammation has been established. In addition, microRNAs are small, non-coding post-transcriptional regulatory RNAs. They inversely regulate their target gene expression at the post-transcriptional level either by inhibiting translation or by causing degradation of the target messenger RNA. MicroRNAs seem to participate as post-transcriptional regulators in all stages of the inflamed atherosclerotic plaque formation, ending to its rupture. VCAM-1 expression by ECs, inflammatory activation of plaque macrophages in M1 phenotype, lipid accumulation in macrophages and foam cell

formation, oxLDL-induced lipid uptake through regulation of scavenger receptors, and macrophage apoptosis are only few of the processes regulated [15,16]. Biomechanical factors may be also implicated in the vulnerable plaque formation and rupture. Endothelial shear stress (ESS), the tangential force derived by the friction of the flowing blood on the endothelial surface, plays a key role in the pathobiology of atherogenesis, plaque formation, and plaque progression to vulnerability. Low ESS modulates the accumulation of lipids and neovascularization resulting to plaque volume expansion. In the setting of inflammation, low ESS increases the mRNA expression and activity of major elastolytic MMPs (MMP 2, 9, 12) and cathepsins (cathepsin K and S) relative to their endogenous inhibitors (TIMPs and cystatin C, respectively), thereby leading to internal elastic lamina fragmentation [17]. Through the fragmented internal elastic lamina, the inflammatory cells migrate into the media where they further promote matrix degradation and ultimately expansive remodelling, which is a key pathobiological feature of vulnerable plaque. Moreover, low ESS increases the expression and enzymatic activity of collagenolytic MMPs (MMP 1, 8, 13, and 14), which in turn degrade the collagen in fibrous cap. This effect in conjunction with the low shear-mediated smooth muscle cell apoptosis and reduction in smooth muscle cells and collagen synthesis leads to fibrous cap thinning [18]. A large multicentre clinical study investigated the role of ESS in the natural history of atherosclerosis. Five hundred patients with acute coronary syndrome (ACS) underwent three-vessel intravascular ultrasound studies (IVUS) examination and profiling of local ESS at baseline and at 6 months. This landmark study demonstrated that low baseline ESS is an independent predictor of plaque progression and expansive remodelling with lumen narrowing [19]. Data from optical coherence tomography (OCT) studies in man further elucidated the role of low ESS in plaque vulnerability. Those studies combined functional and morphological assessment of plaque using 3-dimension OCT and showed that low ESS is associated with inflammation, thin fibrous cap, large lipid core, and expansive remodelling, all of which are key pathobiological fingerprints of vulnerable plaque [20]. Local ESS is a major local factor that interplays with the vascular remodelling response, leading to plaque growth and potentially plaque rupture. Non-stenotic vulnerable plaques are exposed to low ESS, which perpetuates an ongoing vicious cycle of local inflammation, matrix degradation, and expansive remodelling leading to acute plaque disruption and thrombotic occlusion of the lumen in the setting of increased thombogenicity [21]. In contrast to non-stenotic vulnerable plaques, the stenotic vulnerable plaques create a heterogeneous local ESS environment

along their length, which involves low ESS in the upstream shoulders, high ESS at the neck of the plaque, and low/oscillatory ESS in the downstream shoulder. The majority of ruptures occur at the upstream shoulders of the plaque, whereas the downstream regions are more stable and therefore less prone to rupture [22]. Plaque rupture can also occur at the most stenotic part of the plaque likely as a result of local erosion in the setting of very high flow and ESS. However, the pathobiological association of high ESS with plaque erosion is not well investigated. Local wall stress is another major local haemodynamic factor that plays a key role in the pathobiology of plaque rupture [23]. Wall stress is proportional to blood pressure and inversely proportional to lumen stenosis. The highest wall stress typically occurs at the upstream shoulders of a stenotic plaque or within a non-stenotic plaque co-localizing with thin fibrous cap, increased macrophage density, and local microcalcifications. Collectively, the dynamic synergism among local haemodynamic factors (ESS and wall stress), plaque composition, and vascular remodelling is a key player in acute plaque disruption.

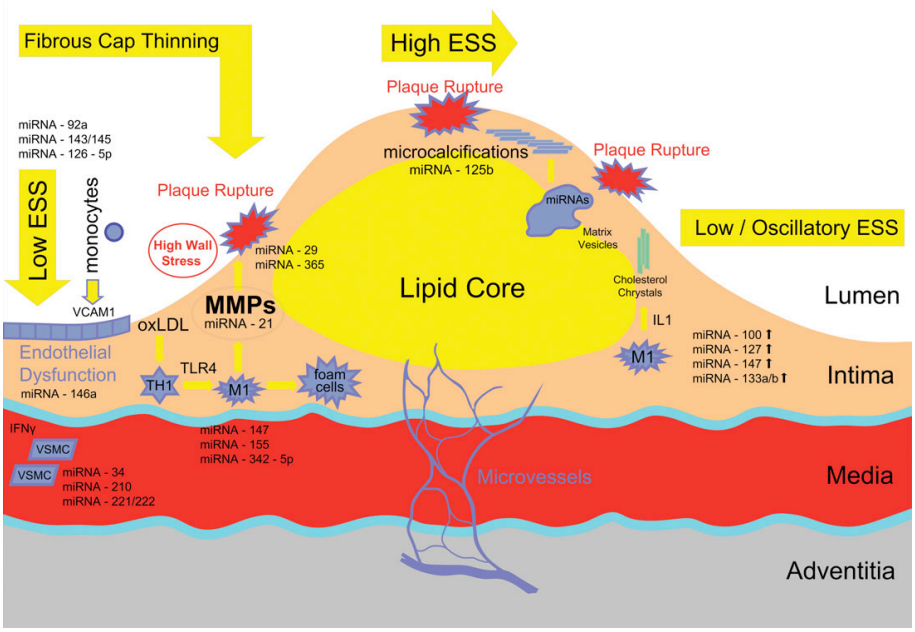

Scheme illustrating the interactions between biomechanical forces, inflammation, microcalcifications, cholesterol crystals, and microRNAs in high-risk plaque formation and rupture. Adapted from Toutouzas K. et al. European Heart Journal 2015; 36:3147–3154.

1.2 Classification of atherosclerotic plaque based on morphology

An initial classification of atherosclerotic plaque was published by the American Heart Association in the mid 1990s [24]. This classification was slightly modified in 2000 [25] and is nowadays always used in clinical practice and in research. Four types of lesion exist: nonatherosclerotic intimal lesions, progressive atherosclerotic lesions, lesions associated with acute thrombi and healed lesions.

In the nonatherosclerotic intimal lesions category, intimal thickening is characterized by the accumulation of smooth muscle cells in the absence of macrophage-derived foam cells, whereas intimal xantoma is composed of superficial accumulation of foam cells without a necrotic core, fibrous cap, or thrombosis.

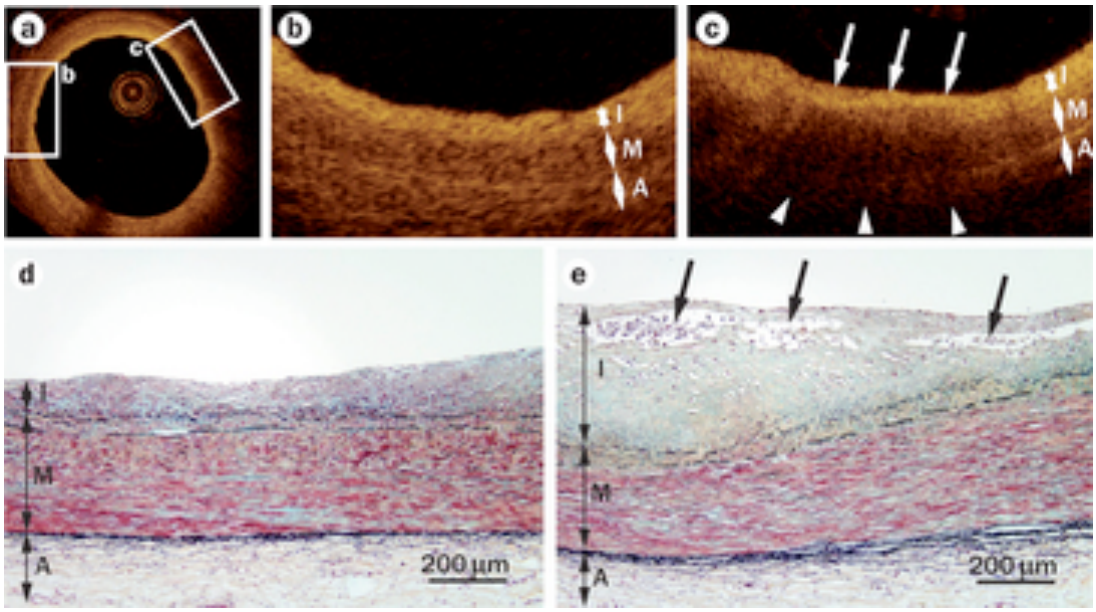

Intimal thickening and intimal xanthoma. **a** Low-power and **b, c** high-power ex vivo OCT images showing intimal thickening (panels a and b) and intimal xanthoma (panels a and c) in a human coronary artery. Three layers i.e. intima (I), media (M) and adventice (A) are apparent in the arterial wall. A focal signal-rich confluent punctate region (white arrows in panel c) is observed close to the luminal surface, which is accompanied by signal attenuation (white arrow heads in panel c). **d, e** Corresponding histological images showing intimal thickening without macrophages (panel d), and intimal xanthoma characterized by the presence of foamy macrophages (black arrows) within the thin neointima (panel e). Adapted from Otsuka F et al. Nat Rev Cardiol 2014; 11:379-389.

In the progressive atherosclerotic lesions category, 4 subtypes exist. First, pathological intimal thickening is characterized by a plaque rich in smooth muscle cells, with hyaluronan and proteoglycan matrix and focal accumulation of extracellular lipid.

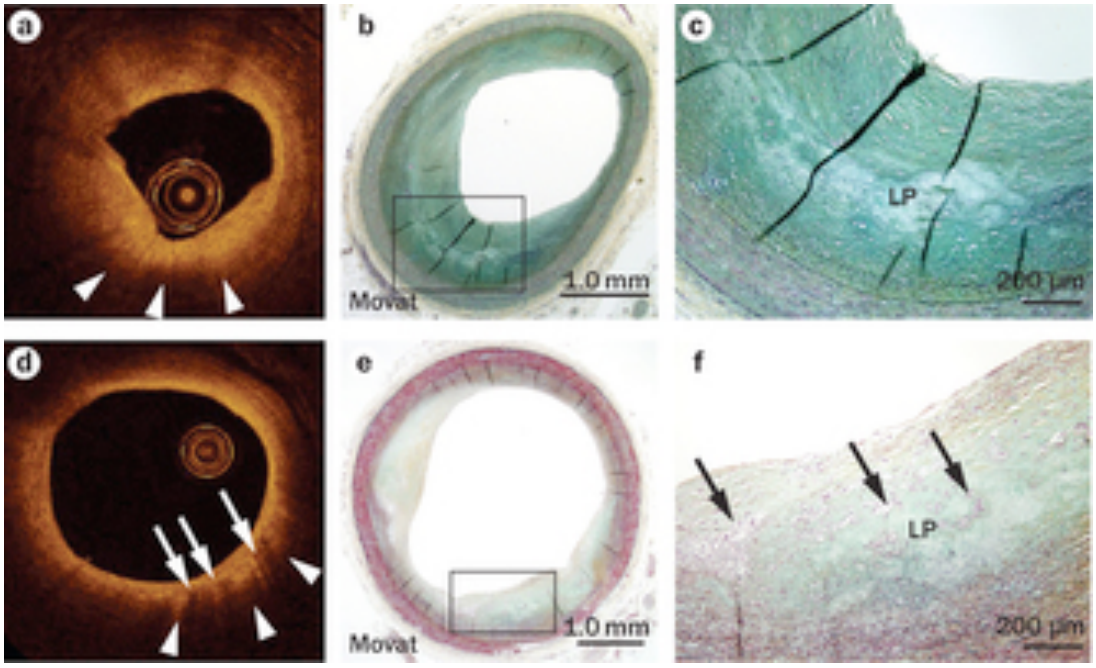

Pathological intimal thickening. **a-c** Images showing macrophage-poor pathological intimal thickening. **d-f** Images showing pathological intimal thickening containing macrophages. Focal signal-poor region with diffuse border (white arrow heads) in *ex-vivo* OCT images (panels a and d) correspond with the presence of LP in low-powered (panels b and e) and high-powered (panels c and f) images of histological sections of human coronary plaques (all sections are stained with Movat Pentachrome). Signal-rich confluent punctate area with attenuation is observed in the OCT image in panel d (white arrows), which corresponds with the presence of foamy macrophages in the histology in panel f (black arrows). Adapted from Otsuka F et al. Nat Rev Cardiol 2014; 11:379-389.

Second, fibroatheroma is composed of focal macrophage infiltration into areas of lipid pools with an overlying fibrous cap during early necrosis. During late necrosis, fibroatheroma present a loss of matrix and extensive cellular debris with an overlying fibrous cap.

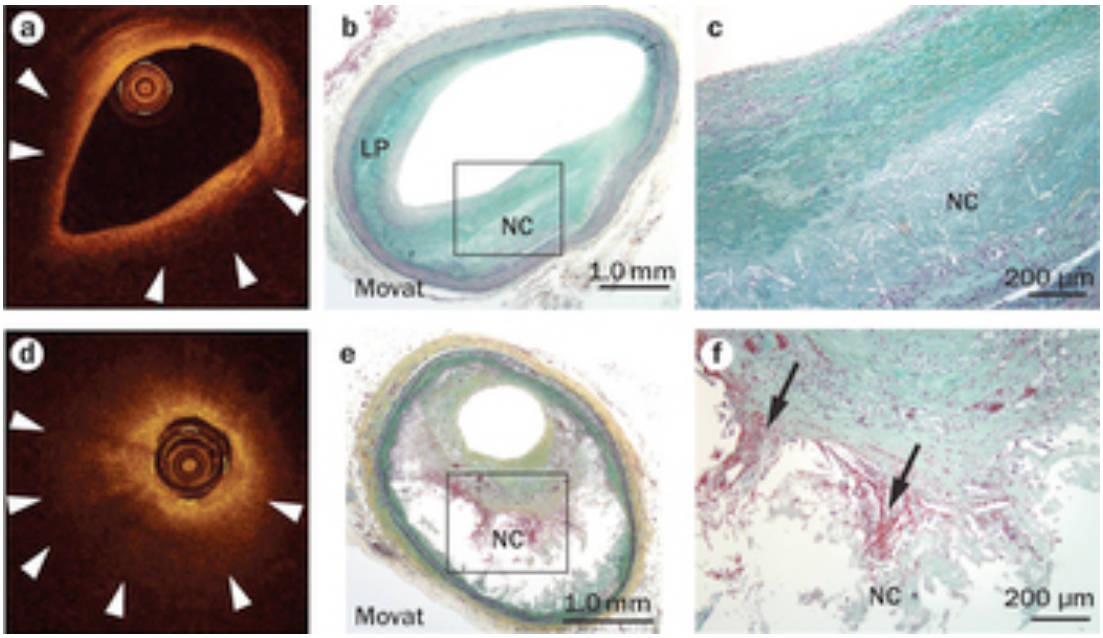

Fibroatheroma. **a-c** Images showing early fibroatheroma. **d-f** Images showing late fibroatheroma. Low backscattering, signal-poor regions with diffuse border (white arrow heads) in ex vivo optical coherence tomography images (panels a and d) correspond with the presence of lipid pool or necrotic core in low-powered (panel b and e) and high-powered (panel c and f) images of histological sections of human coronary plaques (all sections are stained with Movat Pentachrome). Early necrotic core in panel c is characterized by the infiltration of foamy macrophages into the lipid pool, with focal loss of proteoglycan and/or collagen matrix and cholesterol cleft. Late necrotic core in panel f consists of discrete collections of cellular debris with extensive cholesterol cleft and intraplaque haemorrage (balck arrows) where extracellular matrix is almost completely depleted. Adapted from Otsuka F et al. Nat Rev Cardiol 2014; 11:379-389.

Third, intraplaque haemorrhage is characterized by a large necrotic core (size >10% of plaque area) with haemorrhage, and plaque area shows presence of angiogenesis. Necrotic core communicates with the lumen through a fissure. Fourth, thin-cap fibroatheroma has a thin, fibrous cap (<65 µm) infiltrated by macrophages and lymphocytes, with rare or no smooth muscle cells and relatively large underlying necrotic core (>10% of plaque area).

In lesions associated with acute thrombi, the plaque rupture is the consequence of the cap disruption. Thrombosis is present and might or might not be occlusive. The luminal thrombus communicates with the underlying necrotic core.

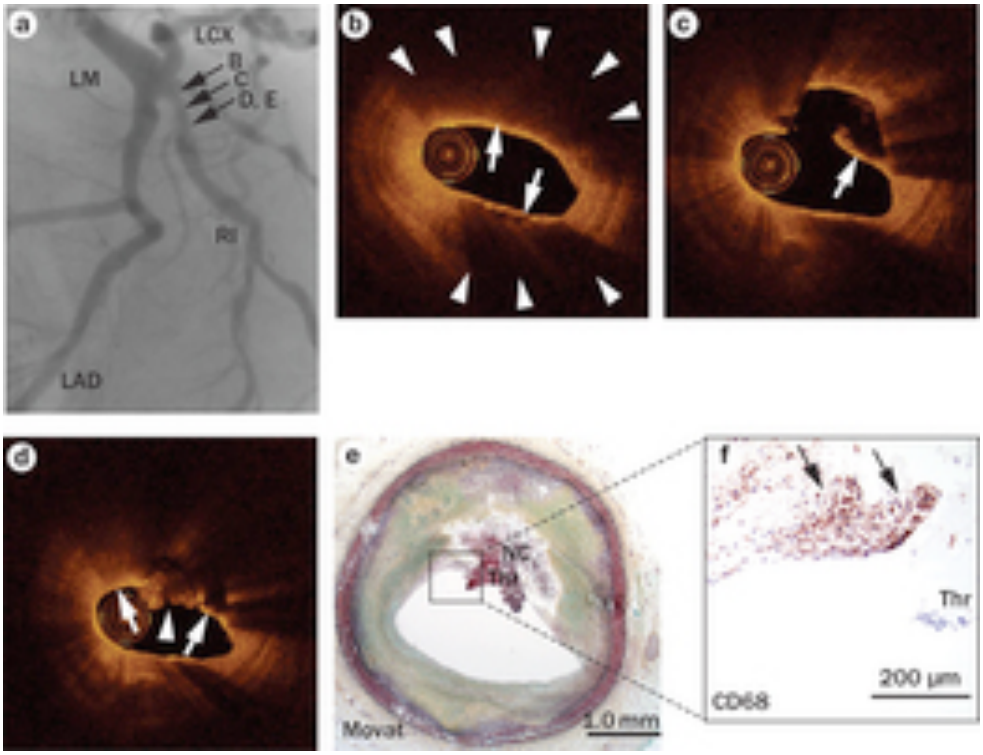

Ruptured plaque associated with non-occlusive luminal thrombus. **a** Post-mortem angiography showed mild luminal narrowing with hazziness at proximal ramus intermedius. **b-d** Serial OCT images revealed the presence of plaque rupture (in panels c and d) with non-occlusive luminal thrombus (white arrow head in panel d), and an adjacent distinct superficial signal-rich region (white arrows in panel b) with rapid attenuation (white arrow heads in panel b) indicating thin-cap fibroatheroma. Disrupted fibrous cap also show distinct superficial signal-rich region (white arrows in panel c and d). **e** Histology confirmed the presence of plaque rupture with an acute fibrin-rich thrombus (shown as Thr) overlying the necrotic core (section stained with Movat Pentachrome). **f** Immunostaining for CD68+ macrophages demonstrated substantial infiltration of macrophages within the disrupted fibrous cap (black arrows). Adapted from Otsuka F et al. Nat Rev Cardiol 2014; 11:379-389.

Conversely, plaque erosion can occur on pathological intimal thickening or on a fibroatheroma. Thrombosis is present and might or might not be occlusive. No communication of the thrombus with the necrotic core. Another acute lesion may be eruptive calcified nodule with an underlying fibrocalcific plaque with minimal or no necrosis.

Finally, healed lesions are composed of smooth muscle cells, proteoglycans, and collagen type III with or without underlying disrupted fibrous cap, necrotic core, or nodular calcification. Lesions can contain large areas of calcification with few inflammatory cells and have a small or no necrotic core. The fibrotic or fibrocalcific collagen-rich plaque is associated with significant luminal stenosis.

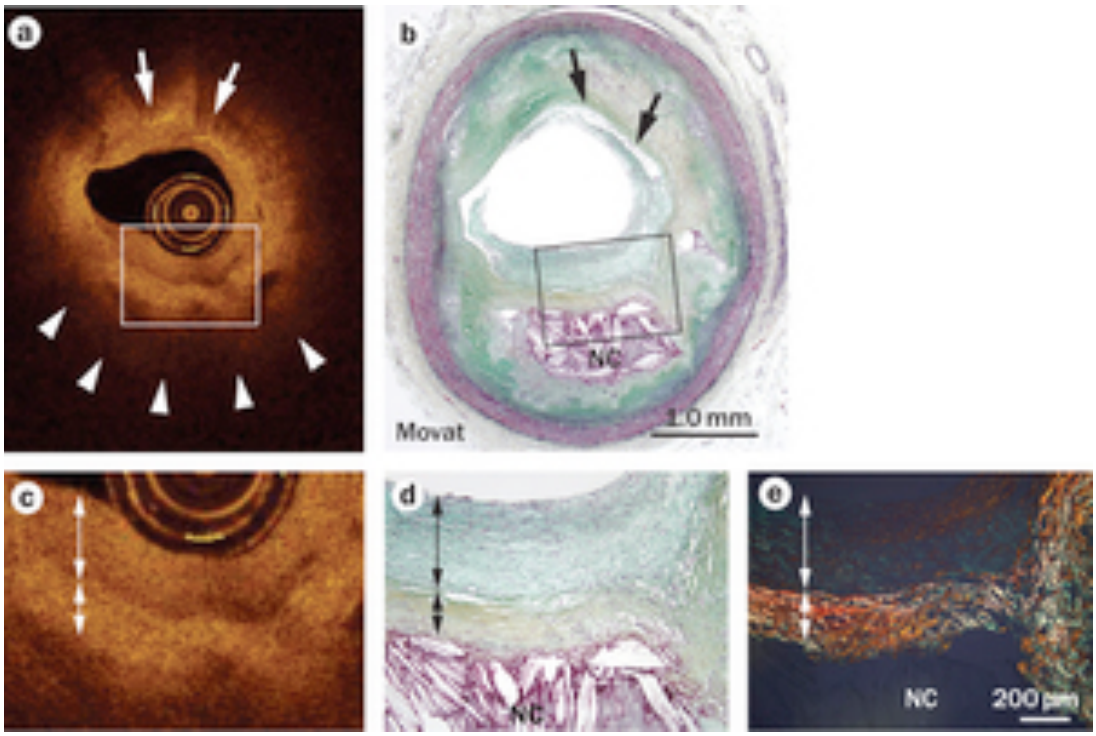

Healed plaque rupture. **a** An *ex vivo* OCT image shows a layered pattern of the signals and underlying signal-poor region with diffuse border (white arrow heads) and focal signal-rich confluent punctate area with rapid attenuation (white arrows). **b** A corresponding histological section of the human coronary plaque (stained with Movat Pentachrome) shows healed plaque rupture and underlying necrotic core with extensive haemorrhage and the presence of foamy macrophages close to the luminal surface (black arrows). **c** The layered pattern of the OCT signal is highlighted in a high-power image (white double arrows). **d** A high-power histological

section (stained with Movat Pentachrome) shows numerous smooth muscle cells within the newly formed proteoglycan-rich neointima (black double arrows close to the luminal surface), with clear demarcation from the underlying old collagen-rich fibrous cap. **e** In a high-power image of a Sirius-red-stained section (taken with polarized light) that corresponds with the image in panel d, dense (type I) collagen forms a fibrous cap, seen as reddish-yellow region, and is overlaid with newer (type III) collagen, detected as a greenish area. Adapted from Otsuka F et al. Nat Rev Cardiol 2014; 11:379-389.

Atherosclerotic plaque_____

References

1. Naghavi M, Libby P, Falk E, Casscells SW, Litvosky S, Rumberger S, et al. From vulnerable plaque to vulnerable patient: a call for new definitions and risk assessment strategies : part I. Circulation 2003;108:1664-1672.
2. McGill Jr HC, McMahan CA, Herderick EE, Malcom GT, Tracy RE, Strong JP. Origin of atherosclerosis in childhood and adolescence. Am J Clin Nutr 2000;72:1307S–15S.
3. Berliner JA, Navab M, Fogelman AM, Frank JS, Demer LL, Edwards PA, Watson AD, Lusis AJ. Atherosclerosis: basic mechanisms. Oxidation, inflammation and genetics. Circulation 1995; 91:2488-96.
4. Cybulsky MI, Gimbrone Jr MA. Endothelial expression of a mononuclear monocyte adhesion molecule during atherogenesis. Science 1991; 251:788-791.
5. Dong ZM, Chapman SM, Brown AA, Frenette PS, Hynes RO, Wagner DD. The combined role of P- and E- selectins in atherosclerosis. J Clin Invest 1998; 102:145-152.
6. Ross R. Atherosclerosis an inflammatory disease. N Engl J Med 1999; 340:115-126.
7. McMurray HF, Parthasarathy S, Steinberg D. Oxidatively modified low density lipoprotein is a chemoattractant for human T lymphocytes. J Clin Invest 1993; 92:1004-1008.
8. Galis ZS, Sukhova GK, Kranshofer R, Clark S, Libby P. Macrophage foam cells from experimental atheroma constitutively produce matrix-degrading proteinases. Proc Natl Acad Sci USA 1995; 92:402-406.
9. Matsumoto S, Kobayashi T, Katoh M, Saito S, Ikeda Y, Kobori M, Masuho Y, Watanabe T. Expression and localization of matrix metalloproteinase-12 in the aorta of cholesterol fed-rabbits: relationship to lesion development. Am J Pathol 1998; 153:109-119.
10. Toutouzas K, Benetos G, Karanasos A, Chatzizisis YS, Giannopoulos AA, Tousoulis D. Vulnerable plaque imaging: updates on new pathobiliological mechanisms. Eur Heart J 2015; 36:3147-3154.
11. Wyss CA, Neidhart M, Altwegg L, Spanaus KS, Yonekawa K, Wischnewsky MB, et al. Cellular actors, toll-like receptors, and local cytokine profile in acute coronary syndromes. Eur Heart J 2010; 31:1457-1469.

12. Boyle JJ, Harrington HA, Piper E, Elderfield K, Stark J, Landis RC, Haskard DO. Coronary intraplaque hemorrhage evokes a novel atheroprotective macrophage phenotype. Am J Pathol 2009; 174:1097–1108.
13. Kashiwagi M, Liu L, Chu KK, Sun CH, Tanaka A, Gardecki JA, Tearney GJ. Feasibility of the assessment of cholesterol crystals in human macrophages using micro optical coherence tomography. PLoS One 2014;9:e102669.
14. Vedre A, Pathak DR, Crimp M, Lum C, Koochesfahani M, Abela GS. Physical factors that trigger cholesterol crystallization leading to plaque rupture. Atherosclerosis 2009; 203:89–96.
15. Du F, Yu F,Wang Y, Hui Y, Carnevale K, Fu M, Lu H, Fan D. Microrna-155 deficiency results in decreased macrophage inflammation and attenuated atherogenesis in apolipoprotein e-deficient mice. Arterioscler Thromb Vasc Biol 2014; 34:759–767.
16. Raitoharju E, Oksala N, Lehtimaki T. Micrornas in the atherosclerotic plaque. Clin Chem 2013; 59:1708–1721.
17. Chatzizisis YS, Baker AB, Sukhova GK, Koskinas KC, Papafaklis MI, Beigel R, Jonas M,Coskun AU, Stone BV, Maynard C, Shi GP, Libby P, Feldman CL, Edelman ER, Stone PH. Augmented expression and activity of extracellular matrix-degrading enzymes in regions of low endothelial shear stress colocalize with coronary atheromata with thin fibrous caps in pigs. Circulation 2011; 123:621–630.
18. Chatzizisis YS, Jonas M, Coskun AU, Beigel R, Stone BV, Maynard C, Gerrity RG, Daley W, Rogers C, Edelman ER, Feldman CL, Stone PH. Prediction of the localization of high-risk coronary atherosclerotic plaques on the basis of low endothelial shear stress: an intravascular ultrasound and histopathology natural history study. Circulation 2008; 117:993–1002.
19. Stone PH, Saito S, Takahashi S, Makita Y, Nakamura S, Kawasaki T, Takahashi A, Katsuki T, Namiki A, Hirohata A, Matsumura T, Yamazaki S, Yokoi H, Tanaka S, Otsuji S, Yoshimachi F, Honye J, Harwood D, Reitman M, Coskun AU, Papafaklis MI, Feldman CL. Prediction of progression of coronary artery disease and clinical outcomes using vascular profiling of endothelial shear stress and arterial plaque characteristics: the prediction study. Circulation 2012; 126:172–181.
20. Vergallo R, Papafaklis MI, Yonetsu T, Bourantas CV, Andreou I, Wang Z, Fujimoto JG, McNulty I, Lee H, Biasucci LM, Crea F, Feldman CL, Michalis LK,

Stone PH, Jang IK. Endothelial shear stress and coronary plaque characteristics in humans: combined frequency-domain optical coherence tomography and computational fluid dynamics study. Circ Cardiovasc Imaging 2014; 7:905–911.

21. Wentzel JJ, Chatzizisis YS, Gijsen FJ, Giannoglou GD, Feldman CL, Stone PH. Endothelial shear stress in the evolution of coronary atherosclerotic plaque and vascular remodelling: current understanding and remaining questions. Cardiovasc Res 2012; 96:234–243.
22. Cheng C, Tempel D, van Haperen R, van der Baan A, Grosveld F, Daemen MJ, Krams R, de Crom R. Atherosclerotic lesion size and vulnerability are determined by patterns of fluid shear stress. Circulation 2006; 113:2744–2753.
23. Kwak BR, BackM, Bochaton-Piallat ML, Caligiuri G, Daemen MJ, Davies PF, Hoefer IE, Holvoet P, Jo H, Krams R, Lehoux S, Monaco C, Steffens S, Virmani R, Weber C, Wentzel JJ, Evans PC. Biomechanical factors in atherosclerosis: mechanisms and clinical implications. Eur Heart J 2014; 35:3013–3020, 3020a–3020d.
24. Stary HC, Chandler AB, Dinsmore RE, Fuster V, Glagov S, Insull W Jr, Rosenfeld ME, Schwartz CJ, Wagner WD, Wissler RW. et al. A definition of advanced types of atherosclerotic lesions and a histological classification of atherosclerosis. A report from the Committee on Vascular Lesions of the Council on Arteriosclerosis, American Heart Association. Arterioscler Thromb Vasc Biol 1995; 15:1512–1531.
25. Virmani R, Kolodgie FD, Burke AP, Farb A, Schwartz SM. Lessons from sudden coronary death: a comprehensive morphological classification scheme for atherosclerotic lesions. Arterioscler Thromb Vasc Biol 2000; 20:1262–1275.

2. Drawbacks of angiography

Angiography alone does not provide all information needed to fully assess the condition of the coronary artery disease, and hence leaves too much room for interpretation in some situations. Angiography provides a 2-dimension projection image of a moving 3-dimension anatomy and does not show to the physicians the pathology, that is, the atherosclerotic plaque [1]. This leads to ambiguity in measurements and identification of the culprit lesion. Furthermore, the lumen of the artery is only visualised, and not the vessel wall which is the cause of the disease. Pathologic studies show that the amount of atherosclerosis is often underestimated by angiography [2,3]. Sometimes, angiography provides poor contrast, especially for thrombus and dissection, leading to some doubts. Thus, intravascular imaging can provide valuable images of pathophysiology in addition to angiography. Unlike X-ray imaging, intravascular imaging technologies including Intravascular Ultrasound Studies (IVUS) and Optical Coherence Tomography (OCT) actually visualize the diseased vessel wall from inside the lumen and offer the possibility to perform tissue characterization, which is interesting to understanding pathophysiology and anticipating the vessel response to percutaneous coronary intervention. The aim of these intravascular imaging technologies is also to improve the results of coronary interventions including stent sizing, positioning and expansion [4]. We recently reported the additional value of OCT in diagnosing an isolated septal myocardial infarction due to spontaneous coronary artery dissection (SCAD).

Atherosclerotic plaque_____

References

1. Katritsis D, Webb-Peploe M. Limitations of coronary angiography: an underestimated problem?
2. Arnett EN, Isner JM, Redwood DR, Kent KM, Baker WP, Ackerstein H, Roberts WC. Coronary artery narrowing in coronary heart disease: Comparison of cineangiographic and necropsy findings. Ann Intern Med 1979; 91:350-356.
3. Vlodaver Z, Frech R, Van Tassel RA, Edwards JE. Correlation of the antemortem coronary arteriogram and the postmortem specimen. Circulation 1973; 47:162-169.
4. Yamashita T, Colombo A, Tobis JM. Limitations of coronary angiography compared with intravascular ultrasound: implications for coronary interventions. Prog Cardiovasc Dis 1999; 42: 91-137.

Isolated septal myocardial infarction due to spontaneous coronary artery dissection

Warren Chasseriaud [1] MD; Guillermo J. Tearney [2,3,4] MD, PhD; Michel Montaudon [5] MD; PhD; Benjamin Fialon [1] MD; Pierre Coste [1] MD; Edouard Gerbaud [1] MD.

Institutions:

[1] Soins Intensifs Cardiologiques - Plateau de Cardiologie Interventionnelle, CHU de Bordeaux, Hôpital du Haut Lévêque, Pessac, France

[2] Harvard Medical School and Wellman Center for Photomedicine, Massachusetts General Hospital, Boston, Massachusetts, United States of America

[3] Harvard-MIT Division of Health Sciences and Technology, Cambridge, Massachusetts, United States of America

[4] Department of Pathology, Harvard Medical School and Massachusetts General Hospital, Boston, Massachusetts, United States of America

[5] Unité d'Imagerie Thoracique et Cardiovasculaire, CHU de Bordeaux, Hôpital du Haut Lévêque, Pessac, France

International Journal of Cardiology 2016; 212:259-261.

Spontaneous coronary artery dissection (SCAD) is an infrequent cause of myocardial infarction and its cause remains unclear [1]. Most physicians are not familiar with various angiographic appearances of SCAD, contributing to why SCAD is often underdiagnosed on angiograms [2]. Isolated septal myocardial infarction is rare; mechanisms previously described are either thrombosis or spasm. We report the first comprehensive intracoronary imaging study of an isolated septal myocardial infarction due to SCAD.

A 53-year-old man was referred to our department complaining of severe chest pain that lasted for 40 min. Traditional risk factors were negative with the exception of smoking. Physical examination was normal, and in particular, blood pressure was in the normal range in both arms. His 18-lead electrocardiogram was normal. Troponin T raised to 13.5 ng/mL (N<0.04 ng/mL). Transthoracic echocardiography revealed antero-septal wall motion abnormalities, whereas chest pain disappeared before admission. Non-ST segment elevation myocardial infarction (NSTEMI) was suspected and coronary angiography was performed. Coronary vessels were normal with the exception of diffuse moderate stenosis on the first septal branch (Fig. 1A, Movie 1). TIMI grade flow was 3. Left ventriculography confirmed the presence of anteroseptal wall motion abnormalities (Movie 2). For further assessment and to confirm the NSTEMI, cardiac magnetic resonance (CMR) imaging was performed, showing antero-septal myocardial oedema associated with a predominant patchy mid-septal wall late gadolinium enhancement (LGE) lesion and an endocardial LGE lesion (Figs. 2A to 2C). To confirm the diagnosis and understand the mechanism of this atypical acute myocardial infarction (AMI), OCT was performed and demonstrated an intimal tear of the first septal branch associated with intramural hematoma (Figs. 1B to 1F, Movie 3). The left descending coronary artery (LAD) was normal. Medical treatment including β-blocker, aspirin and statin was administered. At follow-up, including CMR imaging 3 months later (Figs. 2D to 2F), the patient was asymptomatic. The aetiology remains unknown in this patient, as he had no findings suggestive of fibromuscular dysplasia and a precipitating stress event was not noted.

In our observation, even if the clinical presentation is classic for a SCAD as an NSTEMI, the patient's characteristics are not: he is a middle-age man, with no personal traditional cardiovascular risk factors, no relevant connective tissue disorders or systemic inflammatory conditions and no drug consumption [3].

The LGE pattern on CMR was atypical in the acute phase. Indeed, CMR showed a patchy mid septal and endocardial wall late gadolinium enhancement LGE whereas the classical findings of coronary artery disease are a subendocardial LGE pattern. This non-

specific CMR feature has recently been described in one case report published by Iwakami and al. [4] and could suggest a particular CMR pattern of myocardial ischemia in the septal territory. In our observation, the additional value of early CMR to confirm the diagnosis of isolated septal acute myocardial infarction was unclear. However, the control CMR demonstrated more accurately a subendocardial LGE pattern, probably due to the resorption of myocardial oedema.

Only few cases of isolated septal myocardial infarction are reported in the literature; mechanisms previously described are either thrombosis or spasm [4-5]. Interestingly, septal dissection was localised and not a consequence of LAD dissection. Although SCAD is not per se rare as a cause of AMI, septal coronary branches have the distinction of having a perforating course through the ventricular septum. To our knowledge this observation is the first to describe a coronary dissection of a septal perforating branch causing AMI. Another differential diagnosis of this NSTEMI was coronary embolism into this septal branch. Thus, all interventional cardiologists of the team initially did not recognize a SCAD, until OCT made the correct diagnosis. Thus, it was of importance to perform intravascular imaging to understand the correct mechanism and to confirm the correct diagnosis.

Disclosures: Dr. Tearney receives royalties from Terumo Corporation and MIT. Dr. Tearney's lab receives sponsored research from Canon, Inc. USA.

References

1. D. Giacoppo, D. Capodanno, G. Dangas, C. Tamburino, Spontaneous coronary artery dissection, Int. J. Cardiol. 175 (2014) 8–20.
2. J. Saw, Coronary angiogram classification of spontaneous coronary artery dissection, Catheter. Cardiovasc. Interv. 84 (2014) 1115–1122.
3. J. Saw, E. Aymong, T. Sedlak, C.E. Buller, A. Starovoytov, D. Ricci, et al., Spontaneous coronary artery dissection: association with predisposing arteriopathies and precipitating stressors and cardiovascular outcomes, Circ. Cardiovasc. Interv. 7 (2014) 645–655.
4. N. Iwakami, T. Noguchi, Y. Ikeda, E. Tateishi, Y. Morita, H. Kanzaki, et al., Isolated septal branch myocardial infarction due to coronary spasm mimicking non-ischemic late gadolinium enhancement pattern on cardiac magnetic resonance imaging, Circ. J. 79 (2015) 2280–2282.
5. J. Tomcsanyi, B. Bozsik, A. Zsoldos, T. Simor, Isolated spontaneous septal myocardial infarction, J. Electrocardiol. 45 (2012) 280–282.

Figure 1

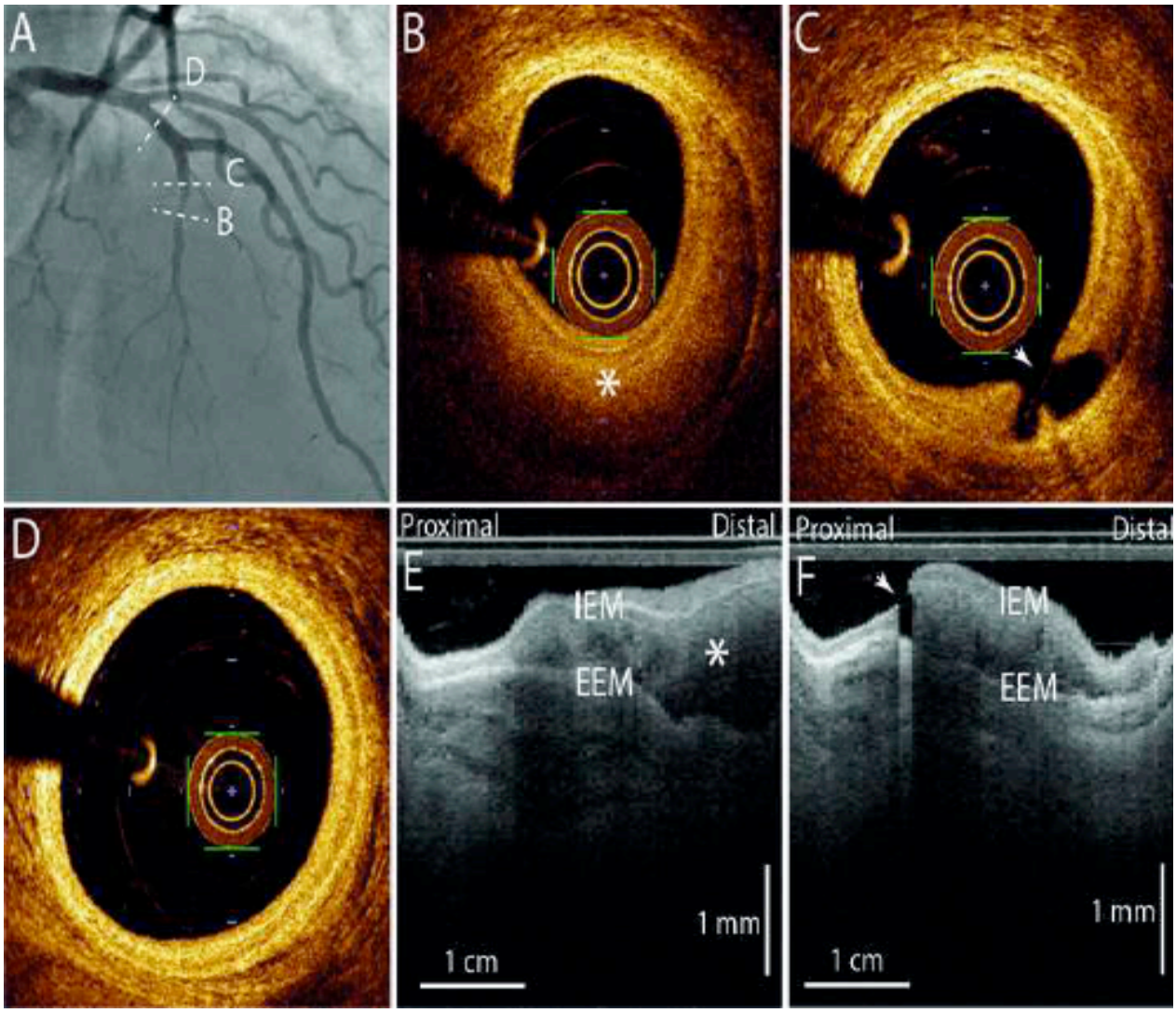

Figure 1: Angiographic and OCT Findings. **(A)** Initial coronary angiography of the left coronary artery demonstrating normal arterial epicardic vessels with the exception of diffuse moderate stenosis on the first septal branch (arrows). (**B, C, D)** Corresponding OCT images of the first septal branch lesion demonstrating the intimal tear of the septal artery (arrowhead) associated with intramural hematoma (asterisk). Left descending coronary artery was normal. (**E, F)** Longitudinal reconstructions of this spontaneous coronary artery dissection. EEM: external elastic membrane; IEM: internal elastic membrane.

Figure 2

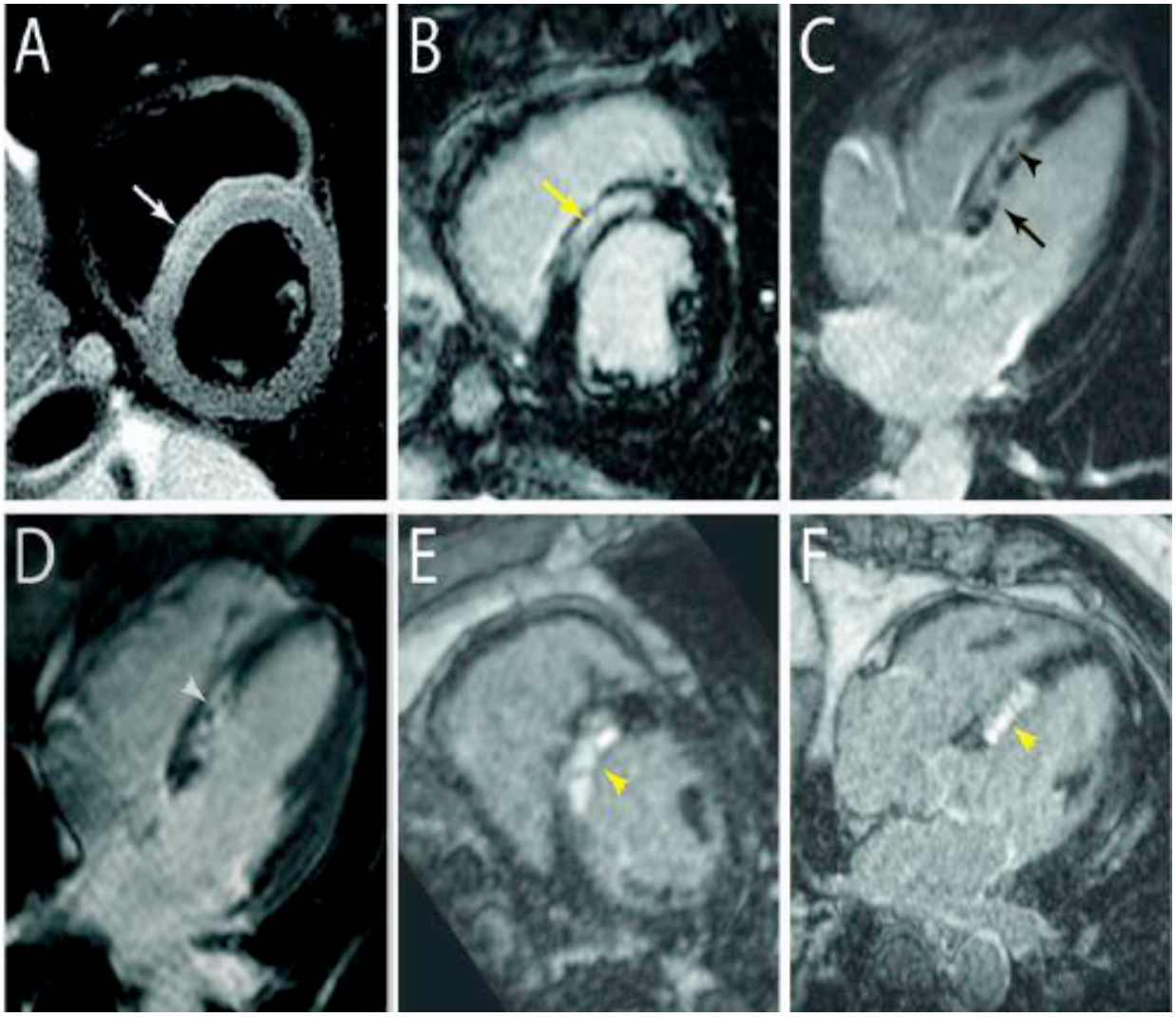

Figure 2: CMR Imaging Findings at Baseline and 3 Months Later. (**A**) Initial T2-weighted Spectral Attenuated Inversion Recovery (SPAIR) breath hold pulse sequence showing myocardial oedema in the septal wall (white arrow). (**B, C)** Corresponding 3-dimensional turbo fast low-angle short inversion recovery (3D TurboFLASH IR) sequences (short axis and 4-chamber views) depicting a predominant patchy mid-septal wall late gadolinium enhancement LGE lesion (yellow arrow) associated with microvascular obstruction (black arrowhead) and an endocardial LGE lesion (black arrow). (**D)** 3 months later, the heterogeneous LGE lesion was clearly localized to the subendocardium (white arrowhead). (**E, F)** Corresponding 3-dimensional, inversion-recovery-prepared, ECG-gated, respiration-navigated gradient-echo pulse sequences (short axis and 4-chamber views) with fat-saturation and high resolution, confirming the subendocardial LGE pattern in the septal wall (yellow arrowheads).

2.1 Intravascular ultrasound studies (IVUS)

2.1.1 Basic physical principles

Intravascular Ultrasound Studies (IVUS) has become increasingly important in both clinical and research applications. Image quality can be partially described by two important factors: spatial resolution and contrast resolution. Spatial resolution, or the minimum distance between closely spaced objects that can be independently detected by the imaging system, has 2 directions: axial (parallel to the light beam) and lateral or transverse (perpendicular to the light beam). For a 20 to 40 MHz IVUS transducer, the typical resolution is 80 microns axially and 200 to 250 microns laterally. For a 60 MHz IVUS transducer, the spatial resolution may be less than 40 microns. Contrast resolution is the distribution of the grayscale of the reflected signal and is often referred to as dynamic range. An image of low dynamic range appears as black and white with a few in-between gray scale levels; images at high dynamic range are often softer, with preserved subtleties in the image presentation. As an ultrasound pulse encounters a boundary between two tissues – fat and muscle, for instance, the beam will be partially reflected and partially transmitted. The degree of reflection depends on the difference between the mechanical impedance of the two materials. Furthermore, as the wave passes through many tissue interfaces, the energy is attenuated. Attenuation is a function of the tissue characteristics, the scattering of energy by small objects, and the absorption by tissue. Thus, only a small percentage of the emitted signal returns to the transducer. The received signal is converted to electrical energy and sent to an external signal processing system for amplification, filtering, scan-conversion, user-controlled modification, and finally, graphic presentation [1].

2.1.2 Advantages and limitations of IVUS

From a clinical and technical point of view, what are the advantages of IVUS? IVUS has been used clinically for nearly 3 decades [2]. Pre-intervention IVUS imaging is often possible without pre-dilation, although ischemia may be observed during the IVUS acquisition. Ultrasound penetration to the adventitia allows measurement of the true vessel size (external elastic membrane) and plaque burden, facilitating mid-wall or true vessel stent sizing to optimize stent dimensions and identifying a landing zone with the smallest plaque burden to minimize geographical miss. IVUS predictors of stent failure (stent underexpansion, major edge

dissections, and geographic miss but not acute strut malapposition) are well established. Thus, meta-analyses of randomized IVUS versus angiography-guided bare metal stent or drug eluting stent implantation trials found that IVUS guidance reduces restenosis and repeat revascularization with no impact on death or myocardial infarction [3,4]. Furthermore, these meta-analyses are supported by a published randomized trial (RESET [Real Safety and Efficacy of a 3-Month Dual Antiplatelet Therapy Following Zotarolimus-Eluting Stents Implantation]) from South Korea [5] as well as by a large-scale prospective observational study (ADAPT-DES [Assessment of Dual AntiPlatelet Therapy with Drug-Eluting Stents]) in more than 8,500 patients [6]. In the same way, a patient-level pooled analysis of 4 registries of patients with left main disease treated with drug eluting stent (DES) in Spain show an association of IVUS guidance during percutaneous coronary intervention with better outcomes in patients with left main disease undergoing revascularization with DES [7]. However, IVUS spatial resolution still to be limited for thrombus, neovascularization or macrophages identification.

2.2 Optical coherence tomography (OCT)

2.2.1 Basic physical principles

Optical coherence tomography (OCT) is a light-based imaging modality that generates high-resolution cross-sectional images of tissue microstructure. The underlying concept of OCT is analogous to that of IVUS, by measuring the delay time of optical echoes reflected or backscattered from subsurface structures in biological tissues, structural information as a function of depth within the tissue can be obtained. OCT light is in the near infrared (NIR) range, typically with wavelengths of approximatively 1.3 microns, which are not visible to human eye. OCT measures the time delay of the light that is reflected or backscattered from tissue, and that is collected by the catheter, by using a technique known as interferometry. Light from the OCT system is split so that a portion of it travels to the patient (sample arm) through a catheter and another portion travels a predetermined distance (reference arm). After being reflected from tissue and collected by the catheter, the sample arm light is combined with the reference arm light detected by a detector. When the distance that the sample and reference arm lights have travelled are roughly equivalent, a pattern of high and low intensities are detected, known as interference. This interference pattern is analyzed by

the OCT system to determine the amount of backscattering as a function of delay time or depth within the tissue (A-line) [8]. A cross-sectional intravascular optical coherence tomography (IVOCT) image is obtained by recording A-lines as the beam is scanned across the sample by rotating the optics in the catheter. There are 2 types of IVOCT systems: earlier time-domain OCT (TD-OCT) and more recent Fourier-domain OCT systems, also known as frequency domain OCT (FD-OCT), sweptsource OCT, or optical frequency domain imaging (OFDI). The main difference between TD-OCT and FD-OCT systems is that FD-OCT systems are capable of obtaining A-lines at much higher imaging speeds, facilitating rapid, 3D pullback imaging during the administration of a nonocclusive flush of an optically transparent media such as Lactated Ringer's or radiocontrast. Like IVUS, IVOCT image quality is in part dependent on spatial resolution. The axial resolution for OCT is dependent on the spectral bandwidth, or range of wavelengths in the light source, and is typically approximately 10 microns. Near the tip of the catheter, light is focused by a small lens and directed toward the vessel wall. The light converges to a minimum diameter spot (focus) outside the catheter and then diverges. The focal location is typically 1 to 3 mm outside the catheter's sheath. The lateral resolution of the OCT image is best at the focus, typically between 20 and 40 microns. Optical frequency domain imaging (OFDI), also known as Frequency Domain optical coherence tomography (FD-OCT), has been invented and developed in Dr. Tearney's laboratory. This imaging modality provides rapid, three-dimensional imaging of detailed plaque microstructure in vivo [9].

2.2.2 Advantages and limitations of OCT

What are the advantages of OCT, especially compared with IVUS? The resolution of OCT is 10 times greater than IVUS such that OCT detects fi ne details missed by IVUS (e.g., edge dissections, small amounts of malapposition, tissue protrusion, stent strut coverage, fibrous cap thickness), as shown by several studies. OCT tissue characterization is better, and OCT may be the gold standard for thrombus detection. The images are clearer and easier to interpret, in part because the obligatory flushing clears the lumen of blood. Rapid automated pullback afforded by OCT minimizes ischemia. One published study by Prati et al. found that OCT-guided DES implantation may be better than angiographic guidance [10]; OCT reduced repeat revascularization, myocardial infarction, and cardiac death. The major drawback of OCT is lack of depth penetration. As such, the external elastic membrane and extent of

plaque burden cannot typically always be measured [11]. Thus, with OCT procedural guidance, stent diameters are chosen to match the reference lumen (potentially resulting in smaller stent areas than with IVUS guidance), and avoiding geographic miss may be more difficult with OCT than with IVUS.

Among all these aspects, another important factor is the reproducibility of these two intravascular imaging modalities. Consensus document guidelines have been published for both techniques in order to harmonize their use and analysis [1,8]. In a core laboratory setting, the inter and intra-observer reproducibility for qualitative and quantitative measurements with both techniques has been previously established in some studies [12,17]. However, the combined inter-institute reliability for IVUS and IVOCT is currently lacking.

References

1. Mintz GS, Nissen SE, Anderson WD, Bailey SR, Erbel R, Fitzgerald PJ, et al. American College of Cardiology clinical expert consensus document on standards for acquisition, measurement and reporting on intravascular ultrasound studies (IVUS). A report of the American College of Cardiology task force on clinical expert consensus documents. J Am Coll Cardiol 2001; 37:1478-92.
2. Maehara A, Mintz GS, Stone GW. OCT versus IVUS: accuracy versus clinical utility. J Am Coll Cardiol Img 2013; 10:1105-7.
3. Parise H, Maehara A, Stone GW, Leon MB, Mintz GS. Meta-analysis of randomized studies comparing intravascular ultrasound versus angiographic guidance of percutaneous coronary intervention in pre-drug eluting stent era. Am J Cardiol 2011; 107:374–82.
4. Zhang Y, Farooq V, Garcia-Garcia HM, Bourantas CV, Tian N, Dong S, et al. Comparison of intravascular ultrasound versus angiography-guided drug-eluting stent implantation: a meta-analysis of one randomised trial and ten observational studies involving 19,619 patients. EuroIntervention 2012; 8:855–65.
5. Kim JS, Kang TS, Mintz GS, Park BE, Shin DH, Kim BK, et al. Randomized comparison of clinical outcomes between intravascular ultrasound and angiography-guided drug eluting stent implantation for long coronary artery stenoses. J Am Coll Cardiol Intv 2013; 6:369–76.

6. Witzenbichler B, Maehara A, Weisz G, Neumann FJ, Rinaldi MJ, Metzger DC, et al. Relationship between intravascular ultrasound guidance and clinical outcomes after drug-eluting stents: the assessment of dual antiplatelet therapy with drug-eluting stents (ADAPT-DES) study. Circulation 2014; 129:463-470.
7. de la Torre Hernandez JM, Baz Alonso JA, Gómez Hospital JA, Alfonso Manterola F, Garcia Camarero T, Gimeno de Carlos F, Roura Ferrer G, Recalde AS, Martínez-Luengas IL, Gomez Lara J, Hernandez Hernandez F, Pérez-Vizcayno MJ, Cequier Fillat A, Perez de Prado A, Gonzalez-Trevilla AA, Jimenez Navarro MF, Mauri Ferre J1, Fernandez Diaz JA, Pinar Bermudez E, Zueco Gil J; IVUS-TRONCO-ICP Spanish study. Clinical impact of intravascular ultrasound guidance in drug-eluting stent implantation for unprotected left main coronary disease: pooled analysis at the patient-level of 4 registries. JACC Cardiovasc Interv. 2014; 7:244-54.
8. Tearney GJ, Regar E, Akasaka T, Adriaenssens T, Barlis P, Bezerra HG, et al. International Working Group for Intravascular Optical Coherence Tomography (IWG-IVOCT). Consensus standards for acquisition, measurement, and reporting of intravascular optical coherence tomography studies. A report from the international working group for intravascular optical coherence tomography standardization and validation. J Am Coll Cardiol 2012; 59:1058-72.
9. Tearney GJ, Waxman S, Shishkov M, Vakoc BJ, Suter MJ, Freilich MI, et al. Three-dimensional coronary artery microscopy by intracoronary optical frequency domain imaging. J Am Coll Cardiol Img 2008; 1:752-761.
10. Prati F, Di Vito L, Biondi-Zoccai G, Occhipinti M, La Manna A, Tamburino C, et al. Angiography alone versus angiography plus optical coherence tomography to guide decision-making during percutaneous coronary intervention: the Centro per la Lotta contro l'Infarto-Optimisation of Percutaneous Coronary Intervention (CLIOPCI) study. EuroIntervention 2012; 8:823–9.
11. Kubo T, Akasaka T, Shite J, Suzuki T, Uemura S, Kozuma K, et al. OCT compared with IVUS in a coronary lesion assessment. The OPUS-CLASS study. J Am Coll Cardiol Img 2013; 6:1095-11.
12. Haussmann D, Lundkvist AJS, Friedrich GJ, Mullen WL, Fitzgerald PJ, Yock PG. Intracoronary ultrasound imaging: intraobserver and interobserver variability of morphometric measurements. Am Heart J 1994; 128:674-680.

13. Blessing E, Hausmann D, Sturm M, Wolpers HG, Amende I, Mügge A. Intravascular ultrasound and stent implantation: intraobserver and interobserver variability. Am Heart J 1999; 137:368-71.
14. Palmer ND, Northridge D, Lessells A, McDicken WN, Fox KA. In vitro analysis of coronary atheromatous lesions by intravascular ultrasound; reproducibility and histological correlation of lesion morphology. Eur Heart J 1999; 20:1701-6.
15. 10. Gonzalo N, Garcia-Garcia HM, Serruys PW, Commissaris KH, Bezerra H, Gobbens P, et al. Reproducibility of quantitative optical coherence tomography for stent analysis. Eurointervention 2009; 5:224-232.
16. Fedele S, Biondi-Zoccai G, Kwiatkowski P, Di Vito L, Occhipinti M, Cremonesi A, et al. Reproducibility of coronary optical coherence tomography for lumen and length measurements in humans (The CLI-VAR [Centro per la Lotta contro l'Infarto-VARiability] study. Am J Cardiol 2012; 110:1106-1112.
17. Paoletti G, Marco V, Romagnoli E, Gatto L, Fedele S, Mangiameli A, et al. Reproducibility of serial optical coherence tomography measurements for lumen area and plaque components in humans (The CLI-VAR [Centro per la Lotta Contro l'Infarto-variability] II study) Int J Cardiovasc imaging 2016; 32:381-387.

Multi-laboratory inter-institute reproducibility study of IVOCT and IVUS assessments using published consensus document definitions

Edouard Gerbaud[1], Giora Weisz[2], Atsushi Tanaka[1], Manabu Kashiwagi[1], Takehisa Shimizu[2], Lin Wang[2], Christiano Souza[2], Brett E. Bouma[1], Melissa J. Suter[1], Milen Shishkov[1], Giovanni J. Ughi[1], Elkan F. Halpern[3], Mireille Rosenberg[1], Sergio Waxman[4], Jeffrey W. Moses[2], Gary S. Mintz[2], Akiko Maehara[2†], and Guillermo J. Tearney[1,5,6]

Institutions:

[1] Harvard Medical School and Wellman Center for Photomedicine, Massachusetts General Hospital, Boston, Massachusetts, United States of America

[2] Columbia University Medical Center, New York, New York; Cardiovascular Research Foundation, New York, New York, United States of America

[3] Institute for Technology Assessment, Massachusetts General Hospital, Boston, Massachusetts, United States of America

[4] Department of Cardiology, Lahey Clinic Medical Center, Burlington, Massachusetts, United States of America

[5] Harvard-MIT Division of Health Sciences and Technology, Cambridge, Massachusetts, United States of America

[6] Department of Pathology, Harvard Medical School and Massachusetts General Hospital, Boston, Massachusetts, United States of America

[†] A.K. shared senior author.

European Heart Journal Cardiovascular Imaging 2016; 17:756-764.

Abstract

Aims: The aim of the study was to investigate the reproducibility of intravascular optical coherence tomography (IVOCT) assessments, including a comparison to intravascular ultrasound (IVUS). Intra-observer and inter-observer variability of IVOCT has been previously described, whereas inter-institute reliability in multiple laboratories has never been systematically studied.

Methods and results: In 2 independent laboratories with intravascular imaging expertise, 100 randomized matched data sets of IVOCT and IVUS images were analyzed by 4 independent observers according published consensus document definitions. Intra-, inter-observer and inter-institute variability of IVOCT qualitative and quantitative measurements versus IVUS measurements were assessed. Minor inter and intra-observer variability of both imaging techniques was observed for detailed qualitative and geometric analysis, except for inter-observer mixed plaque identification on IVUS (κ=0.70) and for inter-observer fibrous cap thickness measurement reproducibility on IVOCT (ICC=0.48). The magnitude of inter-institute measurements differences for IVOCT was statistically significantly less than for IVUS concerning lumen cross section area (CSA), maximum and minimum lumen diameters, stent CSA, maximum and minimum stent diameters ($p<0.001$, $p<0.001$, $p<0.001$, $p=0.02$, $p<0.001$ and $p=0.01$, respectively). Minor inter-institute measurement variabilities using both techniques were also found for plaque identification.

Conclusion: In the measurement of lumen CSA, maximum and minimum lumen diameters, stent CSA, maximum and minimum stent diameters by analysts from 2 different laboratories, reproducibility of IVOCT was more consistent than IVUS.

Keywords: Reproducibility, intravascular ultrasound imaging, optical frequency domain imaging, optical coherence tomography.

List of abbreviations:

IVUS: Intravascular ultrasound

IVOCT: intravascular optical coherence tomography

PCI: percutaneous coronary intervention

FD-OCT: frequency domain optical coherence tomography

CSA: cross section area

EEM: external elastic membrane

IEM: internal elastic membrane

ICC: intra-class coefficient correlation

Introduction

Intravascular ultrasound (IVUS) and intravascular OCT (IVOCT) are widely available for evaluating high-resolution images the coronary artery in vivo. Consensus document guidelines have been published for both techniques in order to harmonize their use and analysis [1-4]. These two techniques are increasingly used for the assessment of the natural history of atherosclerosis, vascular remodelling, pharmacological and percutaneous interventions [5-6]. In a core laboratory setting, the inter- and intra-observer reproducibility for qualitative and quantitative measurements with both techniques has been previously established in many studies [7-11]. Whereas one study underlines the necessity to centrally analyze IVUS data obtained in multicentre studies [12], to the best of our knowledge, the evaluation of inter-institute reliability for IVOCT is currently lacking. Indeed, awareness of the inter-institute differences may be particularly important in multicentre pharmacological or percutaneous intervention trials. Accordingly, the purpose of this study was to investigate, further inter- and intra-observer reproducibility, the inter-institute variability for IVOCT quantitative and qualitative measurements versus IVUS measurements using published consensus document definitions.

Methods

Study Population

42 non-consecutive patients scheduled for elective PCI were enrolled in two centres (Columbia University Medical Center, New York, NY, USA and Lahey Clinic Medical Center, Burlington, MA, USA). MGH, Columbia, and Lahey IRBs approved the study protocol. Patients with acute coronary syndrome, hemodynamic instability, renal insufficiency (glomerular filtration rate <50mL/min), allergy to X-ray contrast, unprotected left main coronary artery disease, venous bypass graft lesions, chronic total occlusions, last remaining vessel or extremely tortuous vessels were excluded. Patients underwent the following procedures in the catheterization laboratory: coronary angiography, percutaneous coronary intervention of the culprit lesion and intravascular imaging in random order: IVOCT imaging, IVUS imaging. 74 coronary arteries (left anterior descending artery, n = 28; left circumflex artery, n = 23; right coronary artery, n = 23) imaged from these 42 patients were studied. 96 pullbacks on both native (primarily, n = 27) and stented coronary artery segments (pre-PCI, n = 26; post-PCI, n = 43) were included. To assess the inter-observer, intra-observer and inter-institute variability of IVOCT quantitative and qualitative measurements versus IVUS measurements, randomized matched data sets of 100 IVOCT and 100 IVUS intracoronary

images were analyzed by 4 independent observers from two different laboratories (E.G and M.K for the Tearney laboratory, Massachusetts General Hospital, Boston; T.S and L.W for the Columbia University Medical Center, New York, New York) who were blinded to other data (Table 1). These four observers had worked for at least 1 year as intravascular imaging researchers and were certified by their respective laboratories by completion of a common training program.

IVUS Acquisition

IVUS imaging was performed after intracoronary administration of nitrates (0.1-0.2 mg) using commercially available mechanical (iLab^{TM} with 40-MHz Atlantis SR Pro catheters, Boston Scientific, Fremont, CA, USA) or phased array transducer systems (s5^{TM} with 20-MHz Eagle Eye Gold catheters, Volcano Therapeutics, Rancho Cordova, CA, USA) as described elsewhere in conventional manner, using an automated pullback device operating at 0.5 mm/s [13].

IVOCT Acquisitions

IVOCT imaging was performed with non-commercial frequency domain optical coherence tomography (FD-OCT) systems (Wellman Center for Photomedicine, Massachusetts General Hospital, Boston, USA) that operate and perform identically to commercial IVOCT systems as described previously [14,15]. This system used a wavelength-swept laser (frequency of 1,310 nm) as a light source. The FD-OCT imaging catheter had a short monorail design with a catheter profile of 2.4Fr compatible with 6F guiding catheters. The technique of OCT acquisitions was in line with recent expert review documents [3]. During the flushing process, motorized pullback FD-OCT imaging was performed at a rate of 20 mm/s.

Matched IVUS-IVOCT images sets

The matched IVUS-IVOCT images sets were made by 2 independent interventional cardiologists (A.M. or A.T.) who have 10 years of experience in intravascular imaging. They generated Tiff stack files from original IVUS and OCT data. Complex geometries such as side-branch take-off/bifurcation carina were included. Images were preliminarily evaluated for diagnostic quality. Typical IVUS artifacts (i.e. non-uniform rotational distortion, air bubble and geometric distortion due to the off-centered position of the IVUS probe in the artery) were excluded. Typical IVOCT artifacts (i.e. movement artifacts, flush defect artifacts, fiber decentration and non-parallelism artifacts) were also excluded. IVUS and OCT images that were deemed to be of diagnostic quality were then co-registered by pullback distance and confirmed by using anatomical landmarks and following these successive steps: 1) The absolute landmarks were the left anterior descending coronary artery/left circumflex coronary

artery bifurcation for the left coronary artery system or the atrio-ventricular node coronary artery/posterior descending coronary artery bifurcation for the right coronary artery system, 2) Additional anatomical landmarks i.e. side branch or perivascular structure such as vein, muscle were systematically used, 3) Morphological features in the cross-sectional image, including calcification shape, prominent vasa vasorum and lumen morphology were also used to confirm registration precision, 4) Stent features including post-stent or old stent cases permitted to obtain corresponding images of IVUS and IVOCT, and 5) Known pullback speed was integrated when pullbacks were considered quite stable (i.e. A.M. or A.T. did not recognize any nonlinearities in the pullback rate) and confirmed the same length (less than 10% of difference) between IVUS and IVOCT. Among this database, sets of 100 IVUS-IVOCT matched images were generated using web-based randomization software.

IVUS data analysis

IVUS measurements, both geometric and compositional analyses, were made on a stand-alone computer workstation using ImageJ software [16]. All quantitative and qualitative data were evaluated following published consensus document definitions [1,2]. The lumen and vessel borders were traced manually for each image (Figure 1). To evaluate the intra-observer variability, one observer of the Columbia University Medical Center repeated the analysis of another set one month later. The following quantitative data were measured: lumen cross section area (lumen CSA), minimum and maximum luminal diameters, stent cross section area (stent CSA), minimum and maximum stent diameters, external elastic membrane (EEM) area when identified and/or present under the lesion [excluding cross-sectional images that contain artifact(s) that obscure a significant portion (>90°)], atheroma cross section area (atheroma CSA) (defined by the EEM CSA minus lumen CSA), plaque burden [calculated as (Atheroma CSA / EEM CSA) X 100 (%)], minimum and maximum atheroma thicknesses, atheroma eccentricity index [calculated as (Maximum atheroma thickness – Minimum atheroma thickness) / Maximum atheroma thickness], the total arc of attenuation and the total arc of calcium. The total arc of attenuation equals to sum of different arcs of attenuation in the same cross section. The total arc of calcium equals to sum of different arcs of calcium in the same cross section. According consensus document definitions [1], plaque composition was also characterized in one of the following categories: hypoechoic, hyperchoic/isoechoic, calcified or mixed. Echo-attenuated plaque was also identified by the absence of the ultrasound signal behind plaque that was either hypo-echoic or isoechoic but contained no bright calcium. Plaque rupture, thrombus, plaque protrusion, incomplete stent apposition and dissection were also assessed.

IVOCT data analysis

Anonymized data were analysed on a stand-alone computer workstation using ImageJ software [16] (Figure 2). All quantitative and qualitative data were evaluated following the published consensus document definitions [3,4]. To evaluate the intra-observer variability, one observer of the Tearney laboratory repeated the analysis of another set one month later. The following quantitative data were measured: lumen CSA, minimum and maximum luminal diameters, stent CSA, minimum and maximum stent diameters, EEM area when identified and/or present under the lesion, atheroma CSA (defined by the EEM CSA minus lumen CSA), plaque burden [calculated as (Atheroma CSA / EEM CSA) X 100 (%)], minimum and maximum atheroma thicknesses, atheroma or plaque eccentricity index, internal elastic membrane (IEM) when identified and/or present under the lesion. The same lumen measurements as for EEM have been made for the IEM. All these measurements were obtained, if EEM and/or IEM were clearly identified in the IVOCT image (excluding EEM and/or IEM delineation when image contain a significant obscure part on more than 90 degrees of its circumference). According consensus document definitions, plaque composition was also characterized in one of the following categories: fibroatheroma, fibrous plaque and fibrocalcific plaque. The cut-off minimal cap thickness used to define the thin-capped fibroatheroma was 65 μm. The maximum lipid arc, the fibrous cap thickness (mean of three successive measurements) and the maximum calcium arcs were also measured. Plaque rupture, thrombus, prolapse, stent malapposition, dissection, macrophages within plaque, cholesterol crystals and intimal vessels were also identified [3].

Statistical Analysis

Continuous data are expressed as mean ± standard deviation, or median (interquartile range) when appropriate. Intra-observer and inter-institute variability for IVUS and IVOCT quantitative data were determined as mean (relative) difference (bias) and standard deviations according to the methods of Bland and Altman. For each image, the magnitude of the difference observed between the two laboratories was computed as the absolute value for lumen CSA, minimum and maximum luminal diameters, stent CSA, minimum and maximum stent diameters, EEM area when identified and/or present under the lesion, atheroma CSA, plaque burden, minimum and maximum atheroma thicknesses, atheroma or plaque eccentricity index. For comparisons within the magnitudes of inter-institute measurement differences for IVUS and IVOCT, a Wilcoxon signed rank test was performed. Inter-observer agreement for quantitative data of both techniques was assessed by intraclass correlation coefficient (ICC) based on the random effects analysis of variance model. An ICC

value > 0.90 was considered excellent. Analysis was performed using Cohen's kappa or Fleiss' Kappa (where the number of observers > 2) for categorical variables. A kappa value of 0.81 to 1.0 indicates almost perfect agreement; a value of 0.61 to 0.80 indicates substantial agreement, and a value of 0.41 to 0.60 indicates moderate agreement [17]. P-values <0.05 were considered significant. All statistics were calculated using NCSS (NCSS 2001; NCSS Statistical software, Kaysville, Utah).

Results

Intra-observer variability for IVUS measurements

Intra-observer variability was very low for lumen CSA, minimum and maximum luminal diameters (-0.05 ± 0.25 mm^2, -0.03 ± 0.09 mm, -0.04 ± 0.21 mm, respectively) (Figure 3 and on-line supplementary Table S1). Likewise, the mean (standard deviation) differences were negligible for stent CSA, minimum and maximum stent diameters (0.04 ± 0.23 mm^2, 0.004 ± 0.13 mm, 0.03 ± 0.11 mm, respectively). Intra-observer variability was also low for EEM area, atheroma CSA, plaque burden, minimum atheroma thickness, maximum atheroma thickness and atheroma eccentricity index (-0.15 ± 0.87 mm^2, -0.10 ± 0.88 mm^2, -0.02 ± 3.1 %, 0.01 ± 0.06 mm, -0.02 ± 0.20 mm, -0.02 ± 0.07, respectively). Bland-Altman showed a good agreement for the arcs measurement [mean difference (standard deviation): 1.2 ± 7.4 degrees for the total arc of attenuation and mean difference (standard deviation): -3.8 ± 9.2 degrees for the total arc of calcium]. Regarding qualitative data, the kappa values for intra-observer agreement on hypoechoic, hyperechoic, mixed, calcified and echo-attenuated plaque characterization were 0.85, 0.92, 0.82, 0.90 and 0.78, respectively.

Intra-observer variability for IVOCT measurements

Intra-observer variability was very low for lumen CSA, minimum and maximum luminal diameters (0.04 ± 0.19 mm^2, 0.03 ± 0.11 mm, 0.04 ± 0.13 mm, respectively) (Figure 3 and on-line supplementary Table S2). Likewise, the mean differences (standard deviation) were negligible for stent CSA, minimum and maximum stent diameters (0.05 ± 0.26 mm^2, 0.02 ± 0.09 mm, 0.03 ± 0.13 mm, respectively). Intra-observer variability was also low for EEM area, atheroma CSA, plaque burden, minimum atheroma thickness, maximum atheroma thickness and atheroma eccentricity index (0.13 ± 0.39 mm^2, 0.08 ± 0.35 mm^2, 0.4 ± 2.0 %, 0.01 ± 0.04 mm, -0.02 ± 0.08 mm, -0.02 ± 0.07, respectively). In the same way, mean differences (standard deviation) were for low IEM area, IEM atheroma CSA, IEM minimum atheroma thickness, IEM maximum atheroma thickness and IEM atheroma eccentricity index (-0.06 ±

0.31 mm^2, -0.10 ± 0.29 mm^2, -0.01 ± 0.03 mm, -0.02 ± 0.04 mm, -0.06 ± 0.16, respectively). Bland-Altman showed a good agreement for the lipid and calcium arcs measurements (1.8 ± 6.8 degrees, -2.4 ± 9.2 degrees, respectively). Furthermore, the mean difference (standard deviation) for the fibrous cap thickness was -3.6 ± 11.6 μm. Regarding qualitative data, the kappa values for intra-observer agreement on fibroatheroma, fibrous, fibrocalcific plaque characterization were 0.83, 0.84 and 0.86, respectively.

Inter-observer variability for IVUS measurements

The ICC was 0.98 (95% CI: 0.97 to 0.99) for lumen CSA, 0.94 (95% CI: 0.92 to 0.96) for minimum lumen diameter and 0.95 (95% CI: 0.90 to 0.98) for maximum lumen diameter (On-line supplementary Table S3). The ICC was 0.98 (95% CI: 0.97 to 0.99) for stent CSA, 0.97 (95% CI: 0.94 to 0.99) for minimum stent diameter and 0.95 (95% CI: 0.93 to 0.97) for maximum stent diameter. In the same way, inter-observer reproducibility was high for EEM area (ICC = 0.92; 95% CI: 0.89 to 0.95), atheroma CSA (ICC = 0.90; 95% CI: 0.86 to 0.93) and good for plaque burden (ICC = 0.88; 95% CI: 0.83 to 0.92), minimum atheroma thickness (ICC = 0.73; 95% CI: 0.63 to 0.81), maximum atheroma thickness (ICC = 0.83; 95% CI: 0.79 to 0.89) and atheroma eccentricity index (ICC = 0.76; 95% CI: 0.67 to 0.83). The ICC for the total arc of attenuation was 0.78 (95% CI: 0.40 to 0.96), whereas the ICC for the total arc of calcium was 0.89 (95% CI: 0.77 to 0.95). Regarding qualitative data, the agreement was excellent for stent identification (κ=1.0), EEM identification under the lesion (κ=0.87), echo-attenuated plaque characterization (κ=0.88), thrombus (κ=1.0), prolapse (κ=1.0), stent malapposition (κ=1.0) and dissection (κ=0.95) detection. Furthermore, the agreement was substantial for hypoechoic plaque (κ=0.75), hyperechoic plaque (κ=0.78), mixed plaque (κ=0.70) and calcified plaque (κ=0.80). No plaque rupture was identified.

Inter-observer variability for IVOCT measurements

The ICC was 0.99 (95% CI: 0.99 to 1.0) for lumen CSA, 0.96 (95% CI: 0.91 to 0.98) for minimum lumen diameter and 0.99 (95% CI: 0.99 to 0.99) for maximum lumen diameter (On-line supplementary Table S4). The ICC was 0.99 (95% CI: 0.99 to 1.0) for stent CSA, 0.98 (95% CI: 0.97 to 0.99) for minimum stent diameter and 0.99 (95% CI: 0.99 to 0.99) for maximum stent diameter. In the same way, inter-observer reproducibility was high for EEM area (ICC = 0.98; 95% CI: 0.96 to 0.99), atheroma CSA (ICC = 0.91; 95% CI: 0.87 to 0.93), plaque burden (ICC = 0.95; 95% CI: 0.91 to 0.98), maximum atheroma thickness (ICC = 0.93; 95% CI: 0.90 to 0.95) and substantial for minimum atheroma thickness (ICC = 0.82; 95% CI: 0.78 to 0.88) and atheroma eccentricity index (ICC = 0.72; 95% CI: 0.61 to 0.80). Likewise, inter-observer reproducibility was high for IEM area (ICC = 0.99; 95% CI: 0.98 to

1.0), IEM atheroma CSA (ICC = 0.96; 95% CI: 0.91 to 0.99), IEM maximum atheroma thickness (ICC = 0.98; 95% CI: 0.96 to 0.99) and good for minimum atheroma thickness (ICC = 0.82; 95% CI: 0.64 to 0.92) and atheroma eccentricity index (ICC = 0.87; 95% CI: 0.68 to 0.95). The ICC for the lipid arc was 0.81 (95% CI: 0.60 to 0.93) and the ICC for the total arc of calcium was 0.89 (95% CI: 0.79 to 0.96). However, the ICC for the fibrous cap thickness measurement was low (ICC = 0.48; 95% CI: 0.08 to 0.81). Regarding qualitative data, the agreement was excellent for stent identification (κ=1.0), IEM identification under the lesion (κ=0.81), thrombus (κ=0.88), prolapse (κ=1.0), stent malapposition (κ=1.0) and dissection (κ=0.91) and the presence of cholesterol crystals (κ=0.93). Furthermore, the agreement was substantial for EEM identification under the lesion (κ=0.79), fibroatheroma (κ=0.76), fibrous plaque (κ=0.78), fibrocalcific plaque (κ=0.80), macrophages presence (κ=0.79) and intimal vessels detection (κ=0.80). As for IVUS, no plaque rupture was detected.

Inter-institute variability for IVUS and IVOCT measurements

Inter-institute mean differences and standard deviations for quantitative IVUS and IVOCT geometrical measurements are shown in Table 2 and in Figure 4. The magnitudes of the measurement differences between the 2 institutes are compared in Table 3. EEM CSA was measured by both institute observers in 90% of the IVUS images and in 40% of the IVOCT corresponding images. In the 40 IVOCT images, where EEM CSA was defined by both institutes' observers, EEM CSA could also be determined in all corresponding IVUS images. The magnitude of inter-institute measurement differences for IVOCT is statistically significantly less than the magnitude of inter-institute measurement differences for IVUS in the following assessments: lumen CSA, maximum and minimum lumen diameters, stent CSA, maximum and minimum stent diameters. When IVOCT measurements were available (i.e. EEM was identified), a similar trend was observed for EEM CSA, atheroma CSA, plaque burden, minimum and maximum atheroma thicknesses (Table 3). Bland-Altman showed a moderate agreement for the IVUS total arc of attenuation [mean difference (standard deviation): 3.8 ± 19.2 degrees] and for the IVUS total arc of calcium [mean difference (standard deviation): -11.4 ± 15.1 degrees]. Regarding IVUS qualitative data, the agreement was excellent for stent identification (κ=1.0), prolapse (κ=1.0), and stent malapposition (κ=1.0). Furthermore, the agreement was substantial for thrombus (κ=0.66) and dissection (κ=0.65). In addition, kappa values for inter-institute agreement on hypoechoic, hyperechoic, mixed, calcified and echo-attenuated plaque characterization were 0.74, 0.78, 0.72, 0.87 and 0.78, respectively. Bland-Altman showed a moderate agreement for the IVOCT lipid and

calcium arcs measurements (-5.3 ± 31.8 degrees, 5.1 ± 24.4 degrees, respectively). Furthermore, the mean difference (standard deviation) for the fibrous cap thickness was -7.9 ± 38.6 μm. Regarding qualitative data, the agreement was excellent for stent identification (κ=1.0), prolapse (κ=1.0), stent malapposition (κ=1.0), macrophages presence (κ=0.88), and the presence of cholesterol crystals (κ=0.85). Furthermore, the agreement was substantial for thrombus (κ=0.72), IEM identification under the lesion (κ=0.73), dissection (κ=0.78), and intimal vessels detection (κ=0.71). In addition, kappa values for inter-institute agreement on fibroatheroma, fibrous, fibrocalcific plaque characterization were 0.76, 0.74 and 0.82, respectively.

Discussion

In the present study, the main finding of our study is that the inter-institute variability of measurements for IVOCT is statistically significantly less than the inter-institute variability of measurements for IVUS in the following assessments: lumen CSA, maximum and minimum lumen diameters, stent CSA, maximum and minimum stent diameters. Furthermore, intra- and inter-observer variability results for both techniques in this study were nearly similar to other studies previously published.

In our study, the inter-institute variability of geometrical measurements for IVOCT is statistically significantly less than for IVUS. The first explanation is that the spatial resolution of IVOCT is greater than the IVUS. Thus, the axial resolution ranges from 10 to 20 μm, compared with 80 to 100 μm for IVUS. Furthermore, the lateral resolution in IVOCT catheters is typically 30 to 50 μm, as compared with 150 to 250 μm for IVUS [6]. Another possible reason for this difference is the superior ability of OCT to visualize the lumen-intima interface compared with IVUS, therefore allowing OCT to visualize the true lumen dimensions, which IVUS can sometimes overestimate [18]. This finding is consistent with that of Magnus et al. who recently observed that IVUS inter-observer variability for measurement of in-stent CSA was significantly higher than IVOCT inter-observer variability (IVUS in-stent CSA: 1.34 mm^2 versus IVOCT in-stent CSA: 0.85 mm^2; p = 0.024) [19]. Moreover, although there was a similar trend in favor of IVOCT for atheroma CSA, plaque burden, atheroma minimum and maximum thicknesses, we acknowledge that EEM under the lesion was clearly less identified by IVOCT compared to IVUS, which is a bias in the results comparison. Thus, IVUS signal penetration (approximately 5 mm) is deeper that IVOCT penetration (around 2 mm). Consequently, although IVUS measurements are probably less consistent that IVOCT, IVUS still appears to be the best technique for evaluating plaque burden and vascular remodeling, regardless of

the composition of the plaque. Concerning plaque composition, the inter-institute agreement for both techniques yielded a substantial concordance. As demonstrated in the present study, assessments by analysts from 2 different centers with the same training program may result in statistically significant minor differences for plaque composition. In trials where both technologies are being increasingly used and where minor changes in plaque composition are expected [5], awareness of the inter-institute difference may be important in the design of a multicentre study.

Using published consensus document definitions, our study evaluated intra- and inter-observer variabilities of both techniques regarding a wide and nearly complete range of quantitative and qualitative data. Previous studies were generally more focused on a specific analysis. Inter-observer IVUS assessments of plaque composition were highly correlated, except possibly for mixed plaque (κ=0.70). Likewise, Palmer et al. showed a high level of agreement except for heterogeneous/mixed plaque (κ=0.78) [9]. We suppose part of this variability may be due to the definition of a mixed plaque. Inter-observer IVOCT reproducibility yielded a very good concordance for all geometry measurements, except for the fibrous cap thickness (ICC = 0.48). Similarly, Kim et al. observed equivalent ICC values emphasizing that it remains challenging to detect the inner border of lipid pool within the plaque for cap measurement [20]. Finally, in our study, the reliability for macrophages, cholesterol crystals and intimal vessels identification was also acceptable. To the best of our knowledge, this finding has never been reported.

Limitations

Our study included a small number of images (n=100) per set. However, the analysis was complete, including a wide range of quantitative and qualitative data using published consensus document definitions. To generate the sets, images with poor quality were excluded, which is a bias of selection. The matching process used in this study may have some imperfections. The adoption of dedicated software can overcome this limitation, such as carpet view analysis of IVOCT images that has been recently described to enable a matching comparison of the same stent portion during serial time points [21]. This study was conducted in two highly experienced centers in intravascular imaging in the USA. The results of this study may not be applicable elsewhere. Analyses were performed offline on selected images of coronary segments from patients with stable angina. Thus, our findings cannot be extrapolated to inter-institute studies in an online setting or in patients with acute coronary syndromes. Our non-commercial IVOCT system is similar to the Terumo FD-OCT imaging system (Lunawave, Terumo, Tokyo, Japan). Finally, parameters like vessel location, vessel

size, plaque burden, calcification, de novo versus stented lesions, flushing media and ECG cycle that could affect differences between IVOCT and IVUS assessments were not incorporated in the analysis.

Conclusion

In the measurement of lumen CSA, maximum and minimum lumen diameters, stent CSA, maximum and minimum stent diameters by analysts from 2 different laboratories, inter-institute reproducibility of IVOCT was found to be more consistent than IVUS. Inter-institute agreement is substantial using both technologies for plaque composition. These findings may have important implications for the design of future studies that pool intravascular imaging parameters evaluated and measured by multiple institutions.

Supplementary Data: Tables S1 and S2 showed intra-observer reproducibility for quantitative IVUS geometrical measurements and for quantitative IVOCT geometrical measurements, respectively. Tables S3 and S4 provided inter-observer reproducibility for quantitative IVUS geometrical measurements and for quantitative IVOCT geometrical measurements, respectively.

Acknowledgements: The authors would like to thank Mireille Rosenberg for her assistance. The research was funding in part by NIH R01HL076398. Dr. Gerbaud has received a grant from the French Federation of Cardiology.

Conflict of interest: G.J.T. Samsung Consultant, receives Royalties from Terumo, receives Sponsored research funding from Canon Inc. and Infraredx. A.M. ACIST and Boston Scientific Consultant.

References

1. Di Mario C, Görge G, Peters R, Kearney P, Pinto F, Hausmann D, et al. Clinical application and image interpretation in intracoronary ultrasound. Study Group on Intracoronary Imaging of the Working Group of Coronary Circulation and of the Subgroup on Intravascular Ultrasound of the Working Group of Echocardiography of the European Society of Cardiology. Eur Heart J 1998; 19:207-229.
2. Mintz GS, Nissen SE, Anderson WD, Bailey SR, Erbel R, Fitzgerald PJ, et al. American College of Cardiology clinical expert consensus document on standards for acquisition, measurement and reporting on intravascular ultrasound studies (IVUS). A report of the American College of Cardiology task force on clinical expert consensus documents. J Am Coll Cardiol 2001; 37:1478-92.
3. Tearney GJ, Regar E, Akasaka T, Adriaenssens T, Barlis P, Bezerra HG, et al. International Working Group for Intravascular Optical Coherence Tomography (IWG-IVOCT). Consensus standards for acquisition, measurement, and reporting of intravascular optical coherence tomography studies. A report from the international working group for intravascular optical coherence tomography standardization and validation. J Am Coll Cardiol 2012; 59:1058-72.
4. Prati F, Guagliumi G, Mintz GS, Costa M, Regar E, Akasaka T, et al. for the Expert's OCT Review Document. Expert review document part 2: methodology, terminology and clinical applications of optical coherence tomography for the assessment of interventional procedures. Eur Heart J 2012; 33:2513-2522.
5. Hartmann M, Huisman J, Böse D, Jensen LO, Schoenhagen P, Mintz GS, et al. Serial intravascular ultrasound assessment of changes in coronary atherosclerotic plaque dimensions and composition: an update. Eur J Echocardiogr 2011; 12:313-321.
6. Bezerra HG, Costa MA, Guaglimi G, Rollins AM, Simon DI. Intracoronary optical coherence tomography: a comprehensive review: clinical and research applications. J Am Coll Cardiol Cardiovasc Interv 2009; 2:1035-1046.
7. Haussmann D, Lundkvist AJS, Friedrich GJ, Mullen WL, Fitzgerald PJ, Yock PG. Intracoronary ultrasound imaging: intraobserver and interobserver variability of morphometric measurements. Am Heart J 1994; 128:674-680.

8. Blessing E, Hausmann D, Sturm M, Wolpers HG, Amende I, Mügge A. Intravascular ultrasound and stent implantation: intraobserver and interobserver variability. Am Heart J 1999; 137:368-71.

9. Palmer ND, Northridge D, Lessells A, McDicken WN, Fox KA. In vitro analysis of coronary atheromatous lesions by intravascular ultrasound; reproducibility and histological correlation of lesion morphology. Eur Heart J 1999; 20:1701-6.

10. Gonzalo N, Garcia-Garcia HM, Serruys PW, Commissaris KH, Bezerra H, Gobbens P, et al. Reproducibility of quantitative optical coherence tomography for stent analysis. Eurointervention 2009; 5:224-232.

11. Fedele S, Biondi-Zoccai G, Kwiatkowski P, Di Vito L, Occhipinti M, Cremonesi A, et al. Reproducibility of coronary optical coherence tomography for lumen and length measurements in humans (The CLI-VAR [Centro per la Lotta contro l'Infarto-VARiability] study. Am J Cardiol 2012; 110:1106-1112.

12. Huisman J, Egede R, Rdzanek A, Böse D, Erbel R, Kochman J, et al. Between-centre reproducibility of volumetric intravascular ultrasound radiofrequency-based analyses in mild-to-moderate coronary atherosclerosis: an international multicentre study. EuroIntervention 2010; 5:925-931.

13. Regar E, Werner F, Siebert U, Rieber J, Thesen K, Mudra H, et al. Reproducibility of neointima quantification with motorized intravascular ultrasound pullback in stented coronary arteries. Am Heart J 2000; 139:632-637.

14. Vakoc B, Yun S, de Boer J, Tearney GJ, Bouma BE. Phase-resolved optical frequency domain imaging. Opt Express 2005; 13:5483-5493.

15. Jamil Z, Tearney G, Bruining G, Sihan K, van Soest G, Lightart J, et al. Interstudy reproducibility of the second generation, Fourier domain optical coherence tomography in patients with coronary artery disease and comparison with intravascular ultrasound: a study applying automated contour détection. Int J Cardiovasc Imaging 2013; 29:39-51.

16. Schneider CA, Rasband WS, Eliceiri KW. NIH Image to ImageJ: 25 years of image analysis. Nat Methods 2012; 9:671-675.

17. Landis JR, Koch GG. The measurement of observer agreement for categorical data. Biometrics 1977; 33:159-174.

18. Kubo T, Akasaka T, Shite J, Suzuki T, Uemura S, Kozuma K, et al. OCT compared with IVUS in a coronary lesion assessment. The OPUS-CLASS study. J Am Coll Cardiol Img 2013; 6:1095-11.

19. Magnus PC, Jayne JE, Garcia-Garcia HM, Swart M, van Es GA, Tijssen J, et al. Optical coherence tomography vs intravascular ultrasound in the evaluation of observer variability and reliability in the assessment of stent deployment: The OCTIVUS Study. Catheter Cardiovasc Interv 2015 Jan 23. doi: 10.1002/ccd.25854.

20. Kim SJ, Lee H, Kato K, Yonetsu T, Xing L, Zhang S, et al. Reproducibility of in vivo measurements for fibrous cap thickness and lipid arc by OCT. J Am Coll Cardiol Img 2012; 5:1072-4.

21. Gabriele A, Marco V, Gatto L, Paoletti G, Di Vito L, Castriota F, et al. Reproducibility of the carpet view system: a novel technical solution for display and off line analysis of OCT images. Int J Cardiovasc Img 2014; 30:1225-33.

Table 1. Design of the study

	Institute	First read data set	Second read data set (one month later)
Observer 1	CRF	IVUS H	IVUS G
Observer 2	CRF	OFDI O	No
Observer 3	MGH	IVUS A	No
		OFDI J	OFDI L
Observer 4	MGH	IVUS F	No
		OFDI P	No

Intra-, inter-observer and inter-institute variabilities were assessed as follows: intra-observer variability for IVUS measurements: IVUS H analysis versus IVUS G analysis; intra-observer variability for OFDI measurements: OFDI J analysis versus OFDI L analysis; inter-observer variability for IVUS measurements: IVUS H analysis versus IVUS A analysis versus IVUS F analysis; inter-observer variability for OFDI measurements: OFDI O analysis versus OFDI J analysis versus OFDI P analysis; inter-institute variability for IVUS measurements: IVUS H analysis versus IVUS F analysis; inter-institute variability for OFDI measurements: OFDI O analysis versus OFDI P analysis. For each set, the new order of images was obtained using web-based randomization software. MGH: Massachusetts General Hospital; CRF: Columbia Research Foundation.

Table 2. Inter-institute reproducibility for quantitative IVUS and OFDI geometrical measurements.

	IVUS CRF Observer 1	IVUS MGH Observer 4	Mean Difference IVUS	OFDI CRF Observer 2	OFDI MGH Observer 4	Mean Difference OFDI
Lumen CSA (mm^2)	7.06 ± 2.81	6.87 ± 2.75	0.19 ± 0.65	6.86 ± 2.79	6.91 ± 2.90	-0.06 ± 0.32
Lumen max. diameter (mm)	3.10 ± 0.68	3.19 ± 0.63	-0.09 ± 0.22	3.13 ± 0.63	3.09 ± 0.66	0.04 ± 0.10
Lumen min. diameter (mm)	2.65 ± 0.52	2.63 ± 0.50	0.02 ± 0.28	2.64 ± 0.56	2.66 ± 0.60	-0.02 ± 0.17
Stent CSA (mm^2)	7.94 ± 3.29	7.84 ± 3.30	0.10 ± 0.60	7.60 ± 3.26	7.65 ± 3.22	-0.05 ± 0.25
Stent max. diameter (mm)	3.31 ± 0.72	3.26 ± 0.75	0.05 ± 0.18	3.18 ± 0.64	3.15 ± 0.64	0.03 ± 0.10
Stent min. diameter (mm)	2.94 ± 0.63	2.98 ± 0.63	-0.04 ± 0.12	2.91 ± 0.62	2.92 ± 0.65	0.01 ± 0.08
EEM CSA (mm^2) *	12.26 ± 2.97	12.06 ± 2.57	0.20 ± 1.11	11.07 ± 2.61	10.96 ± 2.92	0.11 ± 0.70
Atheroma CSA (mm^2) *	5.79 ± 2.36	5.92 ± 2.30	-0.13 ± 1.05	4.83 ± 1.41	4.71 ± 1.43	0.11 ± 0.74
Plaque burden (%)	46.6 ± 14.3	48.8 ± 15.4	-2.2 ± 6.8	43.9 ± 11.7	43.3 ± 10.7	0.6 ± 3.3
Max. atheroma thickness (mm) *	0.85 ± 0.25	0.79 ± 0.25	0.06 ± 0.18	0.71 ± 0.27	0.74 ± 0.29	-0.03 ± 0.12
Min. atheroma thickness (mm) *	0.33 ± 0.14	0.29 ± 0.14	0.04 ± 0.14	0.27 ± 0.09	0.24 ± 0.08	0.03 ± 0.05
Atheroma eccentricity index *	0.59 ± 0.16	0.61 ± 0.18	-0.02 ± 0.15	0.59 ± 0.17	0.62 ± 0.12	-0.03 ± 0.13

Values are expressed as mean ± standard deviation. Mean (relative) differences (bias) and standard deviations were calculated according to the methods of Bland and Altman. CSA: indicates cross section area; EEM: external elastic membrane; Max: maximal; Min: minimal; MGH: Massachusetts General Hospital; CRF: Columbia Research Foundation. Atheroma CSA was calculated as EEM CSA – lumen CSA. Plaque burden was calculated as (Atheroma CSA / EEM CSA) X 100 (%). Atheroma eccentricity index was calculated as (Maximum atheroma thickness – Minimum atheroma thickness) / Maximum atheroma thickness. * in the 40 OFDI images, where EEM CSA was measured by both institute observers, EEM CSA could also be determined in all corresponding IVUS images.

Table 3. Comparison between inter-institute measurement differences magnitudes for quantitative IVUS and OFDI geometrical measurements.

	Inter-institute Measurement Differences Magnitude for IVUS	Inter-institute Measurement Differences Magnitude for OFDI	*P* value
Lumen CSA (mm^2)	0.33 (0.12-0.67)	0.10 (0.05-0.22)	< .001
Lumen max. diameter (mm)	0.16 (0.06-0.30)	0.06 (0.03-0.10)	< .001
Lumen min. diameter (mm)	0.12 (0.06-0.27)	0.04 (0.02-0.08)	< .001
Stent CSA (mm^2)	0.26 (0.20-0.50)	0.17 (0.10-0.30)	0.02
Stent max. diameter (mm)	0.16 (0.09-0.20)	0.05 (0.03-0.09)	< .001
Stent min. diameter (mm)	0.10 (0.03-0.14)	0.04 (0.01-0.08)	0.01
EEM CSA (mm^2) *	0.86 (0.39-1.28)	0.18 (0.05-0.36)	0.007
Atheroma CSA (mm^2) *	0.68 (0.53-1.05)	0.17 (0.06-0.34)	0.02
Plaque burden (%)	5.6 (2.2-7.3)	1.9 (0.4-2.1)	0.002
Max. atheroma thickness (mm) *	0.14 (0.07-0.20)	0.06 (0.03-0.14)	0.03
Min. atheroma thickness (mm) *	0.07 (0.03-0.10)	0.03 (0.01-0.05)	0.01
Atheroma eccentricity index *	0.07 (0.04-0.15)	0.06 (0.04-0.11)	0.42

Values are expressed as median (interquartile range). CSA: indicates cross section area; EEM: external elastic membrane; Max: maximal; Min: minimal. Atheroma CSA was calculated as EEM CSA –lumen CSA. Plaque burden was calculated as (Atheroma CSA / EEM CSA) X 100 (%). Atheroma eccentricity index was calculated as (Maximum atheroma thickness – Minimum atheroma thickness) / Maximum atheroma thickness. P value indicates the use of a Wilcoxon signed rank to compare IVUS and OFDI inter-institute mean differences magnitudes. * in the 40 OFDI images, where EEM CSA was measured by both institute observers, EEM CSA could also be determined in all corresponding IVUS images.

Figure legends:

Figure 1: Example of IVUS measurements. Lumen and EEM areas are delineated. The minimum and maximum lumen diameters are illustrated using a double-headed arrow (open and solid arrowheads, respectively). Furthermore, the minimum and maximum atheroma thickness is illustrated using double headed arrows (white for minimum and black for maximum).

Figure 2: Example of IVOCT measurements. This IVOCT image was matched with the IVUS image presented in Figure 1. Lumen and EEM areas are traced. The minimum and maximum lumen diameters are illustrated using a double-headed arrow (open and solid arrowheads, respectively). Furthermore, the minimum and maximum atheroma thickness is illustrated using double headed arrows (white for minimum and black for maximum).

Figure 3: Intra-observer variability of lumen CSA, stent CSA and atheroma CSA for IVUS and IVOCT measurements. Middle line: mean difference; top and bottom dotted lines: mean +1.96 SD and mean – 1.96 SD, respectively.

Figure 4: Inter-institute variability of lumen CSA, stent CSA and atheroma CSA for IVUS and IVOCT measurements. Middle line: mean difference; top and bottom dotted lines: mean +1.96 SD and mean – 1.96 SD, respectively.

Figure 1

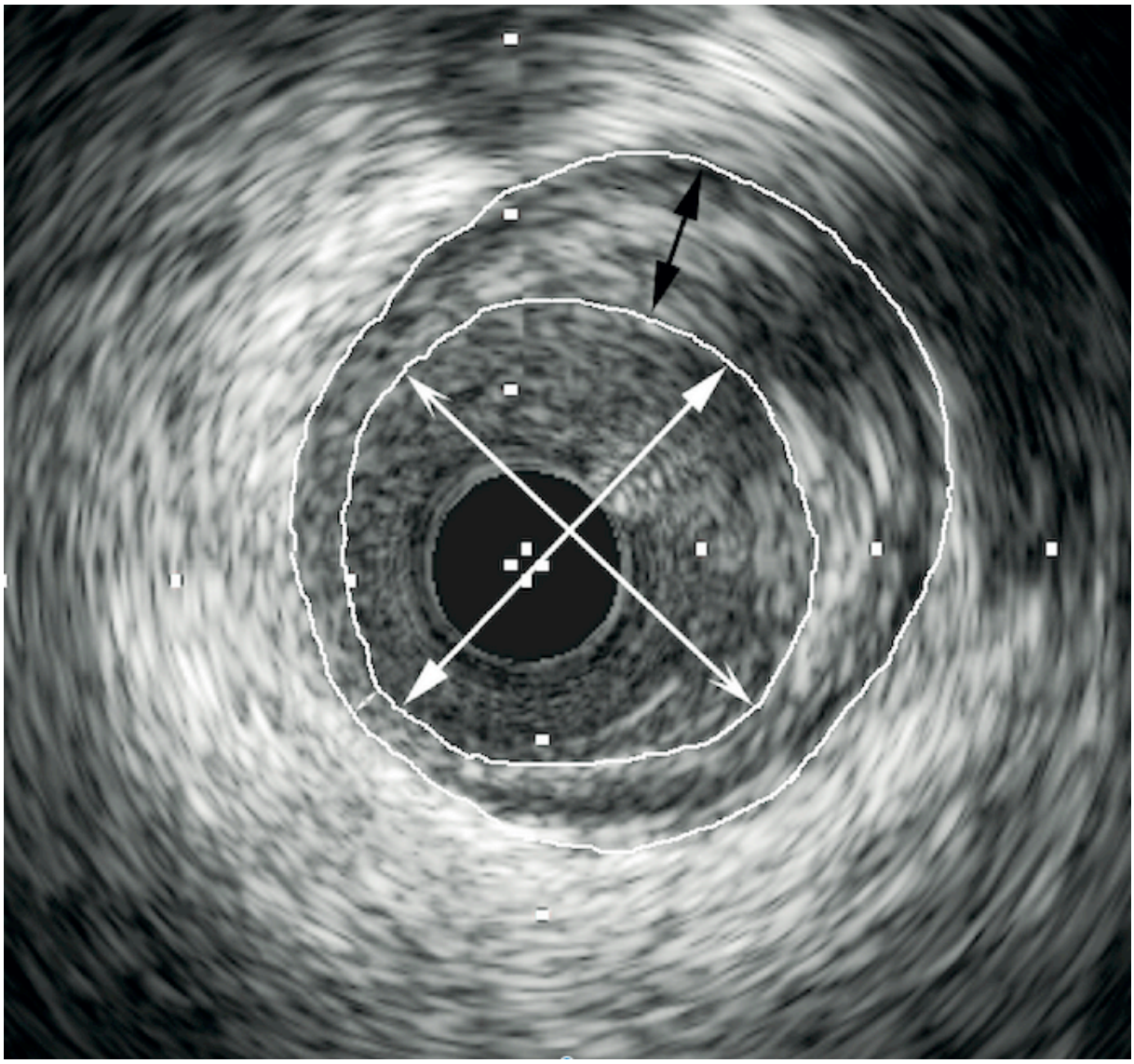

Figure 2

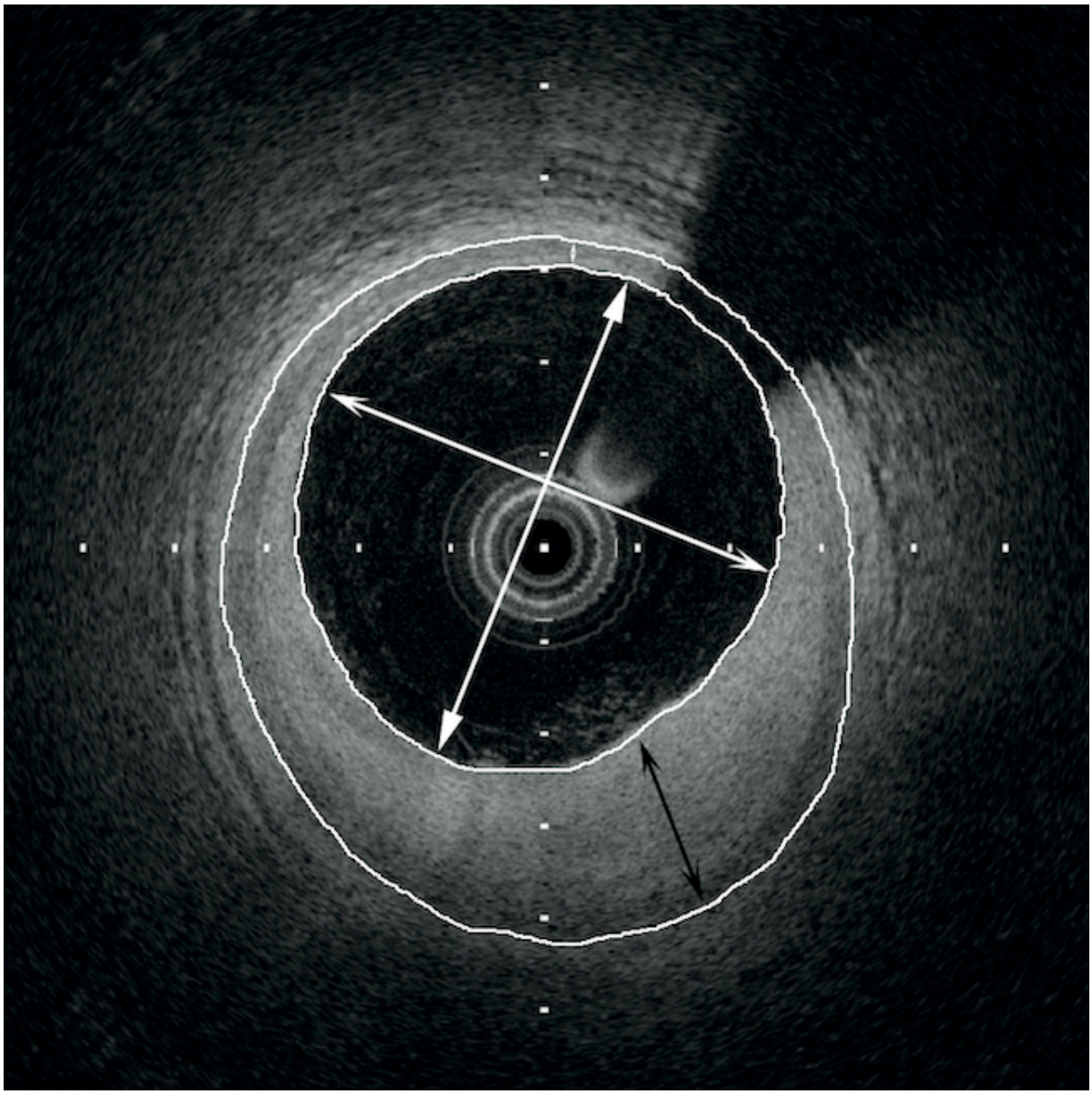

Figure 3

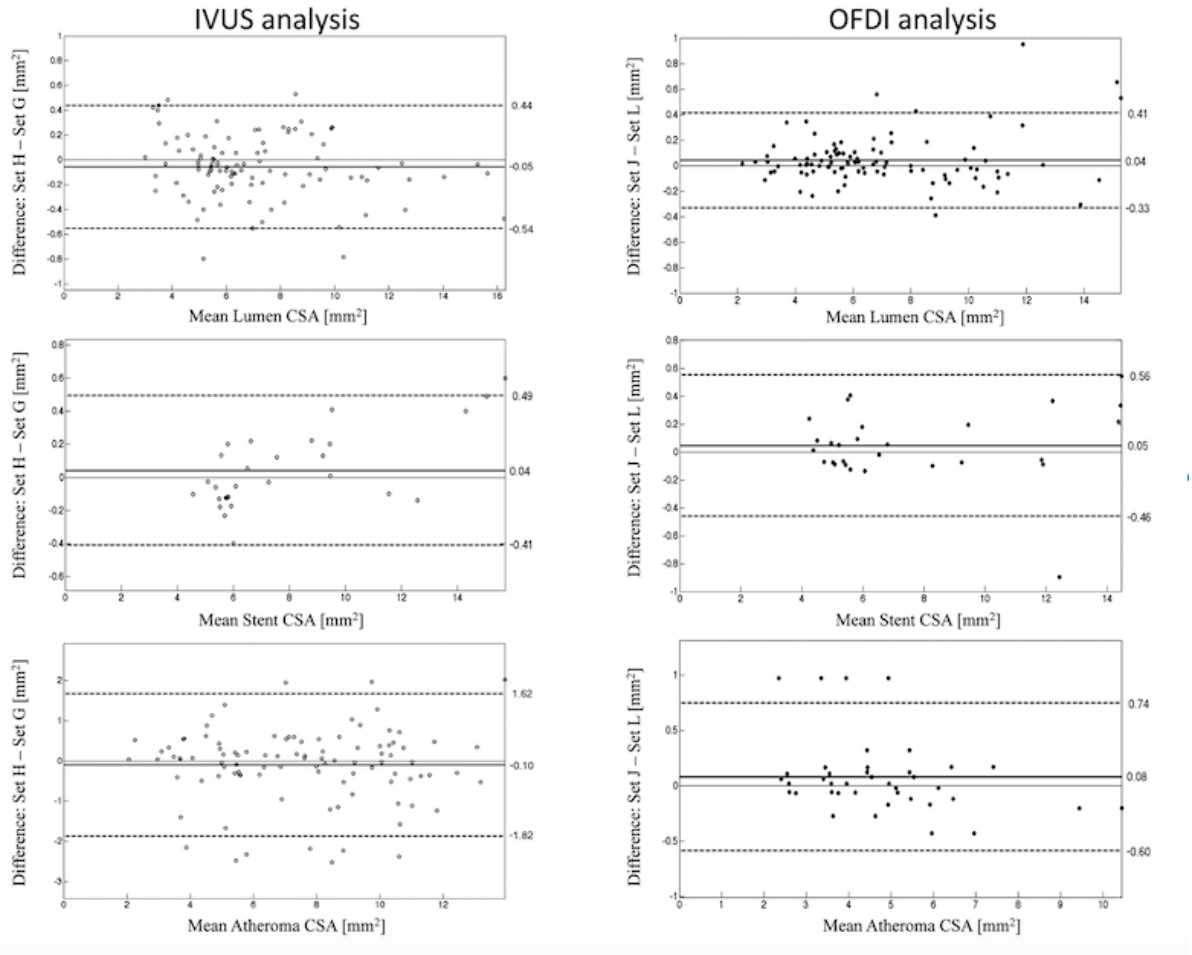
IVUS analysis
OFDI analysis
Difference: Set H – Set G [mm²]
Difference: Set J – Set L [mm²]
Mean Lumen CSA [mm²]
Mean Stent CSA [mm²]
Mean Atheroma CSA [mm²]
0.44
-0.05
-0.54
0.41
0.04
-0.33
0.49
0.04
-0.41
0.56
0.05
-0.46
1.62
-0.10
-1.82
0.74
0.08
-0.60

Figure 4

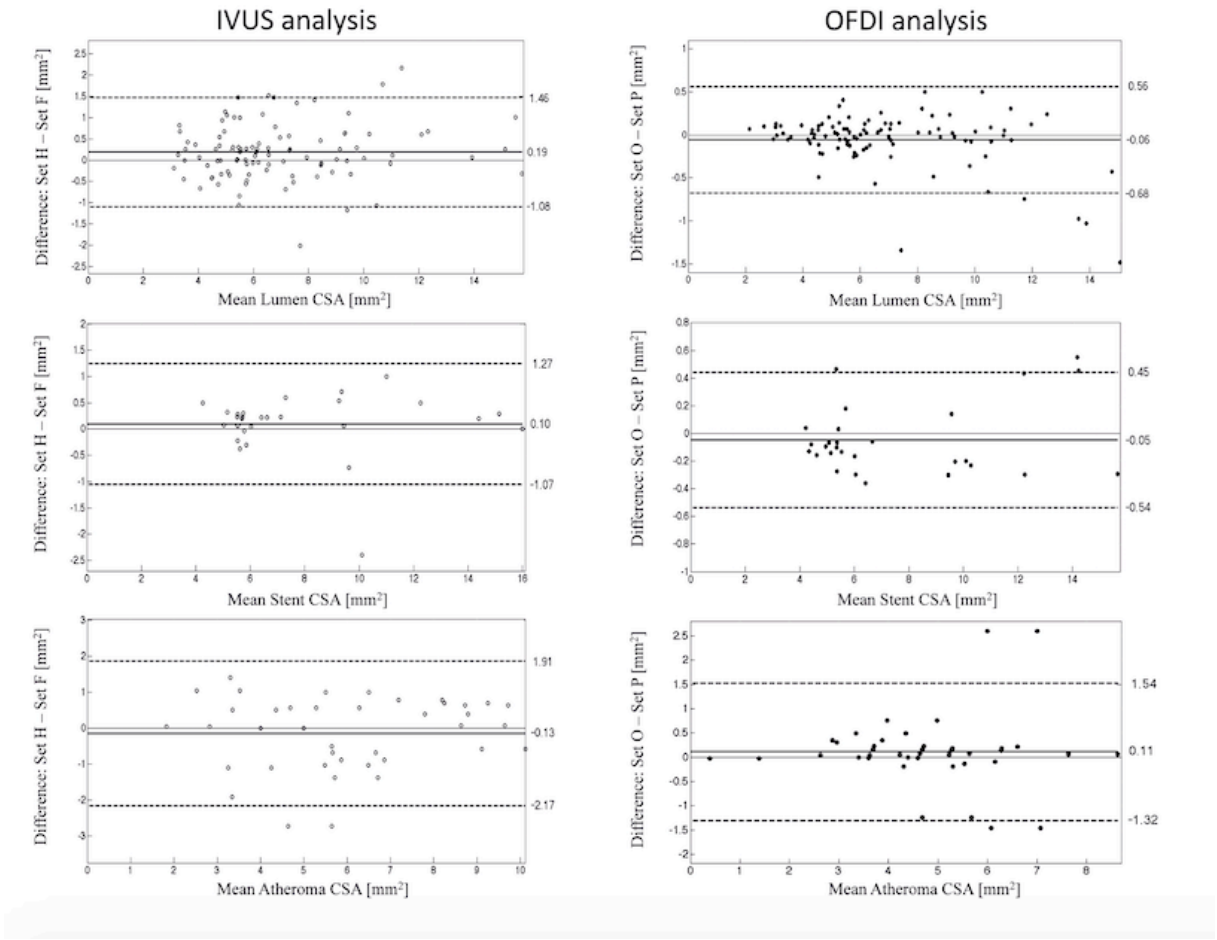
IVUS analysis
OFDI analysis
Difference: Set H – Set F [mm²]
Difference: Set O – Set P [mm²]
Mean Lumen CSA [mm²]
Mean Stent CSA [mm²]
Mean Atheroma CSA [mm²]
1.46
0.19
-1.08
1.27
0.10
-1.07
1.91
-0.13
-2.17
0.56
-0.06
-0.68
0.45
-0.05
-0.54
1.54
0.11
-1.32

Table S1. Intra-observer reproducibility for quantitative IVUS geometrical measurements.

	IVUS CRF Observer 1 (First read)	IVUS CRF Observer 1 (Second read)	Mean Difference IVUS
Lumen CSA (mm^2)	7.06 ± 2.81	7.12 ± 2.85	-0.05 ± 0.25
Lumen max. diameter (mm)	3.10 ± 0.68	3.14 ± 0.68	-0.04 ± 0.21
Lumen min. diameter (mm)	2.65 ± 0.52	2.68 ± 0.51	-0.03 ± 0.09
Stent CSA (mm^2)	7.94 ± 3.29	7.90 ± 3.27	0.04 ± 0.23
Stent max. diameter (mm)	3.31 ± 0.72	3.28 ± 0.73	0.03 ± 0.11
Stent min. diameter (mm)	2.94 ± 0.63	2.94 ± 0.64	0.004 ± 0.13
EEM CSA (mm^2) *	14.50 ± 4.56	14.66 ± 4.47	-0.15 ± 0.87
Atheroma CSA (mm^2) *	7.47 ± 2.84	7.57 ± 2.84	-0.10 ± 0.88
Plaque burden (%)	52.7 ± 23.5	52.7 ± 22.8	-0.02 ± 3.1
Max. atheroma thickness (mm) *	1.17 ± 0.39	1.19 ± 0.38	-0.02 ± 0.20
Min. atheroma thickness (mm) *	0.31 ± 0.15	0.30 ± 0.16	0.01 ± 0.06
Atheroma eccentricity index *	0.72 ± 0.15	0.73 ± 0.14	-0.02 ± 0.07

Values are expressed as mean ± standard deviation. Mean (relative) differences (bias) and standard deviations were calculated according to the methods of Bland and Altman. CSA: indicates cross section area; EEM: external elastic membrane; Max: maximal; Min: minimal; CRF: Columbia Research Foundation; IVUS: intravascular ultrasound. Atheroma CSA was calculated as EEM CSA – lumen CSA. Plaque burden was calculated as (Atheroma CSA / EEM CSA) X 100 (%). Atheroma eccentricity index was calculated as (Maximum atheroma thickness – Minimum atheroma thickness) / Maximum atheroma thickness. * In the images, where EEM was identified by the observer.

Table S2. Intra-observer reproducibility for quantitative OFDI geometrical measurements.

	OFDI MGH Observer 3 (First read)	OFDI MGH Observer 3 (Second read)	Mean Difference MGH
Lumen CSA (mm^2)	6.92 ± 2.91	6.88 ± 2.91	0.04 ± 0.19
Lumen max. diameter (mm)	3.12 ± 0.66	3.08 ± 0.66	0.04 ± 0.13
Lumen min. diameter (mm)	2.69 ± 0.60	2.66 ± 0.58	0.03 ± 0.11
Stent CSA (mm^2)	7.71 ± 3.27	7.67 ± 3.26	0.05 ± 0.26
Stent max. diameter (mm)	3.16 ± 0.68	3.13 ± 0.66	0.03 ± 0.13
Stent min. diameter (mm)	2.94 ± 0.68	2.92 ± 0.64	0.02 ± 0.09
EEM CSA (mm^2) *	11.06 ± 2.81	10.93 ± 2.85	0.13 ± 0.39
Atheroma CSA (mm^2) *	4.74 ± 1.52	4.66 ± 1.62	0.08 ± 0.35
Plaque burden (%)	43.3 ± 11.4	42.9 ± 11.4	0.4 ± 2.0
Max. atheroma thickness (mm) *	0.76 ± 0.28	0.78 ± 0.26	-0.02 ± 0.08
Min. atheroma thickness (mm) *	0.25 ± 0.10	0.24 ± 0.11	0.01 ± 0.04
Atheroma eccentricity index *	0.64 ± 0.16	0.65 ± 0.19	-0.02 ± 0.07

Values are expressed as mean ± standard deviation. Mean (relative) differences (bias) and standard deviations were calculated according to the methods of Bland and Altman. CSA: indicates cross section area; EEM: external elastic membrane; Max: maximal; Min: minimal; MGH: Massachusetts General Hospital; OFDI: optical frequency domain imaging. Atheroma CSA was calculated as EEM CSA – lumen CSA. Plaque burden was calculated as (Atheroma CSA / EEM CSA) X 100 (%). Atheroma eccentricity index was calculated as (Maximum atheroma thickness – Minimum atheroma thickness) / Maximum atheroma thickness. * In the images, where EEM was identified by the observer.

Table S3. Inter-observer reproducibility for quantitative IVUS geometrical measurements.

	IVUS Observer 1	IVUS Observer 3	IVUS Observer 4	Inter-observer ICC (95% CI)
Lumen CSA (mm^2)	7.06 ± 2.81	6.90 ± 2.80	6.87 ± 2.75	0.98 (0.97-0.99)
Lumen max. diameter (mm)	3.10 ± 0.68	3.18 ± 0.76	3.19 ± 0.63	0.95 (0.90-0.98)
Lumen min. diameter (mm)	2.65 ± 0.52	2.66 ± 0.54	2.63 ± 0.50	0.94 (0.92-0.96)
Stent CSA (mm^2)	7.94 ± 3.29	7.79 ± 3.22	7.84 ± 3.30	0.98 (0.97-0.99)
Stent max. diameter (mm)	3.31 ± 0.72	3.27 ± 0.66	3.26 ± 0.75	0.95 (0.93-0.97)
Stent min. diameter (mm)	2.94 ± 0.63	3.00 ± 0.60	2.98 ± 0.63	0.97 (0.94-0.99)
EEM CSA (mm^2) *	14.57 ± 4.51	13.94 ± 4.25	13.90 ± 4.13	0.92 (0.89-0.95)
Atheroma CSA (mm^2) *	7.61 ± 4.25	7.11 ± 3.96	7.19 ± 3.88	0.90 (0.86-0.93)
Plaque burden (%)	50.4 ± 17.8	49.8 ± 17.5	50.2 ± 16.3	0.88 (0.83-0.92)
Max. atheroma thickness (mm) *	1.15 ± 0.36	1.02 ± 0.35	1.04 ± 0.35	0.83 (0.79-0.89)
Min. atheroma thickness (mm) *	0.30 ± 0.14	0.26 ± 0.13	0.31 ± 0.16	0.73 (0.63-0.81)
Atheroma eccentricity index *	0.71 ± 0.15	0.72 ± 0.14	0.68 ± 0.16	0.76 (0.67-0.83)

Values are expressed as mean ± standard deviation. Mean (relative) differences (bias) and standard deviations were calculated according to the methods of Bland and Altman. CSA: indicates cross section area; EEM: external elastic membrane; Max: maximal; Min: minimal; IVUS: intravascular ultrasound; ICC: intraclass correlation coefficient. 95% CI: 95% confidence interval. Atheroma CSA was calculated as EEM CSA – lumen CSA. Plaque burden was calculated as (Atheroma CSA / EEM CSA) X 100 (%). Atheroma eccentricity index was calculated as (Maximum atheroma thickness – Minimum atheroma thickness) / Maximum atheroma thickness. * in the 90 IVUS images, where EEM CSA was measured by all observers.

Table S4. Inter-observer reproducibility for quantitative OFDI geometrical measurements.

	OFDI Observer 2	OFDI Observer 3	OFDI Observer 4	Inter-observer ICC (95% CI)
Lumen CSA (mm^2)	6.86 ± 2.79	6.92 ± 2.91	6.91 ± 2.90	0.99 (0.99-1.0)
Lumen max. diameter (mm)	3.13 ± 0.63	3.12 ± 0.66	3.09 ± 0.66	0.99 (0.99-0.99)
Lumen min. diameter (mm)	2.64 ± 0.56	2.69 ± 0.60	2.66 ± 0.60	0.96 (0.91-0.98)
Stent CSA (mm^2)	7.60 ± 3.26	7.71 ± 3.27	7.65 ± 3.22	0.99 (0.99-1.0)
Stent max. diameter (mm)	3.18 ± 0.64	3.16 ± 0.68	3.15 ± 0.64	0.99 (0.99-0.99)
Stent min. diameter (mm)	2.91 ± 0.62	2.94 ± 0.68	2.92 ± 0.65	0.98 (0.97-0.99)
EEM CSA (mm^2) *	11.07 ± 2.61	10.93 ± 2.73	10.96 ± 2.92	0.98 (0.96-0.99)
Atheroma CSA (mm^2) *	4.83 ± 1.41	4.72 ± 1.37	4.71 ± 1.43	0.91 (0.87-0.93)
Plaque burden (%)	43.9 ± 11.7	43.6 ± 11.4	43.3 ± 10.7	0.95 (0.91-0.98)
Max. atheroma thickness (mm) *	0.71 ± 0.27	0.76 ± 0.28	0.74 ± 0.29	0.93 (0.90-0.95)
Min. atheroma thickness (mm) *	0.27 ± 0.09	0.25 ± 0.10	0.24 ± 0.08	0.82 (0.78-0.88)
Atheroma eccentricity index *	0.58 ± 0.19	0.64 ± 0.15	0.64 ± 0.13	0.72 (0.61-0.80)

Values are expressed as mean ± standard deviation. Mean (relative) differences (bias) and standard deviations were calculated according to the methods of Bland and Altman. CSA: indicates cross section area; EEM: external elastic membrane; Max: maximal; Min: minimal; OFDI: optical frequency domain imaging; ICC: intraclass correlation coefficient. 95% CI: 95% confidence interval. Atheroma CSA was calculated as EEM CSA – lumen CSA. Plaque burden was calculated as (Atheroma CSA / EEM CSA) X 100 (%). Atheroma eccentricity index was calculated as (Maximum atheroma thickness – Minimum atheroma thickness) / Maximum atheroma thickness. * in the 40 OFDI images, where EEM CSA was measured by all observers.

3.1 Definition

Although stable atherosclerotic disease has a clinically silent course, its thrombotic complications, acute coronary syndromes (ACSs), occur suddenly. Serial angiographic studies have shown that lesions responsible for ACSs are often non-occlusive. Consequently, the concepts of the vulnerable plaque, defined as a plaque with a high risk of causing an ACS, and vulnerable patient were introduced. However, the identification of high-risk plaque characteristics has failed to significantly increase the predictive ability of current models for the assessment of cardiovascular risk. Interestingly, few vulnerable plaques actually rupture and even fewer lead to an event, with most plaque ruptures being clinically silent. Two major pathological substrates have been demonstrated by pathology: plaque rupture in the majority of the cases and plaque erosion, while a third infrequent mechanism, consisting of thrombosis on the ground of protruding calcified nodules, has also been suggested [1-3]. A rupture-prone plaque has been characterized by a thin inflamed fibrous cap (65 microns thick), a large necrotic lipid core with abundant inflammatory cells and few smooth muscle cells, as well as spotty calcification and positive outward remodelling. Such a plaque is often described with the term thin-cap fibroatheroma (TCFA), and it is considered to be the major precursor of ACS.

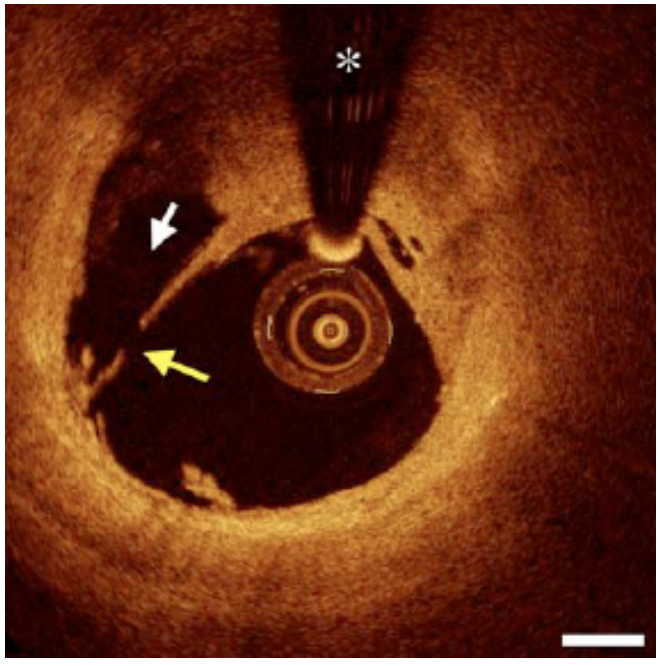

Figure showing a plaque rupture. Dissection of the cap is indicated by a yellow arrow. The cavity is indicated by a white arrow.

Eroded plaques are heterogeneous, scarcely calcified, have lower lipid content than ruptured plaques, and are rarely associated with expansive remodelling, while the presence of inflammation is controversial.

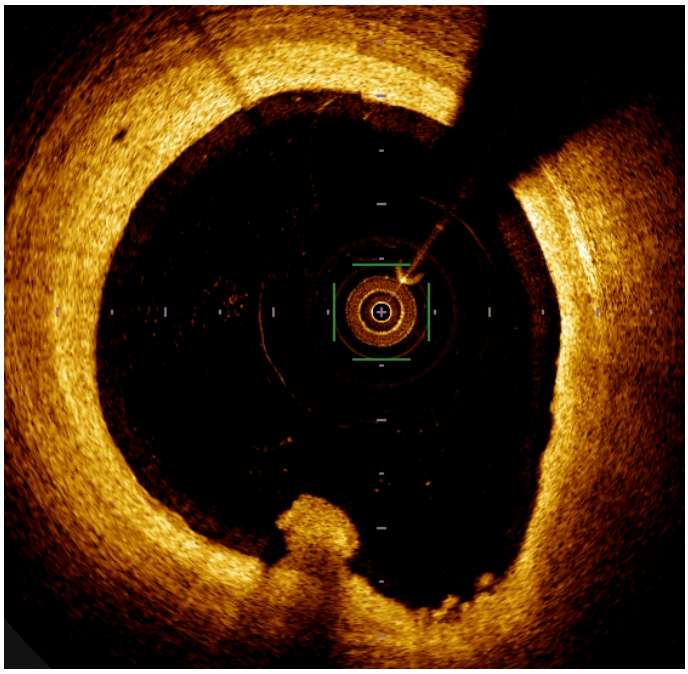

Figure showing as an irregular lumen surface with attached mural thrombus compatible with an erosion.

The least common pathological finding associated with thrombosis is calcified nodules. Calcified nodules are pathologically defined as the presence of fracture of a calcified plate, interspersed fibrin, and a disrupted fibrous cap with an overlying thrombus. Virmani et al. studied over 200 cases of sudden cardiac death. Only one-third of lesions could be described as plaque rupture, and 35% of lesions with thrombi failed to show rupture [1].

3.2 OCT findings in patients presenting with acute coronary syndrome

3.2.1 Ruptured culprit plaque, plaque erosion and calcified nodules

The advent of OCT has boosted the resolving power of intravascular imaging to a level where imaging all these different substrates including the thickness of the cap is possible. Thus, the Massachusetts General Hospital OCT Registry sought to identify specific morphological characteristics of ruptured culprit plaques (RCP) responsible for acute events,

and compare them with ruptured nonculprit plaques (RNCP) and nonruptured thin-cap fibroatheroma (TCFA) in patients presenting with ACS. Tian J et al. analyzed 126 plaques (RCP = 49, RNCP = 19, TCFA = 58) from 82 ACS patients using optical coherence tomography (OCT) and intravascular ultrasound (IVUS) [4]. Fibrous cap thickness was determined by OCT. Plaque burden and lumen area were measured with IVUS. They found that fibrous cap was thinner in RCP (43 ± 11 μm) and RNCP (41 ± 10 μm) than in TCFA (56 ± 9 ± 9 μm, $p < 0.001$ and $p < 0.001$, respectively). Plaque burden was greater in RCP (82 ± 7.2%), compared with RNCP (64 ± 7.2%, $p < 0.001$) and TCFA (62 ± 12.5%, $p < 0.001$). Lumen area was smaller in RCP (2.1 ± 0.9 mm2), compared with RNCP (4.6 ± 2.3 mm2, $p = 0.001$) and TCFA (5.1 ± 2.7 mm2, $p < 0.001$). The fibrous cap thickness <52 mm had good performance in discriminating ruptured plaque from TCFA (area under the curve [AUC] = 0.857, $p < 0.001$) and plaque burden >76% and lumen area <2.6 mm2 had good performance in discriminating RCP from RNCP and TCFA (AUC = 0.923, $p < 0.001$ and AUC = 0.881, $p < 0.001$, respectively). These findings suggest that plaque rupture is determined by fibrous cap thickness, and a combination of large plaque burden and luminal narrowing result in ACS. Another study performed by the same team evaluated using OCT the morphological characteristics of OCT-determined plaque erosion and calcified nodules in patients presenting with ACS. They observed that OCT-erosion is a common finding, particularly in those patients with non-ST-segment elevation ACS and in younger patients, whereas calcified nodules were frequently found in older patients [5]. Both in vivo studies were very interesting to confirm ex-vivo observations. However, all these morphological results do not provide sufficient criteria to identify vulnerable plaques.

3.2.2 Vasa vasorum neovascularization

Furthermore, previous studies suggested that intraplaque bleedings are associated with plaque progression and vulnerability [6]. In this context, angiogenesis originates from the vasa-vasorum in the adventitia. In the same way, a recent OCT study conducted by Taruya A et al. evaluated the relationship between vasa vasorum structures and plaque characteristics of the proximal left descending coronary artery in 53 patients. They observed 2 predominant vasa vasorum patterns at the plaque rupture sites. First, the prevalence of vasa vasorum internal running was 70.0% at the plaque rupture sites. Second, they demonstrated that a distinct pattern of vasa vasorum arborization named «coral tree pattern» was present in 80.0

% of plaque rupture sites [7]. This type of pattern showed also higher average macrophage grade per slice (semi quantified macrophage grading system). Interestingly, despite that this pilot study had some limitations, the authors conclude that imaging for microvasculature could become a new window for plaque vulnerability.

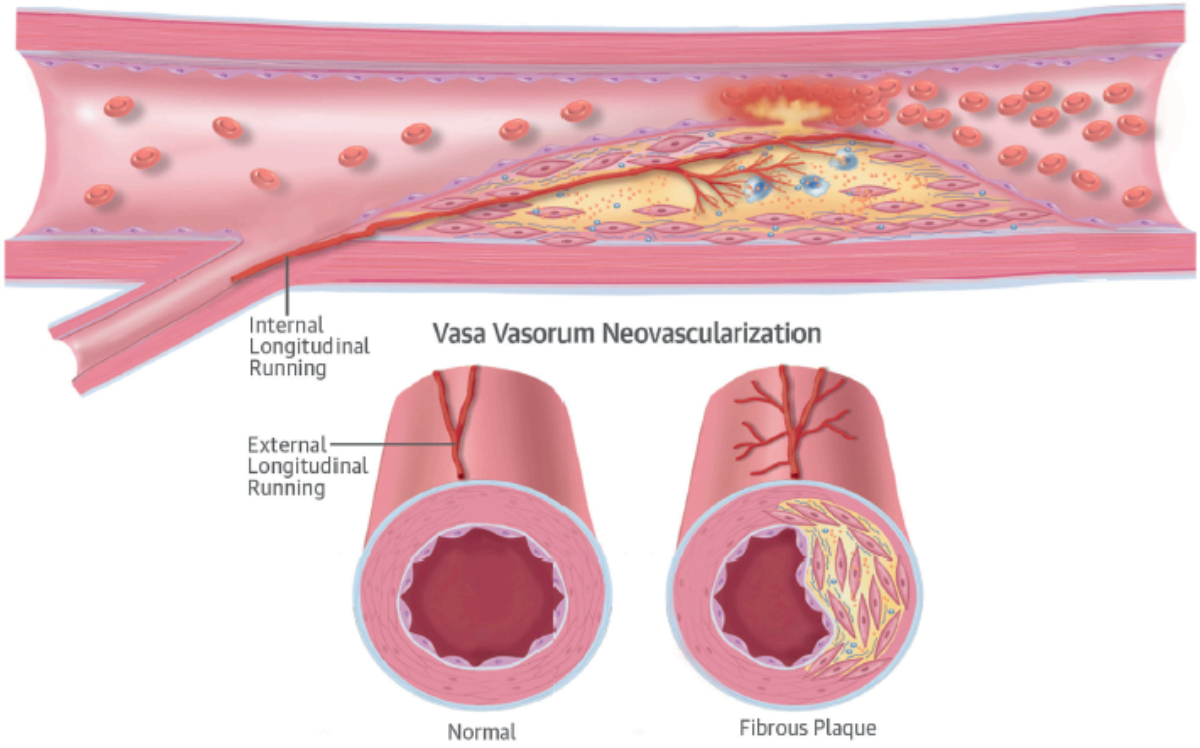

Scheme illustrating the vasa vasorum neovascularization. Vasa vasorum arises from the lumen of the normal coronary artery. This external longitudinal running structure can be seen in every plaque's characteristics. In the case of fibrous plaque, vasa vasorum increases with fibrous plaque growth. In the case of fibroatheroma, an internal longitudinal running structure of intraplaque neovessels emerges according to changes in plaque characteristics. Coronary artery would supplement vasa vasorum with neovascularization of the internal longitudinal running in response to active demand of oxygen and nutrients. In the case of plaque rupture, the coral tree pattern of intraplaque neovessels is from the adventitia or coronary artery branches following a pattern of arborisation and entering plaque. The leaky structure of the coral tree pattern could become a break point for plaque rupture or the main source for necrotic core of a vulnerable plaque. Adapted from Taruya A et al. J Am Coll Cardiol 2015; 65:2469-77.

3.2.3 Macrophages and intravascular OCT bright spots

In addition, cellularity of fibrous caps of atherosclerotic plaque, manifested by the infiltration of macrophages (average size, 20 to 50 μm), is suspected to weaken the structural integrity of the cap and predispose plaques to rupture. Macrophages may produce proteolytic enzymes, such as cathepsins and matrix metalloproteinases that can degrade the fibrous cap and cause thrombosis, the underlying event in clinical atherothrombotic syndromes [8-12]. This evidence suggests that an imaging technology capable of identifying macrophages in patients would provide valuable information for assessing the likelihood of plaque rupture. Thus in 2003, Tearney GJ et al. [13] published a quantitative study that demonstrated that bright spots localised in atherosclerotic plaques on IVOCT images could represent macrophages.

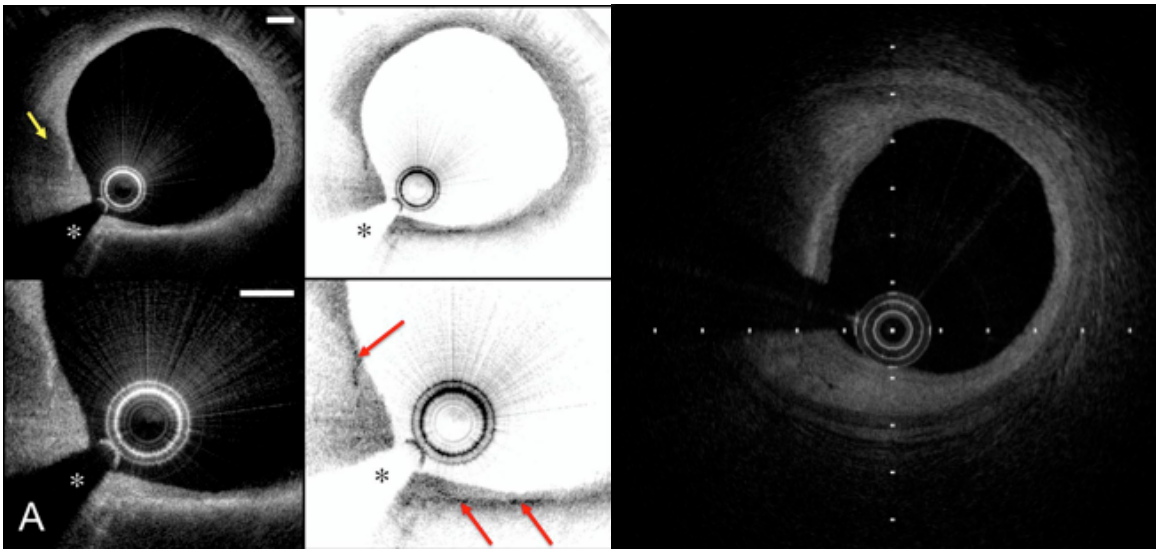

Figure showing punctate, highly scattering focal regions within the plaque (yellow arrow), which may be more readily appreciated by visualizing the images using an inverse gray scale LUT (middle panel, red arrow). Macrophage accumulations can cause shadowing of underlying tissue structure as observed on the right panel.

The same authors also showed that regions with an increased normalized standard deviation (NSD) correlated with areas in human aortic plaque that stained positively for macrophages in immunohistochemical studies. Many years later, Phipps JE et al. studied 1,599 IVOCT images co-registered with histology [14]. Macrophages alone were responsible for only 23% of the bright spot–positive regions, although they were present in 57% of bright spot–positive

regions as determined by histology. However, bright spots in the context of thin-cap fibroatheroma were caused by macrophages in 94% of cases. Additional aetiologies for bright spots included cellular fibrous tissue (8%), interfaces between calcium and fibrous tissue (10%), calcium and lipids (5%), and fibrous cap and lipid pool (3%). Additionally, they showed that large pools of macrophages in $CD68^+$ histology sections corresponded to dark regions in comparative IVOCT images; this result may be explained by the the fact that a pool of lipid-rich macrophages will have the same index of refraction as a pool of lipid and thus will not cause bright spots. In conclusion, these 2 studies performed 12 years apart suggest that a large accumulation of many bright spots within a TCFA may be a new tool to detect vulnerable plaques in patients.

3.3 Lipid-rich coronary artery plaques detection using near-infrared spectroscopy

Besides the structural information offered by the OCT grayscale image, insights into the physiology of the plaque are necessary. While OFDI has been documented to be capable of identifying lipid, the consensus of an international community of experts [15] is that it is not established for distinguishing necrotic core, one of the key features in the most common kind of vulnerable plaque, the TCFA. We therefore seek to add complementary information to OFDI to bring us closer to a single-catheter solution for comprehensive evaluation of coronary pathology *in vivo*.

3.3.1 Spectroscopic optical coherence tomography (SOCT) for automated detection of lipid

One possibility is the use of near-infrared (NIR) spectroscopy which takes advantage the fact that different substances absorb and scatter NIR light (wavelengths from 800 to 2,500 nm) to different degrees at various wavelengths [16]. An NIR spectrometer emits light into a sample and measures the proportion of light that is returned over a wide range of optical wavelengths. The return signal is then plotted as a graph of absorbance (y-axis) at different wavelengths (x-axis) called a spectrum. Absorbance is caused by the loss of NIR light when it interacts with certain molecular bonds (CH, OH, NH, and others) whose vibrational frequency is identical to the frequency of the incoming light. The absorbance spectrum of a

biologic tissue, which is composed of thousands of different chemical entities, is determined by the net result of the absorbances of its individual chemical components. Scattering of NIR light, which differs from absorbance, results from deflections of the light by cellular and extracellular structures. Scattering varies as a function of wavelength and is different for different tissue components. Consequently, the degree of scattering might provide valuable information about the sample. Scattering also permits light to travel an indirect path from the source, through the tissue, and back to the detector. These properties aid the spectroscopic determination of chemical composition. However, one major limitation of this technology is that scattering causes a large loss of the NIR light emitted. Attenuation is the sum of absorption and reduced scattering coefficient. Lipid rich plaques are currently identified within OFDI images as a signal poor region with diffuse boundaries. Because this form of negative contrast can be associated with uncertainty, a method for independently detecting the presence or absence of lipid is highly desirable. Attenuation and backscattering analysis of axial scans using the single scattering model have been used to quantify the difference between fibro-calcific, fibrous, and lipid rich plaques via spectroscopic OCT [17-21].

Christine P. Hendon (Fleming) developed an algorithm using matlab (The MathWorks, Inc.) for automatic detection of lipid within OFDI images based on SOCT [22]. Near infrared basis spectra of pure substances related to plaque vulnerability and intravascular imaging were acquired with the Cary Varian (Agilent Santa Clara, CA) spectrophotometer (Figure 1). Within the OFDI bandwidth of the lightsource used in this study (λ=1300nm, $\Delta\lambda$=100nm), water and cholesterol have nearly linear absorbance spectra. Water absorbance spectrum increased with increasing wavelength whereas cholesterol absorbance spectrum decreased with increasing wavelength (Figure 1). Calcium and collagen had a nearly flat absorbance spectrum over the wavelength region of the light source. Contrast agents i.e. omnipaque and visipaque have similar spectra to water.

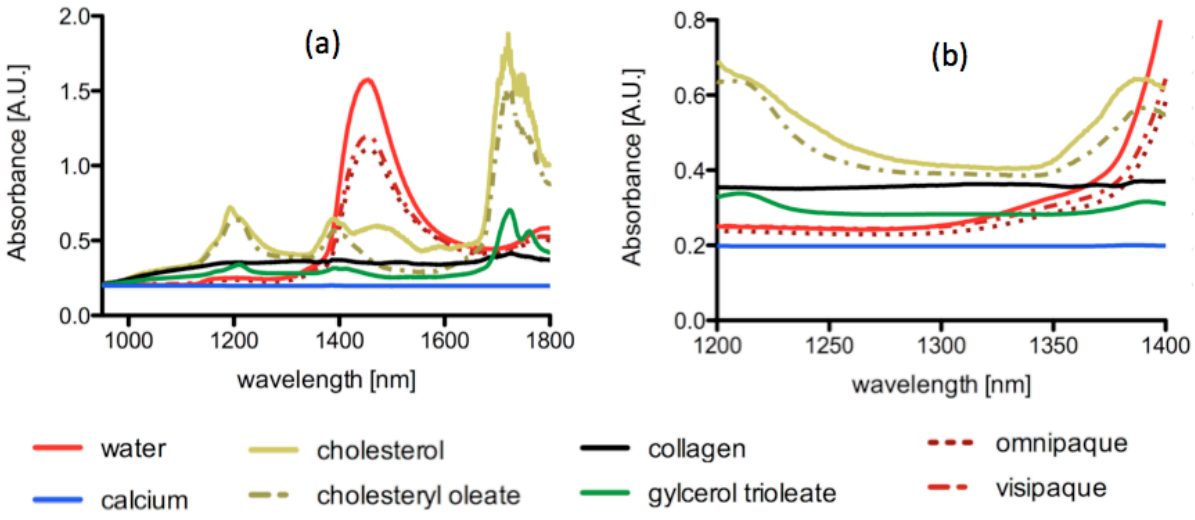

Figure 1 showing on (a) near infrared absorbance spectra of pure substances related to plaque composition and intravascular OCT imaging. The panel (b) depicted absorbance spectra over OFDI source bandwith. Adapted from Fleming CP et al. Biomed Opt Express 2013; 4: 1269-84.

To evaluate the ability of SOCT to detect depth resolved lipid, phantoms of increasing complexity were created using solutions of known chemical compositions and artificial plaques of lipid deposits injected in swine aorta ex vivo. The first set of phantoms comprised of several and different mixtures of cholesterol, collagen, calcium, glycerol trioleate and distilled water to approximate the chemical composition of the plaque. These phantoms were created using solutions of known chemical compositions. All imaging was conducted with a custom built OFDI system, which had a 1300 nm center wavelength, 100 nm bandwith, and 52 kHz axial line rate. The short time Fourier transform was used to generate depth resolved spectra. The spectrograms derived from 64 adjacent axial scans were averaged for final analysis. The single scattering model was used to calculate the attenuation coefficient (from averaged axial lines) and the attenuation spectra (from averaged spectrograms). Pre-processing was used to reduce the variability due to high frequency oscillations and intensity offsets in the attenuation spectra. A Savasky Golay filter, with a 4th order polynomial was used to smooth out the spectra. Use of the standard normal variate reduced intensity differences while maintaining spectral shape.

The preprocessed attenuation spectra can be described as a linear combination of the principal component spectra, PC(λ). For the subsequent analysis, the first three principal

component spectra (PC1(λ), PC2(λ), PC3(λ)) were used for model fitting. Linear least squares analysis was used to find fitting coefficients (c1, c2, and c3) of the principal component spectra to preprocessed attenuation spectra. The image set of cholesterol mixture phantoms was used to develop a prediction model using quadratic discriminant analysis. Inputs to the model included attenuation coefficient and spectral fitting coefficients. Model output was the probability for each pixel being assigned to each of the compositions and the final classification. The principal component spectra used in the model are shown in Figure 2. The first principal component spectrum, PC1, resembles the absorbance spectra of water. The second principal component spectrum resembles the cholesterol absorbance spectra. The figure 2 shows an example preprocessed attenuation spectra, obtained from a 624 μm region overlaid with a modelled spectra consisting of a linear combination of PC1, PC2, and PC3.

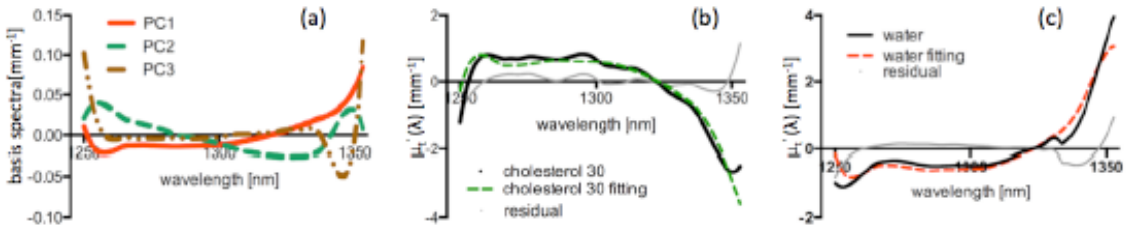

Figure 2 showing modelling attenuation spectra using principal component spectra. (a) Principal component spectra derived from principal component (PC) analysis. The first three PC spectra were included for modelling. (b) Example of preprocessed cholesterol cholesterol 30% spectra (solid line). Fit is the linear combination of principal component spectra (dashed line). (c) Example of pure water preprocessed spectrum (solid line). Fit is the linear combination of principal component spectra (dashed line). Residuals of fit within (b) and (c) are shown in grey. Adapted from Fleming CP et al. Biomed Opt Express 2013; 4: 1269-84.

Figure 3 shows the normalized confusion matrices for the three models for classifying the cholesterol mixture phantoms belonging to the first set of phantoms. An ideal model will have ones (white) along the diagonal. Attenuation analysis alone had an overall accuracy of 38.98% and a lower power to discriminate for compositions with cholesterol. Spectral

analysis had a 60.45% overall accuracy and improved prediction rate for compositions with cholesterol. The combination of attenuation and spectral analysis improved the classification to 72.6%. Importantly, the magnitude of the attenuation had poor correlation coefficients with spectral fitting coefficients, indicating that this additional spectral analysis adds information.

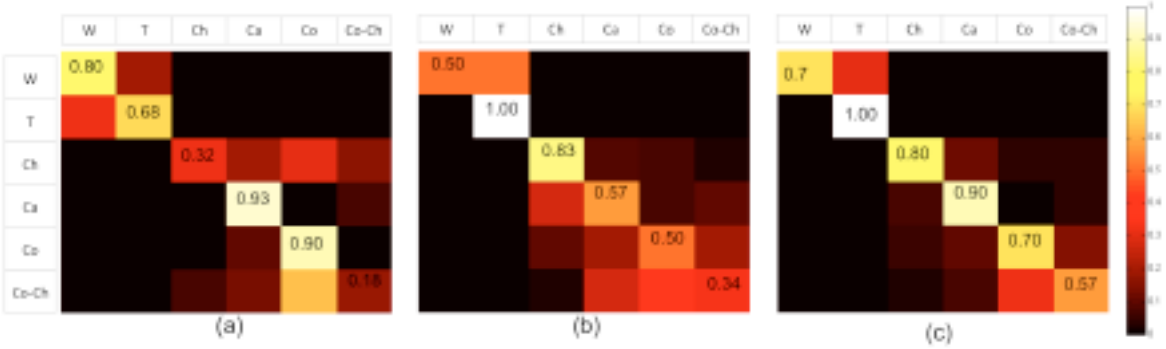

Figure 3 showing normalized confusion matrices explaining the results of the discriminant analysis model. (a) Model incorporating attenuation coefficient. (b) Model incorporating spectral fitting coefficients. (c) Model incorporating both attenuation coefficient and spectral fitting parameters. The classification accuracy improves significantly by combining information from both the magnitude of the attenuation coefficient and the spectral shape. W: water; T: trioleate; Ch: cholesterol; Ca: calcium; Co: collagen; Co-Ch: collagen and cholesterol. Adapted from Fleming CP et al. Biomed Opt Express 2013; 4: 1269-84.

To further evaluate this algorithm, the second set of phantoms was designed to give the appearance of a lipid rich plaque within OFDI images. Artificial plaques were created by injecting of fat emulsions into the tunica media layer of fresh normal swine aorta. Imaging occurred directly after making the plaque phantoms. Aortic phantom samples were fixed in 10% neutral buffered formalin. Frozen cross sectional sections (10μm thickness) were stained with Oil Red O (ORO) and Hemotoxylin and Eosin (H&E). Slides were digitized using a NanoZoomer 2.0-HT slide scanner (Hamamatsu) at 20X. All imaging was conducted with a custom built OFDI system, which had a 1300 nm center wavelength, 100 nm bandwith, and 52 kHz axial line rate. Figures 4 and 5 depict example images of the phantom plaques. Figure 4 is of a normal section of swine aorta, without injection of the fat emulsion.

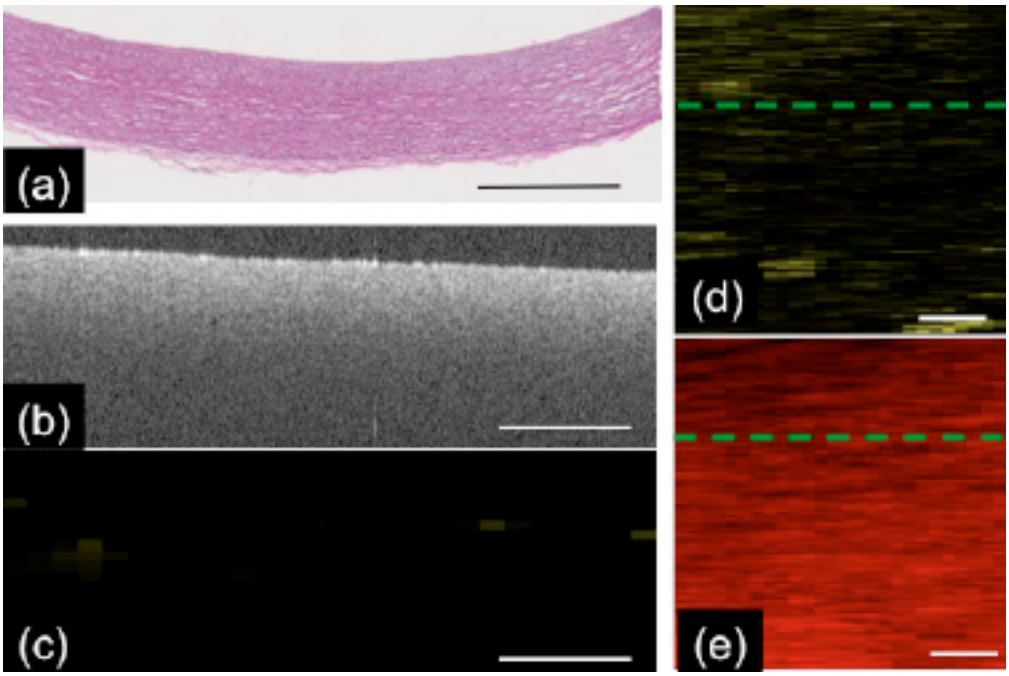

Figure 4. (a) H&E of normal swine aorta. (b) Corresponding OFDI image. (c) Probability of cholesterol image showing no detected cholesterol using spectral analysis. (d) Depth resolved integration of cholesterol probability. (e) Depth resolved integration of collagen probability, showing a relatively uniform amount of collagen and apparent fiber structure. Scale bars corresponding to 1 mm. Adapted from Fleming CP et al. Biomed Opt Express 2013; 4:1269-84.

An example of the lipid plaque model is shown in Figure 5. Regions with the fat emulsion show a signal poor region with diffuse boundaries, consistent with the published qualitative description of lipid plaques.

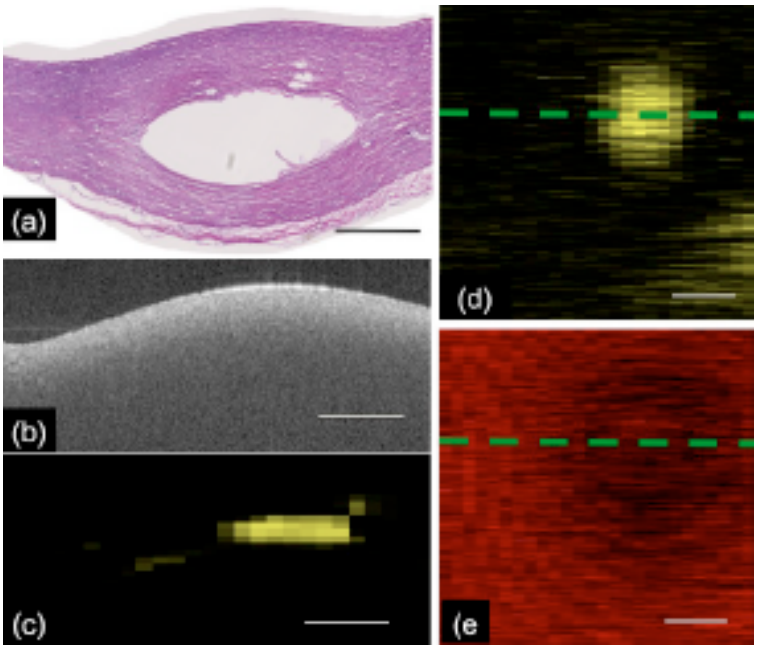

Figure 5. (b) H&E stain showing a void created by the injection of a fat emulsion. (a) Corresponding OFDI image of phantom lipid plaque. (c) Probability of cholesterol image, showing increased probability at center of plaque. (d) Depth resolved integration of cholesterol probability, with increased lipid probability at the center of plaque. (e) Depth resolved integration of collagen probability, with decrease collagen probability within the center of plaque. Scale bars corresponding to 1 mm. Adapted from Fleming CP et al. Biomed Opt Express 2013; 4:1269-84.

This algorithm was also tested using *ex-vivo* data (5 hearts). Then, the next step was to validate this algorithm on OFDI pullbacks from the Natural History of Vulnerable Plaque study. The goal was to develop an algorithm providing a color coded OCT image that could make it easier for non-expert OCT readers to delineate fibroatheromas. The design of the study was the following: 2 beginners (young interventional cardiologists) of Bordeaux University had to read 500 randomized OFDI frames with and without lipid of plaques selected by Edouard Gerbaud. Dr. Guillermo J. Tearney had to read the same data set and was the expert. The data set will ideally be read 2 times for intra-observer variability assessment. The responses requested to the readers were: presence or absence of lipid and in which quadrant 1= 0 to 3 hours, 2= 3 to 6 hours, 3= 6 to 9 hours and 4= 9 to 12 hours. Before to start this study, a training set including 50 OFDI unselected frames was performed

and analyzed using the algorithm based off the the spectral fitting coefficients and the attenuation. The model was based on four input parameters and five output classes (lipid, adipose, blood, calcium, fibrous). This algorithm was able to determine the presence of lipid as a binary or probability of lipid, range of 0-1. An expert (Dr. Guillermo J. Tearney) analysed the same training set. Plaques were manually segmented and different colors were assigned as follows : lipidic plaque : yellow, calcific plaque : blue, fibrotic plaques : purple, blood : red and adipose tissue : orange. The preliminary unpublished results were interesting but not straightforward. A multivariate power analysis between the algorithm results and the expert (GJT) analysis on this training set revealed that 30% of lipid cases were misclassified as adipose tissue, 27% cases of calcific plaques were misclassified as lipidic plaques, and that 17% of fibrotic plaques misclassified as lipidic plaques.

	Lipid	Adipose	Blood	Calcium	Fibrous
Lipid	0.4010	0.3029	0.0948	0.1303	0.0711
Adipose	0.0833	0.7917	0.0417	0.0417	0.0417
Blood	0.0769	0.2308	0.5385	0	0.1538
Calcium	0.2774	0.2240	0.1406	0.2249	0.1331
Fibrous	0.1705	0.3101	0.1395	0.1473	0.2326

Table 1 showing normalized confusion matrices explaining the results of the discriminant analysis model on the training data set. Unpublished data; courtesy of Christine P. Hendon.

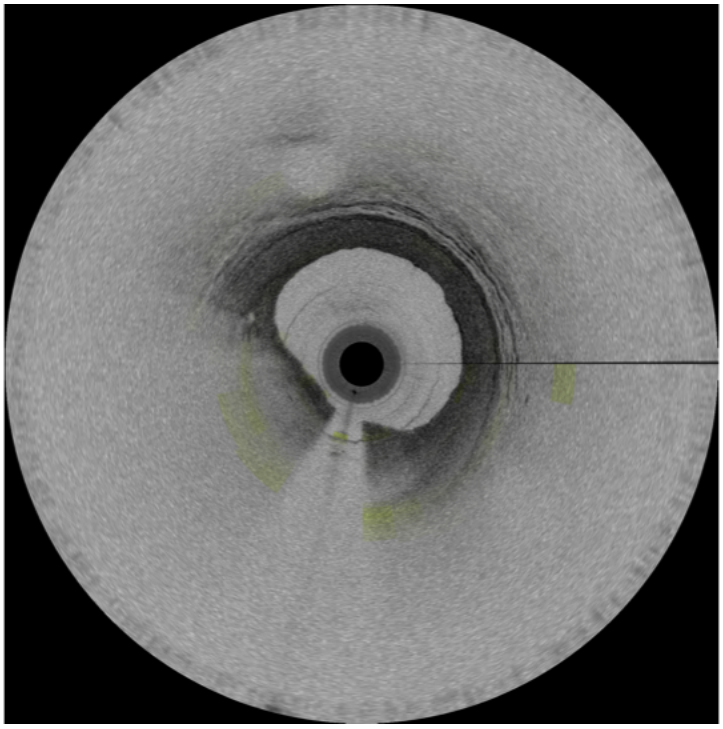

Example of the algorithm process of an OFDI frame including a large lipidic plaque (from 5 to 10 o'clock). Lipid detected by the classification model appears in yellow. The algorithm seems to be adequate. Unpublished images: courtesy of Christine P. Hendon.

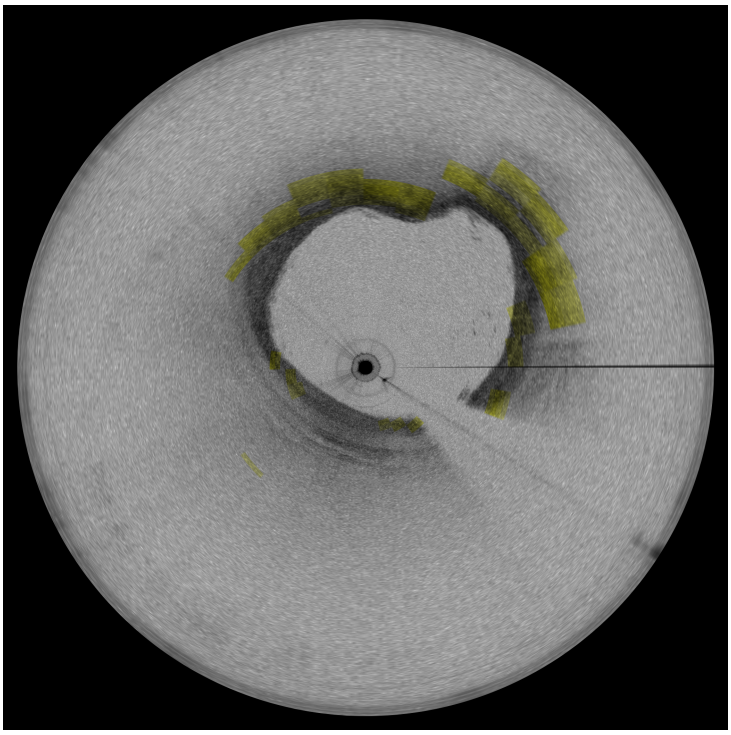

Example of the algorithm process of an OFDI frame including a large lipidic plaque (from 9 to 3 o'clock). Lipid detected by the classification model appears in yellow. The algorithm seems to be adequate. Unpublished images: courtesy of Christine P. Hendon.

Example of the algorithm process of an OFDI frame including a large calcific plaque (from 7 to 11 o'clock). Lipid detected by the classification model appears in yellow. The algorithm seems to be inadequate. Unpublished images: courtesy of Christine P. Hendon.

Some explanations of these results exist. Indeed, the histological validation of this algorithm need to be completed. Thus, the algorithm was not validated and tested using a large panel of ex-vivo data (i.e. human autopsies) including a sufficient number of lipidic plaques. Furthermore, the ex vivo data were collected with one MGH OFDI prototype, having a different light source and a better spatial resolution than a clinical OFDI catheter.

3.3.2 Optical coherence tomography – near infrared spectroscopy catheter for iintravascular imaging

Near-infrared spectroscopy (NIRS) has been developped as a standalone imaging modality and was able to detect lipid pool through and deep within the artery wall. Recently, NIRS has been combined with intravascular ultrasound (IVUS) to provide co-registered structural and chemical information. This combination is particularly advantageous, since IVUS can measure plaque structure, while NIRS accurately and reproducibly can determine the presence of lipid-rich plaques. NIRS system has been validated using histology in coronary

artery specimens. This technology enables to quantify the amount of lipid present, defining a chemogram image and calculating the lipid core burden index (LCBI) i.e. the fraction of pixels indicating lipid within a region multiplied by 1000 [23]. Currently, commercially available NIRS-IVUS combines extended bandwidth 50 MHz rotational IVUS with NIRS on a single 3.2 Fr monorail catheter. Near infrared spectroscopy-intravascular ultrasound has been used in a number of trials to assess the effect of statins on plaque burden and composition. Near infrared spectroscopy-intravascular ultrasound studies have also shown that the culprit lesions in patients presenting with acute STEMI have specific morphological characteristics (i.e. an increased lipid component and plaque burden), suggesting that a high-risk lipid plaque signature is associated with acute cardiac events (Figure 2). Each 10-mm culprit and non-culprit segment was scanned for the maximum LCBI in any 4-mm region (maxLCBI4mm), as previously described. Madder RD et al. demonstrated that the cut-off value of a maxLCBI4mm >400, as detected by NIRS, is a signature of plaques causing STEMI [24].

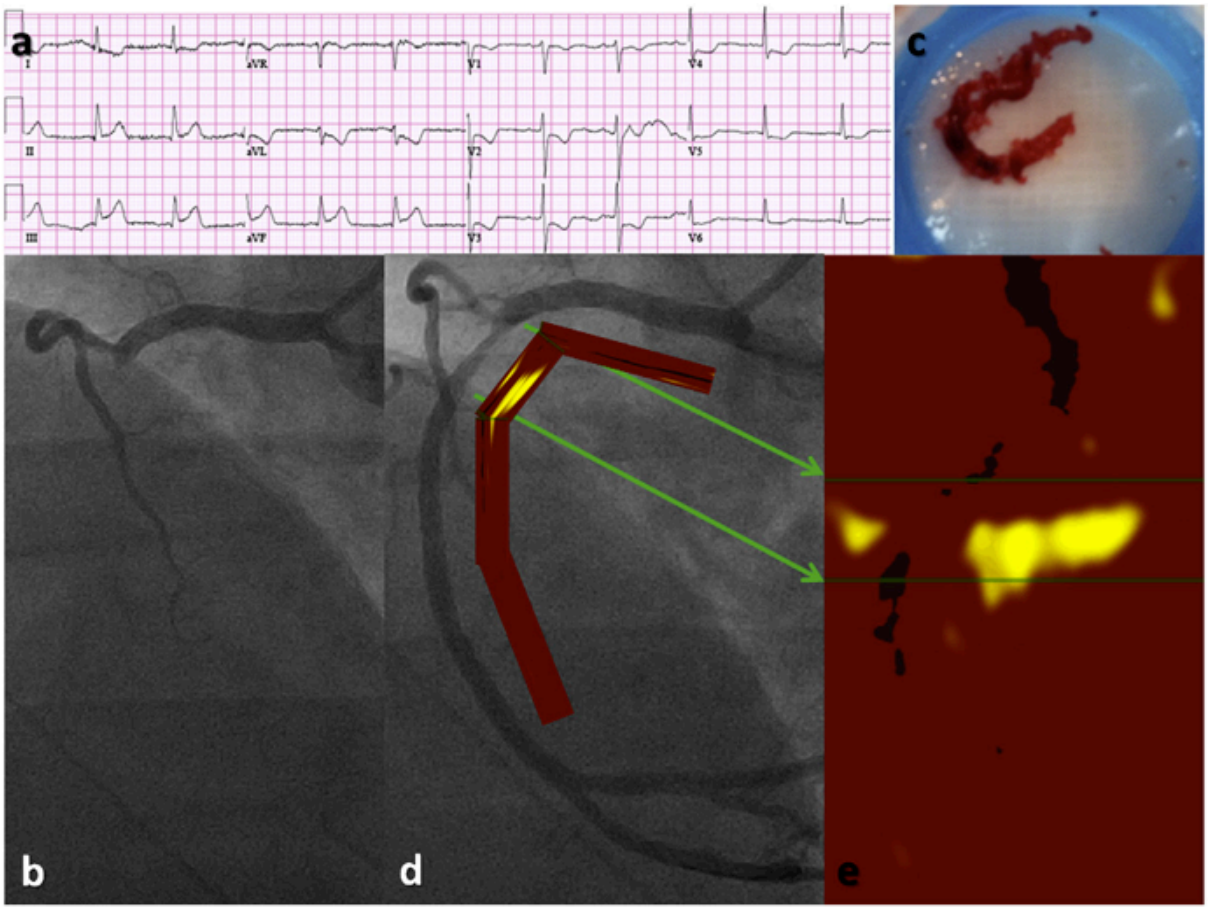

Figure depicting a patient 56 years-old presenting with acute chest pain and inferior-posterior injury (a) who was referred for primary PCI. Angiography of the right coronary artery revealed complete occlusion (b). Aspiration yielded a thrombus characteristic of STEMI (c) and resulted in TIMI flow grade 3 (d). NIRS performed after TIMI flow grade 3 was established revealed a prominent, nearly circumferential large lipid core concentrated at the culprit site (e). Adapted from Madder RD et al. J Am Coll Cardiol Intv 2013; 6:838-846.

Some early results suggest also the ability of NIRS-IVUS to identify plaque characteristics associated with future events and two major trials are underway (Prospect II, NCT02171065; and the Lipid Rich Plaque Study, NCT02033694) to more comprehensively and rigorously prove this hypothesis. Limitations of NIRS-IVUS include the inadequate spatial resolution of IVUS for finer measurements such as the neointimal coverage of stent struts or the cap thickness, the loss of the IVUS imaging signal behind calcific tissue or stent struts, occasional lumen border definition issues in the presence of thrombus or high blood speckle. Near infrared spectroscopy is limited by not giving explicit depth information of the lipid core plaque, and thus superficial lipid cannot be distinguished from deep lipid in the same arc using the NIRS information alone. These limitations may be resolved by the development of a dual-modality OCT-NIRS catheter. A OCT-NIRS system using a wavelength-swept light source for both OCT and NIRS modalities has been created in Dr. Tearney's lab [25].

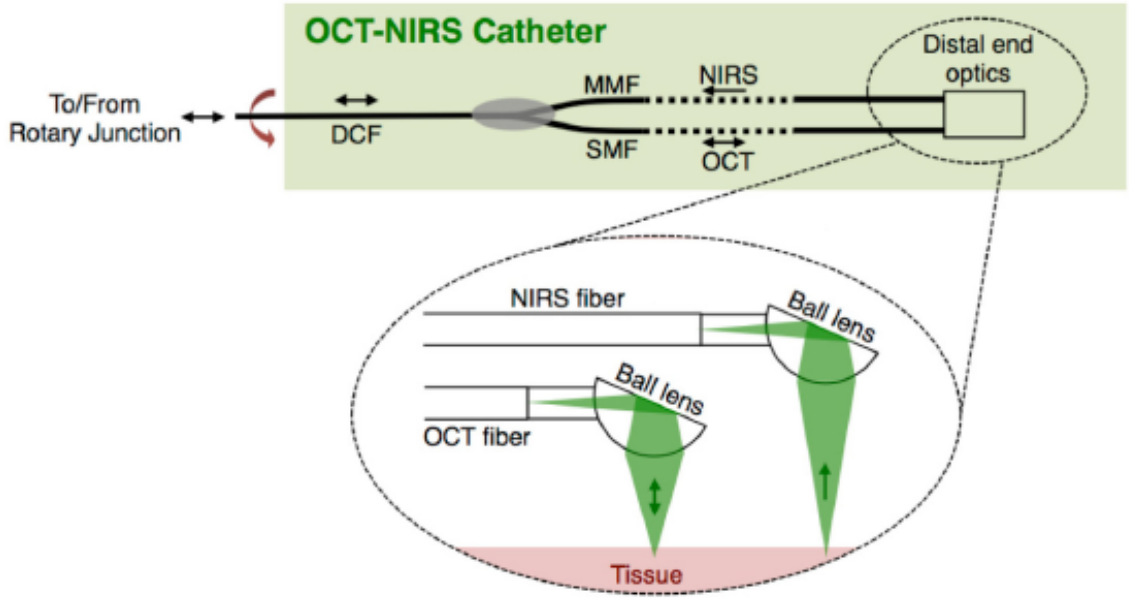

Schematic for OCT-NIRS Catheter. Inside the catheter, a single-mode fiber (SMF) delivered and collected OCT light to/from tissue and a multi-mode fiber (MMF) collected NIRS light. The two fibers were combined into a double-clad fiber (DCF) using a commercial power combiner such that the OCT light transceived through the core of the SMF and DCF, while NIRS light coupled to the cladding of the DCF. At the distal end (insets), the SM and MM fibers were terminated by two angle-cleaved ball lenses for efficient delivery/collection of OCT and NIRS light to/from tissue. In order to spin the catheter for cross-sectional dual modality imaging, all optical fibers, optical power combiner, and distal optics were housed in a 2.4-Fr driveshaft and stainless steel tubing. Adapted from Fard AM et al. Opt Express 2013; 21: 30849-58.

Fard AM et al. already reported ex-vivo data [25].

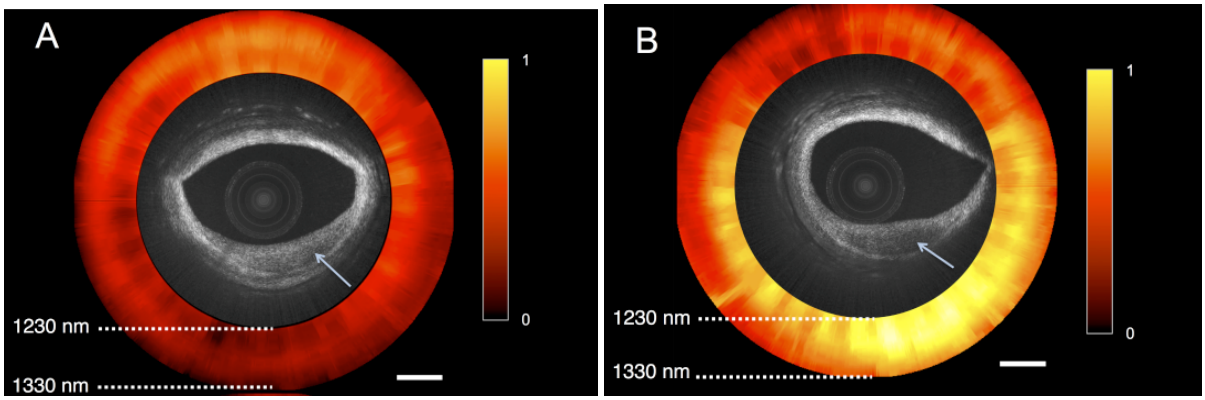

OCT-NIRS images of human cadaver plaques that appear similar by optical coherence tomography. The optical coherence tomography microstructural image is surrounded by the near infrared spectroscopy absorption spectrum at each angle of rotation of the catheter, where yellow indicates high absorption. The plaque in (A) does not exhibit significant near infrared spectroscopy absorption, whereas the lesion in (B) does. These near infrared spectroscopy datasets indicate that the plaque in (B) is fibrocalcific, whereas in (C) is a lipid-rich plaque. Adapted from Fard AM et al. Opt Express 2013; 21: 30849-58.

First-in-human OFDI-NIRS imaging procedures are anticipated in the near future (2016-2017). Several directions include development of a broad bandwidth cholesterol to cholesterol esters ratio that is known to be associated with high-risk coronary lesions.

References

1. Virmani R, Kolodgie FD, Burke AP, Farb A, Schwartz SM. Lessons from sudden coronary death: a comprehensive morphological classification scheme for atherosclerotic lesions. Arterioscler Thromb Vasc Biol 2000; 20:1262–75.
2. Naghavi M, Libby P, Falk E, Casscells SW, Litvosky S, Rumberger S, et al. From vulnerable plaque to vulnerable patient: a call for new definitions and risk assessment strategies : part I. Circulation 2003;108:1664-1672.
3. Virmani R, Burke AP, Farb A, Kolodgie FD. Pathology of the vulnerable plaque. J Am Coll Cardiol 2006; 47:C13–8.
4. Tian J, Ren X, Vergallo R, Xing L, Yu H, Jia H, et al. Distinct morphologic features of ruptured culprit plaque for acute coronary events compared to those with silent rupture and thin-cap fibroatheroma. J Am Coll Cardiol 2014; 63:2209-16.
5. Jia H, Abtahian F, Aguire AD, Lee S, Chia S, Lowe H, et al. *In vivo* diagnosis of plaque erosion and calcified nodules in patients with acute coronary syndrome by intravascular optical coherence tomography. J Am Coll Cardiol 2013; 63:1748-58.
6. Kolodgie FD, Gold HK, Burke AP, Fowler DR, Kruth HS, Weber DK, et al. Intraplaque hemorrhage and progression of coronary atheroma. N Eng J Med 2003; 349:2316-2325.
7. Taruya A, Tanaka A, Nishiguchi T, Matsuo Y, Ozaki Y, Kashiwaghi M, et al. Vasa vasorum restructuring in human atherosclerotic plaque vulnerability. A clinical optical coherence tomography study. J Am Coll Cardiol 2015; 65:2469-77.
8. Lendon CL, Davies MJ, Born GV, Richardson PD. Atherosclerotic plaque caps are locally weakened when macrophages density is increased. Atherosclerosis 1991;87: 87–90.
9. Moreno PR, Falk E, Palacios IF, Newell JB, Fuster V, Fallon JT. Macrophage infiltration in acute coronary syndromes: implications for plaque rupture. Circulation 1994; 90:775–778.
10. Galis ZS, Sukhova GK, Kranzhöfer R, Clark S, Libby P. Macrophage foam cells from experimental atheroma constitutively produce matrix-degrading proteinases. Proc Natl Acad Sci U S A 1995; 92:402–406.
11. Lee RT, Schoen FJ, Loree HM, Lark MW, Libby P. Circumferential stress and matrix

metalloproteinase 1 in human coronary atherosclerosis: implications for plaque rupture. Arterioscler Thromb Vasc Biol 1996; 16:1070–1073.

12. Davies MJ, Richardson PD, Woolf N, Katz DR, Mann J, et al. Risk of thrombosis in human atherosclerotic plaques: role of extracellular lipid, macrophage, and smooth muscle cell content. Br Heart J. 1993; 69:377–381.
13. Tearney GJ, Yabushita H, Houser SL, Aretz HT, Jang IK, Schlendorf KH, et al. Quantification of macrophage content in atherosclerotic plaques by optical coherence tomography. Circulation 2003; 107:113-119.
14. Phipps JE, Vela D, Hoyt T, Halaney DL, Mancuso JJ, Buja ML, et al. Macrophages and intravascular OCT bright spots: a quantitative study. J Am Coll Cardiol Img 2015; 8:63-72.
15. Tearney GJ, Regar E, Akasaka T, Adriaenssens T, Barlis P, Bezerra HG, et al. International Working Group for Intravascular Optical Coherence Tomography (IWG-IVOCT). Consensus standards for acquisition, measurement, and reporting of intravascular optical coherence tomography studies. A report from the international working group for intravascular optical coherence tomography standardization and validation. J Am Coll Cardiol 2012; 59:1058-72.
16. Caplan JD, Waxman S, Nesto RW, Muller JE. Near-Infrared Spectroscopy for the Detection of Vulnerable Coronary Artery Plaques. J Am Coll Cardiol 2006; 47:C92-6.
17. Levitz D, Thrane L, Frosz MH, Andersen PE, Andersen CB, Andresson-Engels S, et al. Determination of optical scattering properties of highly -scattering media in optical coherence tomography images. Optics Express 2004; 12:249-259.
18. van der Meer FJ, Faber DJ, Baraznji Sassoon DM, Aalders MC, Pasterkamp G, van Leuween TG, et al. Localized Measurement of Optical Attenuation Coefficients of Atherosclerotic Plaque Consitutents by Quantitative Optical Coherence Tomography. IEEE Transactions on Medical Imaging 2005; 24:1369-75.
19. van der Meer FJ, Faber DJ, Baraznji Sassoon DM, Aalders MC, Pasterkamp G, van Leuween TG, et al. Quantitative optical coherence tomography of arterial wall components. Lasers in Medical Science 2005; 20:45-51.

20. Xu C, Schmitt J, Carlier S, Virmani R. Characterization of atherosclerosis plaques by measuring both backscattering and attenuation coefficients in optical coherence tomography. Journal of Biomedical Optics 2008; 13: 1-8.
21. van Soest, G, Regar E, Koljenovic S, van Leenders GJLH, Gonzalo N, van Noorden S, et al. Atherosclerotic tissue characterization in vivo by optical coherence tomography attenuation imaging. Journal of Biomedical Optics 2010; 15:011105-9.
22. Fleming CP, Eckert J, Halpern EF, Gardecki JA, Tearney GJ. Depth resolved detection of lipid using spectroscopic optical coherence tomography. Biomed Opt Express 2013; 4: 1269-84.
23. Gardner CM, Tan H, Hull EL, Lisauskas JB, Sum ST, Meese TM, et al. Detection of lipid core coronary plaques in autopsy specimens with a novel catheter-based near-infrared spectroscopy system. J Am Coll Cardiol Img 2009; 1:638-648.
24. Madder RD, Goldstein JA, Madden SP, Puri R, Wolksi K, Hendricks M, et al. Detection by near-infrared spectroscopy of large lipid core plaques at culprit sites in patients with acute ST-segment elevation myocardial infarction. J Am Coll Cardiol Intv 2013; 6:838-846.
25. Fard AM, Vacas-Jacques P, Hamidi E, Wang H, Carruth RW, Gardecki JA, Tearney GJ. Optical coherence tomography – near infrared spectroscopy system and catheter for intravascular imaging. Opt Express 2013; 21: 30849-58.

3.4 Necrotic cores detected by near-infrared autofluorescence (NIRAF)

3.4.1 Ex-vivo studies

Optical frequency domain imaging (OFDI) has been documented to be capable of identifying extracellular lipid. However, this imaging modality is not established for differentiating necrotic core from non necrotic lipid-rich lesions. In OFDI, lipid manifests as a signal poor region that has diffuse borders with respect to the surrounding tissues and a rapid signal decay in depth [1]. These optical properties are valuable for both necrotic and non necrotic lipids. Furthermore, high attenuation in plaque may be induced by either components such as macrophages [2] and blood or artifacts such as tangential signal dropout [3,4]. One main objective of research in this topic consists to add complementary information to OFDI to bring the physicians closer to a single-catheter solution for comprehensive evaluation of coronary pathology *in vivo*. Additional molecular imaging of inflammatory pathways like oxidative stress in atherosclerotic lesions could therefore be of considerable clinical importance, allowing better identification and risk stratification of high-risk plaques [5].

One such additive signal may be near infrared autofluorescence (NIRAF), which can be measured by illuminating atherosclerotic lesions in the NIR region of 600-850 nm and detecting the associated red-shifted fluorescence light. NIRAF has been found to be elevated in lipid-containing lesions; the origin of this signal has been hypothesized to be associated with red blood cell remnants [6], ceroid/lipofuscin [7], and carotenoids [8]. Wang H et al. have recently conducted experiments in cadaver plaques *ex vivo*. First, they used a double clad fiber ball lens probe and a bench top setup to acquire *en face* NIRAF images of aortic plaques *ex vivo* (n=20). They identified optimal NIRAF excitation (633 nm) and detection (675-950 nm). They observed that the mean NIRAF signals of necrotic core were significantly higher than the non-necrotic lesions (pathological intimal thickening, calcified plaque and intimal hyperplasia) ($p<0.001$). In the same way, they built an OFDI-NIRAF catheter and investigated *ex-vivo* 15 coronary arteries from 5 explant human hearts. The post-processing of OFDI-NIRAF data sets included the following steps: background removal, distance calibration and NIRAF signal normalization. After imaging of these 15 coronary arteries, they analysed NIRAF intensity from 37 distinct artery wall regions: coronary necrotic core/ruptured plaques (n=3), pathological intimal thickening plaques (n=2), calcified plaques (n=12), and regions of intimal hyperplasia

(n=20). They observed significant differences in normalized NIRAF intensities between all different types of plaques ($p<0.0005$).

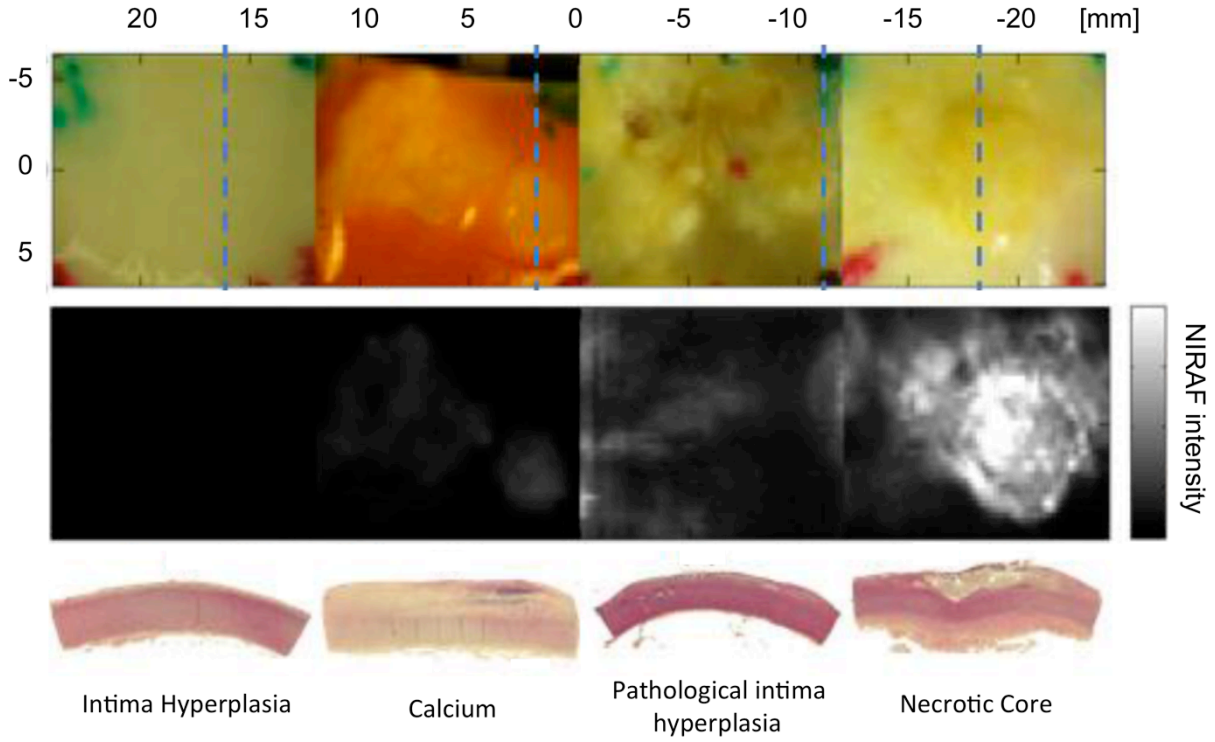

Figure showing different types of plaques and the corresponding NIRAF intensities.
NIRAF signal is elevated in necrotic cores. NIRAF signal is found in areas of high inflammatory activity. Adapted from Wang H et al. Biomed Opt Express 2015; 6:1363–1375.

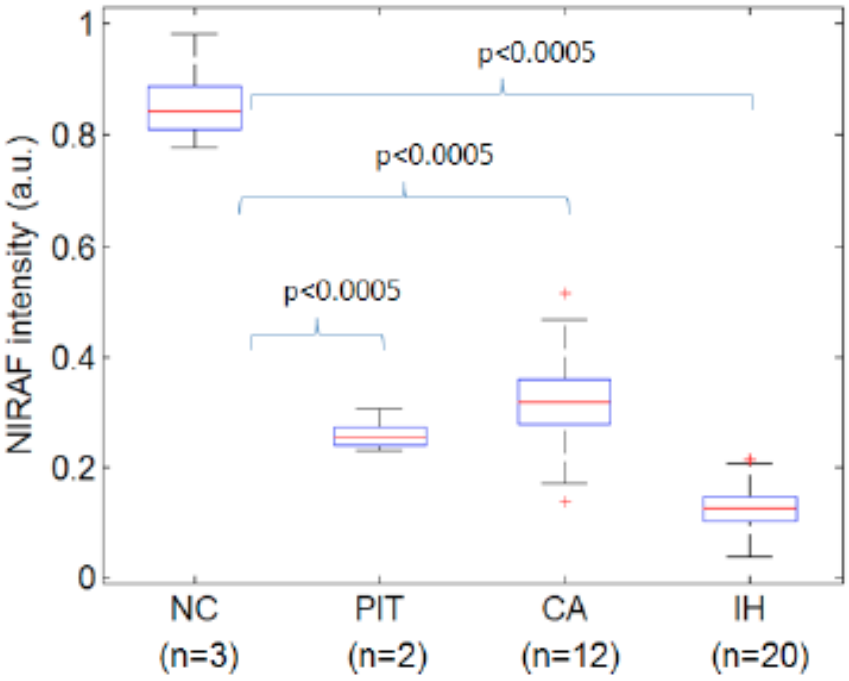

Comparison of NIRAF intensity for different types of coronary lesions. IH: intimal hyperplasia, CA: calcified plaque, PIT: pathological intimal thickening plaque, NC: necrotic core plaque. The NIRAF intensities from IH, CA, PIT and NC were statistically significantly different according to one-way ANOVA ($p<0.0005$). Adapted from Wang H et al. Biomed Opt Express 2015; 6:1363–1375.

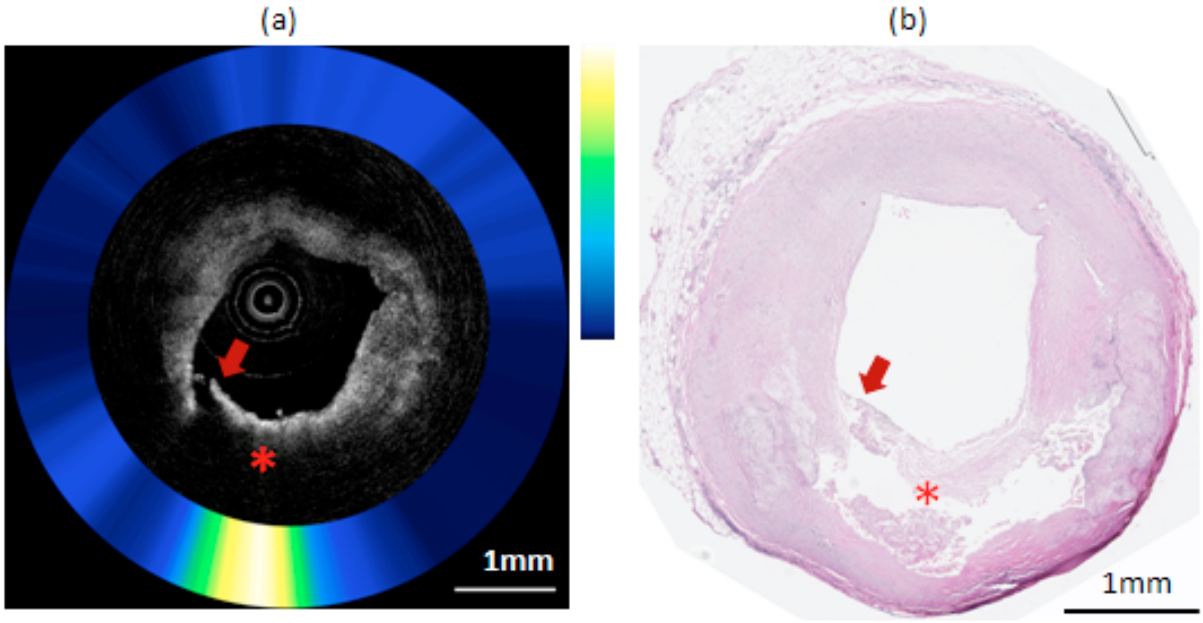

OFDI-NIRAF image of a ruptured cadaver plaque acquired with the OFDI-NIRAF catheter (left) adjacent to corresponding histology (right). (a) The OFDI image indicates the presence of a plaque rupture (arrow) and area of high attenuation suggestive of a high lipid-pool or necrotic core (star). The NIRAF signal is strong (yellow) at the necrotic core location. (b) H&E stained slide confirming that this plaque is a ruptured thin-cap fibroatheroma. The scale bars for both (a) and (b) represent 1 mm. Adapted from Wang H et al. Biomed Opt Express 2015; 6:1363–1375.

3.4.2 First-in-human dual-modality OCT and autofluorescence Imaging of Coronary Artery Disease

Following all these results, Dr. Tearney has received FDA approval to conduct NIRAF/OCT imaging studies in humans. Dr. E Gerbaud joined Dr. Tearney's team to participate to the first in-human studies of this technology.

References

1. Yabushita H, Bouma BE, Houser SL, Aretz HT, Jang IK, Schlendorf KH, et al. Characterization of human atherosclerosis by optical coherence tomography. Circulation 2002; 106:1640-45.
2. Tearney GJ, Yabushita H, Houser SL, Aretz HT, Jang IK, Schlendorf KH, et al. Quantification of macrophage content in atherosclerotic plaques by optical coherence tomography. Circulation 2003; 107:113-119.
3. van Soest G, Regar E, Goderie T, Gonzalo N, Koljenovic S, van Leenders GL, et al. Pitfalls in plaque characterization by OCT: image artifacts in native coronary arteries. J Am Coll Cardiol Img 2011; 4:810-813
4. Motreff P, Levesque S, Souteyrand G, Sarry L, Ouchchane L, Citron B, et al. High-resolution coronary imaging by optical coherence tomography: feasibility, pitfalls and artefact analysis. Arch Cardiovasc Dis 2010; 103:215-226.
5. Jaffer FA, Libby P, Weissleder R. Molecular and cellular imaging of atherosclerosis: emerging applications. J Am Coll Cardiol. 2006; 47:1328-1338.
6. Kolodgie FD, Gold HK, Burke AP, Fowler DR, Kruth HS, Weber DK, et al. Intraplaque hemorrhage and progression of coronary atheroma. N Eng J Med 2003; 349:2316-2325.
7. Papazoglou TG. Malignancies and atherosclerotic plaque diagnosis--is laser induced fluorescence spectroscopy the ultimate solution? Journal of Photochemistry and Photobiology 1995; 28:3-11.
8. Uchida, Y., S. Kawai, R. Kanamaru, Y. Sugiyama, T. Tomaru, Y. Maezawa, and N. Kameda, *Detection of vulnerable coronary plaques by color fluorescent angioscopy.* J Am Coll Cardiol Img 2010; 3 :398-408**.**
9. Wang H, Gardecki JA, Ughi GJ, Vacas Jacques P, Hamidi E, Tearney GJ. *Ex-vivo* catheter-based imaging of coronary atherosclerosis using multimodality OCT and NIRAF excited at 633 nm. Biomedical optics express 2015;6:1363-75.

Clinical Characterization of Coronary Atherosclerosis With Dual-Modality OCT and Near-Infrared Autofluorescence Imaging

Giovanni J. Ughi, PhD,[1] Hao Wang, PhD,[1] Edouard Gerbaud, MD,[1] Joseph A. Gardecki, PhD,[1] Ali M. Fard, PhD,[1] Ehsan Hamidi, PhD,[1] Paulino Vacas-Jacques, PhD,[1] Mireille Rosenberg, PhD,[1] †Farouc A. Jaffer, MD, PhD, FACC,[1,2] and †Guillermo J. Tearney, MD, PhD, FACC, FCAP*[,1,3,4]

[1]Wellman Center for Photomedicine, Harvard Medical School and Massachusetts General Hospital, Boston, MA, USA
[2]Cardiovascular Research Center and Cardiology Division, Harvard Medical School and Massachusetts General Hospital, Boston, MA, USA
[3]Department of Pathology, Massachusetts General Hospital and Harvard Medical School, Boston, MA
[4]Harvard-MIT Health Sciences and Technology, Boston, MA
†Dr. Jaffer and Dr. Tearney share senior authorship.

JACC Cardiovascular Imaging 2016; Mar 3. pii: S1936-878X(16)00038-3. doi: 10.1016/j.jcmg.2015.11.020.

***Address for Correspondence**:
Guillermo J. Tearney, MD, PhD, FACC, FCAP or Farouc Jaffer, MD, PhD, FACC

Guillermo Tearney, MD, PhD, FACC, FCAP
Massachusetts General Hospital
Wellman Center for Photomedicine
40 Blossom Street, BHX-604A
Boston, Massachusetts 02114.
Tel: (617) 724-2979; Fax: (617) 726-4103.
Email: gtearney@partners.org

Farouc Jaffer, MD, PhD, FACC
Massachusetts General Hospital
Cardiovascular Research Center
Simches Research Building, Room 3206
Boston, Massachusetts 02114
Tel: (617) 724-9353; Fax: (617) 860-3180
Email: fjaffer@mgh.harvard.edu

Word count: 4,494 words (including references and figure legends)
Brief title: First-in-human coronary OCT-NIRAF imaging
Keywords: optical coherence tomography; near-infrared fluorescence; multi-modality imaging; first-in-human

Author email addresses:
Giovanni J. Ughi: giovanni.ughi@gmail.com
Hao Wang: hwang21mgh@outlook.com
Edouard Gerbaud: edouard.gerbaud@chu-bordeaux.fr
Joseph A. Gardecki: gardecki.joseph@mgh.harvard.edu
Ali M. Fard: mfard.ali@mgh.harvard.edu
Ehsan Hamidi: hamidiehsan@gmail.com
Paulino Jacques-Vacas: pvjacques@gmail.com
Mireille Rosenberg: mrosenberg@mgh.harvard.edu
Farouc A. Jaffer: fjaffer@mgh.harvard.edu
Guillermo J. Tearney**:** gtearney@partners.org

Disclosures: Massachusetts General Hospital has a patent licensing arrangement with Terumo and Canon Corporations. Dr. Tearney (Terumo, Canon), Dr. Gardecki (Canon) and Dr. Jaffer (Canon) have the right to receive royalties as part of this licensing arrangement. Dr. Tearney also receives royalties from MIT. Dr. Tearney receives sponsored research from Canon and Infraredx. Dr. Tearney receives catheter components from Terumo. Dr. Jaffer receives sponsored research from Merck, Kowa, and Siemens, and nonfinancial support from Boston Scientific.

STRUCTURED ABSTRACT

OBJECTIVES We present the first clinical imaging of human coronary arteries in vivo using a multimodality OCT and near-infrared autofluorescence (NIRAF) intravascular imaging system and catheter.

BACKGROUND Although intravascular OCT is capable of providing microstructural images of coronary atherosclerotic lesions, it is limited in its capability to ascertain compositional/molecular features of plaque, including the definitive presence of a necrotic core. A recent study in cadaver coronary plaque has shown that endogenous NIRAF is elevated in necrotic core lesions. The combination of these two technologies in one device may therefore provide synergistic data to aid in the diagnosis of coronary pathology *in vivo*.

METHODS We developed a dual-modality intravascular imaging system and 2.6-F catheter that can simultaneously acquire OCT and NIRAF data from the same location on the artery wall. This technology was used to obtain volumetric OCT-NIRAF images from 12 patients with coronary artery disease undergoing PCI. Images were acquired during a brief, non-occlusive 3-4 ml/sec contrast purge at a speed of 100 frames per second and a pullback rate of 20 or 40 mm/sec. OCT-NIRAF data were analyzed to determine the distribution of the NIRAF signal with respect to OCT-delineated plaque morphological features.

RESULTS High quality intracoronary OCT and NIRAF image data (>50 mm pullback length) were successfully acquired without complication in all patients (17 coronary arteries). The maximum NIRAF signal intensity of each plaque was compared to OCT-defined type, showing a statistically significant difference between plaque types (one-way ANOVA, $p<0.0001$). Interestingly, coronary arterial NIRAF intensity was elevated only focally in plaques with a high-risk morphologic phenotype ($p<0.05$), including OCT fibroatheroma, plaque rupture, and fibroatheroma associated with in-stent restenosis.

CONCLUSIONS This OCT-NIRAF study demonstrates that dual-modality microstructural and fluorescence intracoronary imaging can be safely and effectively conducted in human patients. Our findings show that NIRAF is associated with a high-risk morphologic plaque phenotype. The focal distribution of NIRAF in these lesions

furthermore suggests that this endogenous imaging biomarker may provide complementary information to that obtained by structural imaging alone.

CONDENSED ABSTRACT

We developed a dual-modality OCT and near-infrared autofluorescence (NIRAF) system and 2.6-F catheter for coronary imaging. In a first-in-human-study, we enrolled 12 patients with CAD undergoing PCI, and demonstrated that intracoronary OCT-NIRAF imaging can be safely and effectively conducted in human patients. We found that NIRAF is elevated focally in atheromas harboring high-risk morphologic phenotypes, including OCT-fibroatheroma, plaque rupture, and fibroatheroma associated with in-stent restenosis. These results suggest that NIRAF is only associated with high-risk morphologic plaque phenotypes but may also provide complementary information to that obtained by structural imaging alone.

ABBREVIATION LIST

DCF = double-clad fiber

NIRF = near-infrared fluorescence

NIRAF = near-infrared autofluorescence

NIRS = near-infrared spectroscopy

NSD = normalized standard deviation

NURD = non uniform rotational distortion

OCT = optical coherence tomography

PCI = percutaneous coronary intervention

TCFA = thin-cap fibroatheromas

ThCFA = thick-cap fibroatheroma

INTRODUCTION

Intravascular optical coherence tomography (OCT) is a high-resolution imaging technique that is increasingly being utilized in interventional cardiology for the investigation and management of coronary artery disease (CAD) (1,2). OCT enables the visualization of artery wall microstructure, including morphologic features related to coronary events such as lipid-containing regions, macrophage accumulations, thin-cap fibroatheromas (TCFA), erosion and rupture of coronary plaques, and presence of thrombi and calcified nodules (1,2). Owing to its capability to enable a clear view of the detailed arterial morphology and implanted arterial stents, OCT has also been used to assess the response of the artery wall following percutaneous coronary intervention (PCI) (1,2).

Even though OCT provides an unprecedented level of morphologic detail, it does have limitations that constrain its diagnostic capabilities. Key plaque features such as lipid, for example, manifest as low OCT signal. The use of negative contrast features can confound diagnosis, as signal loss may arise from a variety of different sources such as macrophage shadowing, intraluminal debris, and image artifacts (3,4). Furthermore, the capability of OCT to differentiate non-necrotic intra- and extracellular lipid accumulations from necrotic core lipid has never been shown and therefore remains an unresolved question in the field (2,4). This ambiguity is problematic, as many studies have shown that a definitive diagnosis of necrosis is needed to distinguish the most advanced, progression-prone lesions (5). In addition, microstructure alone does not provide a complete understanding of CAD as the underlying mechanisms of coronary plaque development that lead to disruption and acute thrombosis are multifactorial, involving a complex interaction between structural, compositional and biomechanical characteristics, and cellular and molecular processes in the vessel wall (5).

Fluorescence molecular imaging has been proposed to complement OCT for studying plaque pathobiological mechanisms (6,7). Intravascular near-infrared fluorescence (NIRF) using targeted molecular agents has been shown to elucidate inflammatory activity and fibrin accumulation in mice (8) and rabbit arteries (7,9), but these agents are not yet approved for human use. Detection of fluorescence from naturally occurring molecules, also known as autofluorescence, is closer to clinical application because it can be detected without the administration of exogenous agents. Autofluorescence excited in the UV and the visible portions of the electromagnetic

spectrum has been studied in human plaques *ex vivo* where the signal relates to elastin, collagen, and NADH (10,11). Recently, red-excited (633 nm) near-infrared autofluorescence (NIRAF), with emission detected between 700-900 nm, has been shown in cadaver coronary arteries to be specifically elevated in advanced, necrotic core containing lesions (12), including thin capped fibroatheroma (TCFA), the most common type of plaque implicated in acute coronary syndromes and acute myocardial infarction.

Based on the potential of OCT and NIRAF combination to improve our detection of necrotic core lesions and specifically TCFA, we developed a human-use OCT-NIRAF system and catheter. Here we describe a first-in-human safety and feasibility study of this multimodality intravascular imaging technology in patients and report our findings regarding the spatial distribution of the NIRAF signal with respect to co-localized OCT images of tissue microstructure *in vivo*.

METHODS

Patients

Patients undergoing PCI at Massachusetts General Hospital (Boston, MA) were enrolled between July 2014 and January 2015. All patients provided informed consent and the study was approved by the Massachusetts General Hospital (Partners Healthcare) institutional review board (IRB).

Dual-modality OCT-NIRAF imaging system

We created a dedicated, dual-modality OCT-NIRAF system that implements state-of-the-art OCT (1250-1370 nm) and NIRAF, excited at 633 nm and detected between 675 and 950 nm (**Supplementary Figure 1**). This system acquires synchronized OCT and NIRAF data at a rate of 100 frames/second. The OCT-NIRAF coronary imaging procedure is identical to that of current intravascular OCT, where volumetric (3D) OCT-NIRAF data are obtained by rotating and translating the driveshaft at a constant speed producing a helical scan.

Clinical intracoronary OCT-NIRAF imaging

As in routine clinical intravascular OCT imaging (1,2), the dual-modality catheter was advanced over a 0.014-inch guidewire and through a 6-F guide catheter placed into a coronary ostium. The OCT-NIRAF catheter was advanced distal to a lesion of interest

and images were acquired during a manual contrast injection at a rate of approximately 3-4 ml/sec for approximately 3 seconds. The driveshaft was retracted at a pullback speed of either 20 or 40 mm/sec. OCT-NIRAF imaging of the vessel undergoing PCI was performed in all cases, and additional major coronary vessels were imaged as time permitted.

Data Processing

NIRAF emission intensity data were processed by first subtracting the image background. We then automatically calibrated NIRAF emission intensities based on the distance between the catheter and the artery wall as determined by OCT, so that the fluorescence signal could be quantitatively compared between patients (6,13). Quantitative NIRAF data were normalized between 0 and 1 using the minimum and maximum NIRAF values acquired in the study. NIRAF data was displayed using a linear color look up table (white=high NIRAF, to dark blue=low NIRAF). OCT and NIRAF data were fused with the calibrated, normalized, and color-mapped NIRAF data, presented as an annulus around the gray scale OCT image, in a similar manner to that employed for NIRS-IVUS (14). *En face* two-dimensional (2D) NIRAF maps were also generated, similar in format to that of a NIRS chemogram, with the catheter's scan angle on the vertical axis and the pullback distance on the horizontal axis. OCT images were displayed using a logarithmic gray-scale look up table (15).

Three-dimensional (3D) reconstructions of OCT-NIRAF data were obtained after frame-to-frame semi-automatic registration to correct for artifacts generated by cardiac motion and mechanical scanning catheter-based acquisition. Plaques were manually segmented and different colors were assigned as follows: artery wall – gray, calcified plaques – white, and lipid-rich plaque – yellow. In addition, stent struts were automatically segmented (16,17) and rendered in red. Processed OCT-NIRAF images were imported into volume rendering software, (OsiriX 6.5.2,The OsiriX Foundation, Switzerland), and 3D data was visualized as volumes (perspective volume rendering) with semi-transparent opacity tables (15). The NIRAF signal was rendered over the artery wall with semi transparent opacity levels, tuned for optimal visualization.

Data analysis

In order to correlate the NIRAF emission intensities with the different plaque features, lesions were manually segmented using standard OCT image interpretation criteria

(1,2). Tissue type was categorized as: normal vessel wall, fibrotic, fibrocalcific, thick-cap fibroatheroma (ThCFA) if cap thickness >65 μm, thin-cap fibroatheroma (TCFA) if cap thickness <=65 μm, and plaque rupture. The plaques were selected by an expert OCT image reader (GJU) blinded to NIRAF data to avoid bias. Each plaque included multiple adjacent OCT-NIRAF frames. The maximum NIRAF signal intensity was calculated using all A-scan lines within the plaque. Plaques with a maximum NIRAF intensity >0.4 were arbitrarily classified as having a high NIRAF signal, moderate NIRAF plaques had a maximum signal between 0.2 and 0.4, low NIRAF lesions had a maximum signal between 0.05 and 0.2, and plaques negative for NIRAF were those with a maximum NIRAF signal <0.05. Macrophage accumulations within fibroatheroma caps were quantified using the normalized standard deviation (NSD) parameter (18). NSD values >7 (median value of the NSD range) were considered to be elevated in this study. This analysis was performed on each OCT fibroatheroma frames showing moderate or high NIRAF, and on an equally numbered, randomly selected set of atheroma frames showing low or absent NIRAF. Frames showing OCT image artifacts (e.g., NURD – non-uniform rotational distortion, seamline artifact or blood in the lumen) where excluded from all analyses. NIRAF signal reproducibility among repeated pullbacks from the same coronary segment was assessed by first registering two datasets using anatomical landmarks and known pullback speeds. A one-dimensional pullback plot was then generated for each NIRAF dataset by taking the maximum NIRAF signal for each frame for each pullback position. Reproducibility was quantified using Pearson's correlation coefficient computed from paired, one-dimensional NIRAF pullback datasets.

In order to quantify our observations that NIRAF is only elevated focally in OCT-delineated atherosclerotic plaques, we measured the fibroatheroma arc distribution in degrees as determined by OCT using the lumen's centroid as the origin and repeated the same procedure for NIRAF. These measurements were made for all the plaques imaged in this study that exhibited moderate or high NIRAF emission intensity. The same procedure was used to compare NIRAF and macrophage density (NSD) angular distributions.

Statistics

Statistical analysis reported in this study was performed using Matlab version 8.4.0 (MathWorks®, Natick, MA) and Matlab Statistics Toolbox version 9.1. One-way analysis of variance and pairwise Kruskal-Wallis analysis (with Mann-Whitney U test and without

adjustment for multiple comparisons) were used to compare maximum NIRAF between OCT-defined plaque type. No corrections for multiple observations within subjects or vessels were applied. Continuous data are expressed as mean ± standard deviation, or median (interquartile range) when appropriate, and p values <0.05 are considered statistically significant.

RESULTS

At total of 12 patients were imaged using the OCT-NIRAF catheter. **Table 1** depicts baseline characteristics of the enrolled patients. A total of 17 major coronary arteries were imaged simultaneously using co-localized OCT and NIRAF, encompassing 33 OCT-NIRAF pullbacks. Good quality OCT-NIRAF datasets (average length: 52 ± 10 mm) were obtained for each patient. The mean number of pullbacks per patient was 2.75 ± 1.23 and the average amount of contrast administered to each patient was 44 ± 26 ml, with a mean of 14±2 ml per OCT-NIRAF pullback. In a substudy of 4 repeated pullbacks, NIRAF reproducibility was excellent with an average Pearson's correlation coefficient of 0.925±0.015 (**Supplementary Figure 2**). There were no patient complications related to the OCT-NIRAF imaging procedure.

Description of representative clinical cases

Figure 1 shows an example of an OCT-NIRAF pullback from the right coronary artery (RCA) of a 67-year-old male patient who presented with in-stent restenosis of the mid-RCA. This pullback was acquired adjacent to the stented region located in the distal RCA, along a non-stenotic segment (**Figure 1A**). OCT imaging revealed a long segment of normal coronary wall and intimal hyperplasia with concomitant minimal NIRAF signal throughout (**Figures 1B, D**). A small calcific lesion located in the middle of the pullback was NIRAF negative (**Figure 1C**).

Strong NIRAF was only seen in regions of plaque with high-risk structural features (e.g., lipid-containing plaques, thin-fibrous caps, rupture with thrombus) as determined by OCT. **Supplementary Figure 4** shows an example of an OCT-NIRAF pullback acquired from the left-anterior descending (LAD) coronary artery of a diabetic 59-year-old male patient, presenting with left-circumflex (LCx) in-stent restenosis. The angiogram demonstrated diffuse atherosclerotic disease in the LAD. OCT imaging revealed multiple lesions in the LAD, including several fibrocalcific and lipid-rich plaques (**Supplementary Figures 4C-F, G**). A single, focal spot of elevated NIRAF signal was observed in the 2D

NIRAF map (**Supplementary Figure 4B**). The OCT image at this site in the mid LAD indicated the presence of a TCFA with an intact cap. Interestingly, the NIRAF signal was only elevated focally in this OCT-TCFA; in the cross-section displayed in **Supplementary Figure 4F**, high NIRAF was located at 9 o'clock, whereas the thin cap extended over a much larger arc, from 7 to 2 o'clock. All other plaques in this artery were OCT-delineated as fibrotic (**Supplementary Figure 4C**), fibrocalcific (**Supplementary Figure 4E**), or ThCFA (**Supplementary Figure 4D**), and exhibited negligible or low NIRAF signal.

High NIRAF was also found in arterial sites that contained OCT-evidence of plaque disruption/erosion and overlying thrombus. **Figure 2** shows an example of a TCFA rupture located in the LAD of a 66 year-old diabetic patient, presenting with significant stenosis of the proximal LCx (treated artery) and moderate stenosis of the proximal LAD. OCT imaging of the ostial LAD revealed a TCFA with cap rupture (**Figures 2C-H**), including a platelet-rich thrombus overlying the site of cap disruption (**Figures 2D, G**). NIRAF was elevated focally within the OCT-TCFA at the rupture site (**Figures 2E, H**) and at an adjacent location that contained a cholesterol crystal (**Figures 2C, F**). In this pullback, OCT revealed several other lipid-containing plaques (**Figure 2I**) that were all negative for NIRAF.

The OCT-NIRAF catheter was also used to image early in-stent restenosis (86 days after BMS implantation) in the left-circumflex coronary artery (LCx) of the diabetic patient described in section 3.2. Because of severe restenosis (70%), OCT-NIRAF was conducted after balloon pre-dilatation. In the proximal and middle region of the stented segment, OCT imaging revealed that a portion of the stent was deployed overlying a large fibroatheroma (**Figure 3**). An elevated NIRAF signal was observed in this area (**Figure 3B, C**). The remaining in-stent restenotic tissue had an OCT appearance of neointimal hyperplasia and exhibited minimal NIRAF signal (**Figure 3E**).

OCT-NIRAF quantitative analysis

Patient imaging findings revealed NIRAF emission intensity patterns that were distinct from structural or compositional patterns seen with other intravascular coronary imaging modalities (e.g. OCT, IVUS, NIRS) *in vivo*. From the 17 coronary arteries imaged in this study, a high focal NIRAF signal was found in 5 arteries (29%), a low to moderate NIRAF signal was found in 4 arteries (24%) while all the other arteries (n=8, 47%) were NIRAF negative. Following analysis of each pullback, a total of 79 distinct

plaques were identified as described in the methods section. The maximum NIRAF signal intensity of each plaque was compared to OCT-defined type (**Figure 4**). There was a statistically significant difference of maximum NIRAF signal between plaque types (one-way analysis of variance, $p<0.0001$). OCT-delineated TCFA and plaque rupture cases demonstrated much higher maximum NIRAF signal than all other plaque ($p<0.05$). All other groups were statistically different from each other ($p<0.05$), with the exception of fibrocalcific plaques and ThCFA ($p=0.65$). While there were only two plaque ruptures identified in this cohort, the maximum NIRAF signal for rupture sites was non-significantly higher than that of unruptured TCFA ($p=0.07$) (**Figure 4**).

By comparing OCT and NIRAF lipid arcs, we observed that NIRAF contiguously spanned 23.2%±13% (mean ± standard deviation) of the total arc of lipid in OCT fibroatheroma. These findings indicate that in all areas where NIRAF was elevated, it only peaked at specific discrete loci.

OCT-macrophage accumulation analysis (92 OCT-fibroatheroma frames analyzed) demonstrated that NIRAF is focally associated with OCT measurement of macrophage-rich inflammation, as estimated by the NSD parameter (18). When NIRAF was high, it was always found in areas of elevated NSD (**Supplementary Figure 3**) but not all areas of high NSD exhibited high NIRAF. Furthermore, NIRAF was only elevated discretely in regions of elevated NSD as NIRAF covered 39.2%±12.5% of the elevated NSD arc.

DISCUSSION

In this paper, we present a first-in-human investigation of multimodality intracoronary OCT and near-infrared autofluorescence (NIRAF) imaging *in vivo*. Our results show that OCT-NIRAF uncovers a unique autofluorescence signature of human coronary atherosclerosis *in vivo*. The intracoronary NIRAF-OCT procedure was safe and was utilized in patients similarly to conventional intravascular OCT. Importantly, co-registration and distance correction of OCT and NIRAF data was inherently automatic and facilitated image interpretation. Data acquisition was reliable and NIRAF was found to be reproducible amongst multiple pullbacks.

By investigating the spatial relationship between NIRAF and arterial morphological features *in vivo*, we found that elevated NIRAF was associated with morphologic and/or mechanistic features of high plaque risk. NIRAF was negative or low in plaques with a low-risk microstructural phenotype as determined by OCT (intimal hyperplasia, fibrous plaque, and fibrocalcific plaque). In contrast, NIRAF was high focally in certain OCT-

delineated fibroatheromas and highest in OCT-delineated TCFA, regions of cap disruption, and areas of fibroatheroma associated with in-stent restenosis. Results of this study also associate elevated NIRAF with indicators of inflammation. NIRAF was found to be only elevated in plaque regions that showed OCT evidence of macrophage accumulations. In combination with our previous *ex vivo* study (12), these findings support our original rationale for combining OCT and NIRAF to better delineate and characterize atherosclerotic lesions that are at risk of progression. Although the correlation shown here between NIRAF and plaque inflammation has been established using an objective method for OCT image quantification (18,19) these results should be considered hypothesis generating. Plaque components other than macrophages give rise to an appearance of punctate high OCT signal regions and OCT has not been demonstrated to distinguish between active and inactive macrophages and other macrophage subtypes (20).

The focal spatial distribution of the NIRAF signal was a major unexpected finding of this study that supports the potential additive nature of this imaging biomarker. Elevated NIRAF signal occurred only at discrete locations and for example did not subtend the entire fibroatheroma or the entire arc of thin fibrous caps. In addition, NIRAF was only high focally in regions with OCT evidence of high macrophage accumulations, however the converse was not true in that there were many elevated NSD areas that were NIRAF negative. The observation that NIRAF is only focally elevated in plaques with macrophage accumulations is consistent with concept of multiple macrophage phenotypes in atherosclerotic lesions.

Additional studies are merited to uncover the specific molecular/chemical mechanisms that produce NIRAF in atherosclerotic plaque to fully understand the biological and clinical relevance of this signal. Based on the findings of this study and information gleamed from the literature (21,22), various hypotheses can be made about the potential sources of NIRAF in atherosclerotic plaques and its potential relationship to coronary wall inflammation. NIRAF in atherosclerotic plaque may arise from the modification of lipids and lipoproteins by oxidative stress (21,22). Studies have shown that ceroid, a protein-lipid oxidation byproduct found in atherosclerotic plaque, has a yellow fluorescence spectrum (22) and it is possible that the tail of ceroid's fluorescence emission may extend into the NIR. Oxidative stress caused by inflammatory activity may also cross-link surrounding proteins, creating dimers such as dityrosine that are fluorescent in the NIR (21). Other reports in cancerous tissues (23) have observed tissue

autofluorescence, suggesting that it could arise from endogenous porphyrins. Extrapolating to atherosclerosis, it is possible that intraplaque hemorrhage that contributes to lesion development and destabilization may give rise to porphyrins that could in part explain the NIRAF signal observed here.

Although the focal appearance of the NIRAF signal could be due high biological/spatial specificity of the molecular/chemical entity generating the fluorescence, it also could in part be influenced by the spatial locations of the fluorophores and NIRAF light propagation given the surrounding tissue's optical properties. To better characterize the autofluorescence signal detected *in vivo*, OCT-NIRAF instrumentation can be augmented by detecting the emitted light using a spectrometer rather than a single integrating detector. Use of a spectrometer will allow for the analysis of the spectral content of the NIRAF emission signal that may help to determine its molecular/chemical origins. Furthermore, spectral detection can potentially be used to correct for variations of NIRAF signal intensity that are due to the location of the fluorophores in the artery wall and the propagation of NIRAF light through plaque, which may have heterogeneous optical properties.

Study limitations

In this study, we imaged a limited number of patients with relatively low risk clinical presentations (Canadian Classification System Class II and Class III angina pectoris). Intravascular OCT-NIRAF imaging studies in larger cohorts that include acute coronary syndrome and ST-segment elevation myocardial infarction patients will be required in order to confirm and expand our findings. Although our data allows a preliminary assessment of the associations between the NIRAF signal and plaque morphology and microstructure, the small size of this study and our inability to acquire specimens for advanced tissue analysis prevent us from making definitive conclusions about the biological or molecular nature of the NIRAF signal. Although these results demonstrate the potential for this NIRAF plaque signature to refine the identification of high-risk plaques *in vivo*, the applicability of these new lesion characteristics to clinical screening and coronary event prediction remain to be demonstrated as well as the accuracy in assigning an increased risk to plaques with high NIRAF.

CONCLUSIONS

In our first-in-human experience with intracoronary OCT-NIRAF, we have demonstrated that a unique human coronary autofluorescence signature can be detected in CAD patients *in vivo*. The multimodal OCT-NIRAF structural and fluorescence intracoronary imaging can be conducted in patients with similar ease and safety as that of conventional, standalone intravascular OCT. Findings show that NIRAF is focally elevated in plaque locations where most high-risk morphologic phenotypes are evident. Future investigations will elucidate the specific molecular nature of the NIRAF signal and its pathobiological and clinical relevance. In addition to NIRAF, this work paves the way for demonstrating intravascular OCT and targeted molecular fluorescence in human patients. Such multimodality technologies that combine microstructural and fluorescence imaging will perhaps further expand our armamentarium of tools for coronary plaque diagnosis, improving our capacity to predict plaque progression and refine patient and lesion-specific risk.

Acknowledgments

The authors thank Dr. Amna Soomro and Dr. Aubrey Tiernan (Tearney Lab clinical regulatory team) and Luke Stone (clinical research coordinator at the Cardiology Division of Massachusetts General Hospital) for their help with patient enrollment. Authors also acknowledge: Daryl Hyun and Robert Carruth (Tearney Lab engineering team) for their assistance with system and catheters manufacturing; Martin Seifert, Dr. Kanishka Tankala, Dr. George Oulundsen and Harish Govindarajan (NUFERN, East Granby, CT, USA) for their help developing and manufacturing the optical fiber used in this study; and Terumo Medical Corporation (Tokyo, Japan) for providing catheter material supplies. Authors also acknowledge financial support from Canon USA (support of new technology advancement in OCT-NIRAF), NIH R01HL093717 (GJT—development of imaging system and imaging of the first two patients), NIH R01HL HL122388 (FAJ), AHA Grant-in-Aid 13GRNT1760040 (FAJ) and Bullock-Wellman Fellowship Award, Harvard Medical School (GJU).

REFERENCES

1. Bezerra HG, Costa MA, Guagliumi G, Rollins AM, Simon DI. Intracoronary optical coherence tomography. JACC Cardiovascular interventions 2009;2:1035-46.
2. Tearney GJ, Regar E, Akasaka T et al. Consensus standards for acquisition, measurement, and reporting of intravascular optical coherence tomography studies. J Am Coll Cardiol 2012;59:1058-72.
3. van Soest G, Regar E, Goderie TP et al. Pitfalls in plaque characterization by OCT. JACC Cardiovascular imaging 2011;4:810-3.
4. Imanaka T, Hao H, Fujii K et al. Analysis of atherosclerosis plaques by measuring attenuation coefficients in optical coherence tomography. European heart journal 2014;34.
5. Finn AV, Nakano M, Narula J, Kolodgie FD, Virmani R. Concept of vulnerable/unstable plaque. ATVB 2010;30:1282-92.
6. Yoo H, Kim JW, Shishkov M et al. Intra-arterial catheter for simultaneous microstructural and molecular imaging in vivo. Nature medicine 2011;17:1680-4.
7. Vinegoni C, Botnaru I, Aikawa E et al. Indocyanine green enables near-infrared fluorescence imaging of lipid-rich, inflamed atherosclerotic plaques. Science translational medicine 2011;3:84ra45.
8. Hara T, Bhayana B, Thompson B et al. Molecular imaging of fibrin deposition in deep vein thrombosis using fibrin-targeted near-infrared fluorescence. JACC Cardiovascular imaging 2012;5:607-15.
9. Lee S, Lee MW, Cho HS et al. Fully integrated high-speed intravascular optical coherence tomography/near-infrared fluorescence structural/molecular imaging in vivo using a clinically available near-infrared fluorescence-emitting indocyanine green to detect inflamed lipid-rich atheromata in coronary-sized vessels. Circulation Cardiovascular interventions 2014;7:560-9.
10. Marcu L, Fishbein MC, Maarek JM, Grundfest WS. Discrimination of human coronary artery atherosclerotic lipid-rich lesions by time-resolved laser-induced fluorescence spectroscopy. ATVB 2001;21:1244-50.
11. Baraga JJ, Rava RP, Taroni P, Kittrell C, Fitzmaurice M, Feld MS. Laser induced fluorescence spectroscopy of normal and atherosclerotic human aorta using 306-310 nm excitation. Lasers Surg Med 1990;10:245-61.

12. Wang H, Gardecki JA, Ughi GJ, Jacques PV, Hamidi E, Tearney GJ. Ex vivo catheter-based imaging of coronary atherosclerosis using multimodality OCT and NIRAF excited at 633 nm. Biomedical optics express 2015;6:1363-75.
13. Ughi GJ, Verjans J, Fard AM et al. Dual modality intravascular optical coherence tomography (OCT) and near-infrared fluorescence (NIRF) imaging: a fully automated algorithm for the distance-calibration of NIRF signal intensity for quantitative molecular imaging. Int J Cardiovasc Imaging 2015;31:259-68.
14. Madder RD, Goldstein JA, Madden SP et al. Detection by near-infrared spectroscopy of large lipid core plaques at culprit sites in patients with acute ST-segment elevation myocardial infarction. JACC Cardiovascular interventions 2013;6:838-46.
15. Tearney GJ, Waxman S, Shishkov M et al. Three-dimensional coronary artery microscopy by intracoronary optical frequency domain imaging. JACC Cardiovascular imaging 2008;1:752-61.
16. Ughi GJ, Adriaenssens T, Onsea K et al. Automatic segmentation of in-vivo intra-coronary optical coherence tomography images to assess stent strut apposition and coverage. Int J Cardiovasc Imaging 2012;28:229-41.
17. Ughi GJ, Van Dyck CJ, Adriaenssens T et al. Automatic assessment of stent neointimal coverage by intravascular optical coherence tomography. European heart journal cardiovascular Imaging 2014;15:195-200.
18. MacNeill BD, Jang IK, Bouma BE et al. Focal and multi-focal plaque macrophage distributions in patients with acute and stable presentations of coronary artery disease. J Am Coll Cardiol 2004;44:972-9.
19. Di Vito L, Agozzino M, Marco V et al. Identification and quantification of macrophage presence in coronary atherosclerotic plaques by optical coherence tomography. European heart journal cardiovascular Imaging 2015;16:807-13.
20. Phipps JE, Vela D, Hoyt T et al. Macrophages and intravascular OCT bright spots: a quantitative study. JACC Cardiovascular imaging 2015;8:63-72.
21. Malencik DA, Anderson SR. Dityrosine as a product of oxidative stress and fluorescent probe. Amino Acids 2003;25:233-47.
22. Haka AS, Kramer JR, Dasari RR, Fitzmaurice M. Mechanism of ceroid formation in atherosclerotic plaque: in situ studies using a combination of Raman and fluorescence spectroscopy. Journal of biomedical optics 2011;16:011011.

23. Yang YL, Ye YM, Li FM, Li YF, Ma PZ. Characteristic autofluorescence for cancer diagnosis and its origin. Lasers Surg Med 1987;7:528-32.

Baseline characteristics	N =12
Mean age (years)	63.3 ± 7.6
Male gender, n (%)	11 (91.2)
Hypertension, n (%) *	11 (91.2)
Family history of premature heart disease, n (%)	3 (25.0)
Prior coronary artery disease	8 (66.6)
Prior myocardial infarction, n (%)	2 (16.6)
Prior PCI, n (%)	5 (41.7)
Smoking status	
Never smoked, n (%)	6 (50.0)
Ex-smoker, n (%)	5 (41.7)
Current smoker, n (%)	1 (8.3)
Hyperlipidemia, n (%)	11 (91.2)
Hyperlipidemia currently taking medication, n (%)	9 (75.0)
LDL mg/dL, mean ± SD	99 ± 33
HDL mg/dL, mean ± SD	43 ± 11
Triglycerides mg/dL, mean ± SD	123 ± 63
Body-mass index (kg/m^2), n, median, Q1-Q3	28.0 (24.8-30.4)
Diabetes mellitus, n (%)	4 (33.3)
Medication	
Statins, n (%)	9 (75.0)
Beta-blocker, n (%)	8 (66.6)
ACEi or A2 receptor blockers, n (%)	6 (50.0)
Nitrates, n (%)	8 (66.6)
Diuretics, n (%)	4 (33.3)
Aspirin or clopidogrel, n (%)	11 (91.2)
Anticoagulant, n (%)	1 (8.3)
Angina pectoris class	
CCS I, n (%)	0 (0.0)
CCS II, n (%)	8 (66.6)
CCS III, n (%)	4 (33.3)
CCS IV, n (%)	0 (0.0)
Angiography indication	
Chest pain	5 (41.7)
Positive functional study	7 (58.3)
Stented Vessel (PCI)	
LAD	4
LCx	3
RCA	5
*hypertension is defined by systolic blood pressure ≥ 140 mmHg and/or diastolic blood pressure ≥ 90 mmHg.	

Table 1. Patient baseline characteristics on admission. All patients presented with stable angina pectoris (SAP), either Class II or Class III. Categorical variables are expressed as numbers (%) and continuous variables are reported as mean ± standard deviation or medians (interquartile ranges) for body-mass index. CCS – Canadian Classification System for stable angina pectoris.

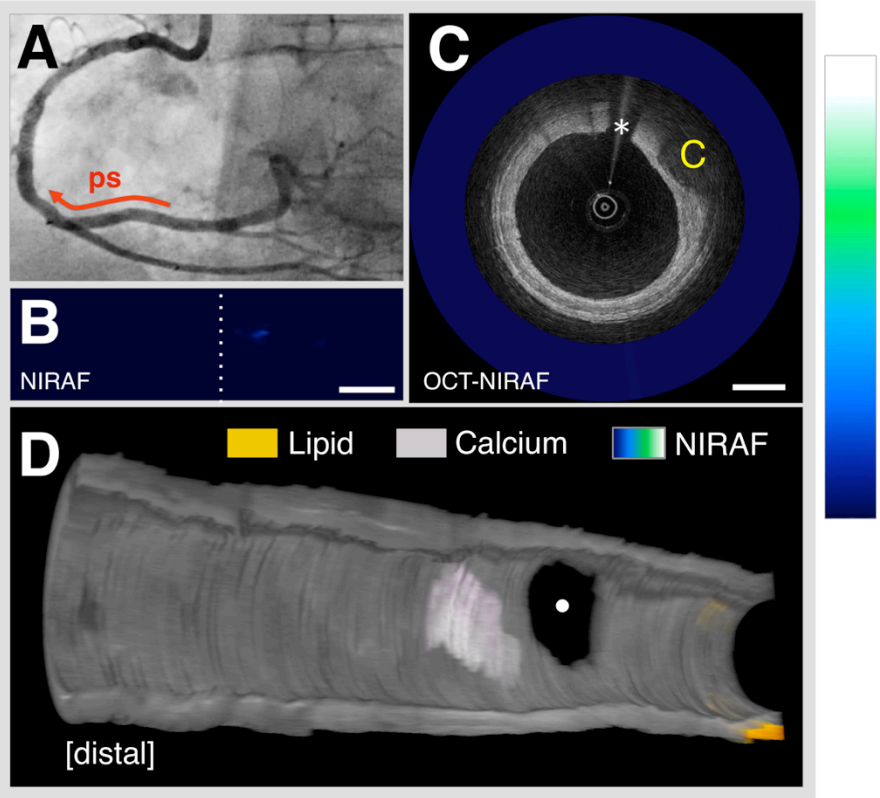

Fig. 1. Coronary segment negative for NIRAF. (A) Angiography of RCA showing non-significant coronary disease over the OCT-NIRAF pullback segment (ps). (**B**) 2D NIRAF map demonstrating negligible NIRAF signal. (**C**) Cross sectional OCT-NIRAF image showing normal coronary wall and a calcification (2 o'clock) with no NIRAF signal detected. (**D**) 3D cutaway rendering of the OCT-NIRAF pullback. Scale bar in (**C**) equal to 1 mm; scale bar in (**B**) equal to 5 mm. *, guide-wire shadowing artifact; •, side-branch.

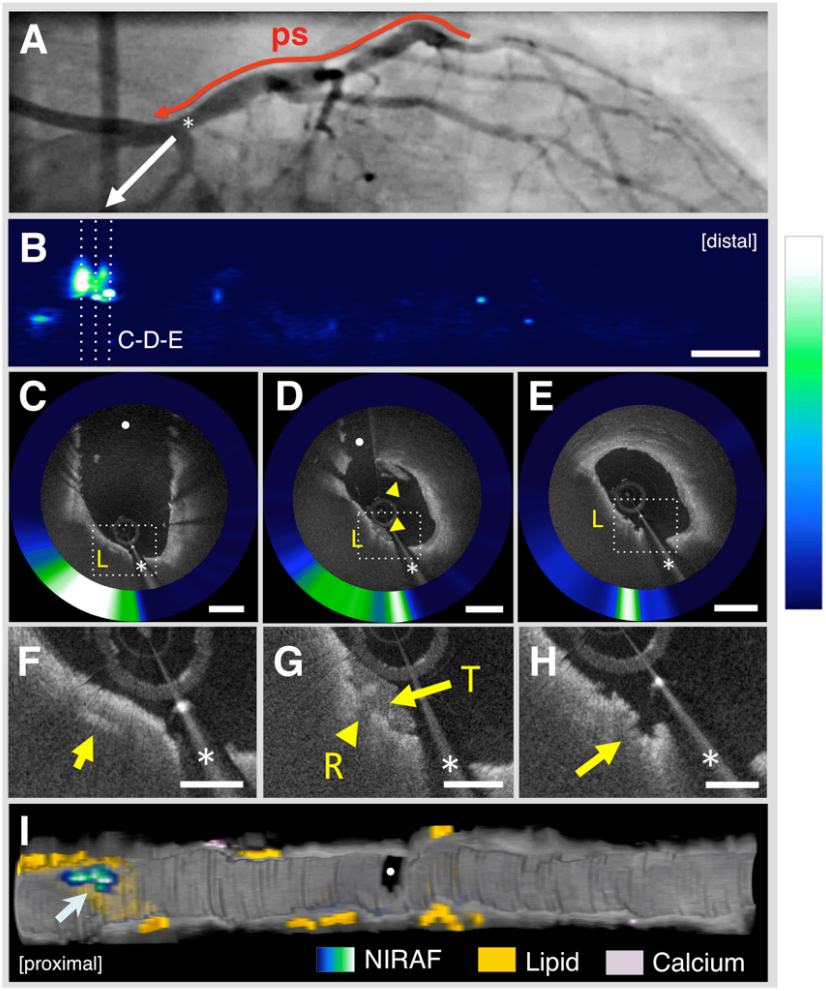

Fig. 2. OCT-NIRAF imaging of TCFA rupture. (**A**) Coronary angiogram of LAD and (**B**) 2D NIRAF map showing a focal region of elevated NIRAF in the ostial LAD. (**C, D, E**) OCT-NIRAF cross-sections from sites in (**B**) with elevated NIRAF, revealing subclinical OCT-TCFA fibrous cap rupture. (**F**) Magnification of a cholesterol crystal below the cap, co-localized with high NIRAF, and (**G, H**) magnified views of the rupture site. In (**G**), the rupture site (arrowhead) is covered by a small white luminal thrombus (arrow) and the arrow in (**H**) points to the site of the thin-cap rupture, demonstrating co-localized and very high focal NIRAF signal. (**I**) 3D cutaway rendering showing that the highest NIRAF spot appears focally within a large lipid pool (arrow), and the remaining portion of the vessel shows diffuse disease that was negative for NIRAF. Scale bars on OCT images and magnifications are equal to 1 mm and 0.5 mm, respectively; scale bar in (**B**) is equal to 5 mm. ps, pullback segment; L, lipid; R, rupture site; T, thrombus.

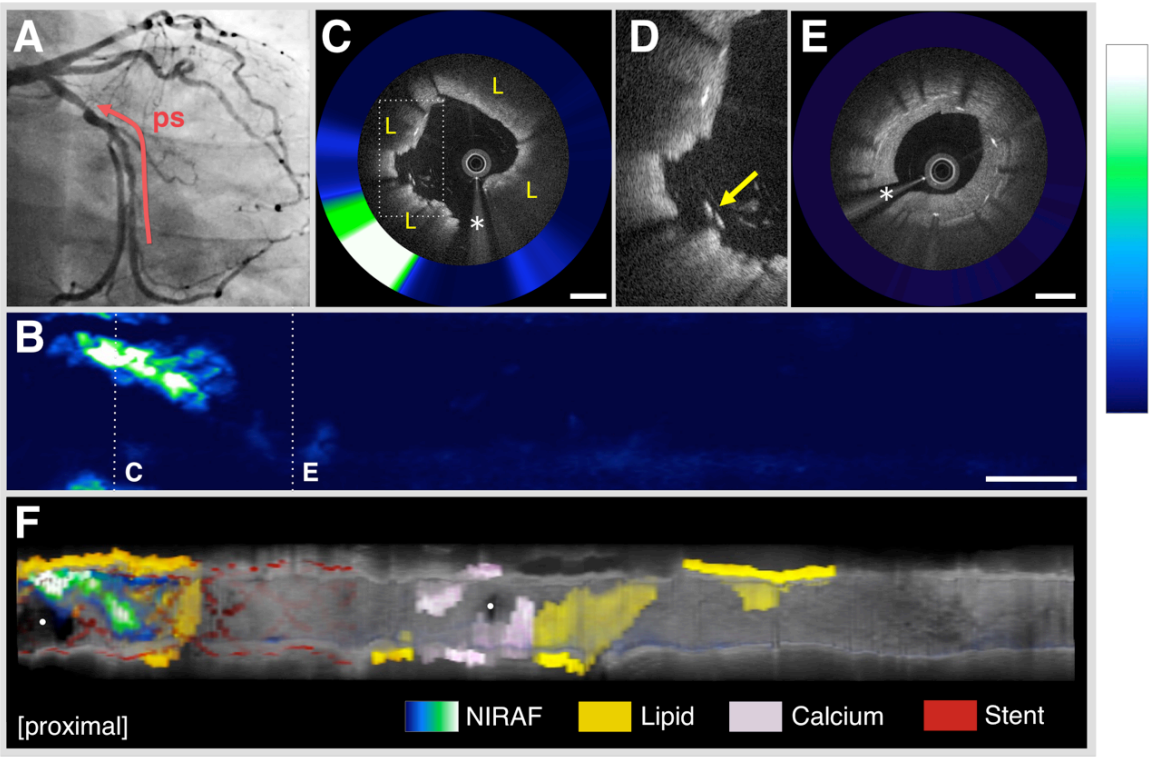

Fig. 3. OCT-NIRAF imaging of in-stent restenosis. (**A**) Angiography of LCx and (**B**) 2D NIRAF map. (**C**) Cross-sectional OCT-NIRAF image, showing a focal site with elevated NIRAF co-localized with stent struts overlying an OCT-delineated fibroatheroma. The arrow in (**D**) identifies OCT uncovered stent struts, a marker of incomplete stent healing. (**E**) Cross-sectional image from the distal portion of the stent that is negative for NIRAF, showing in-stent restenosis and non-attenuating OCT tissue suggesting intimal hyperplasia and presence of fibrotic tissue. (**F**) 3D cutaway rendering illustrating that the highest NIRAF signal is co-localized with mid and proximal stent segment and with the tissue with high OCT signal attenuation (fibroatheroma). Scale bars on OCT images are equal to 1 mm; scale bar on (**B**) is equal to 5 mm. ps, pullback segment; L, lipid.

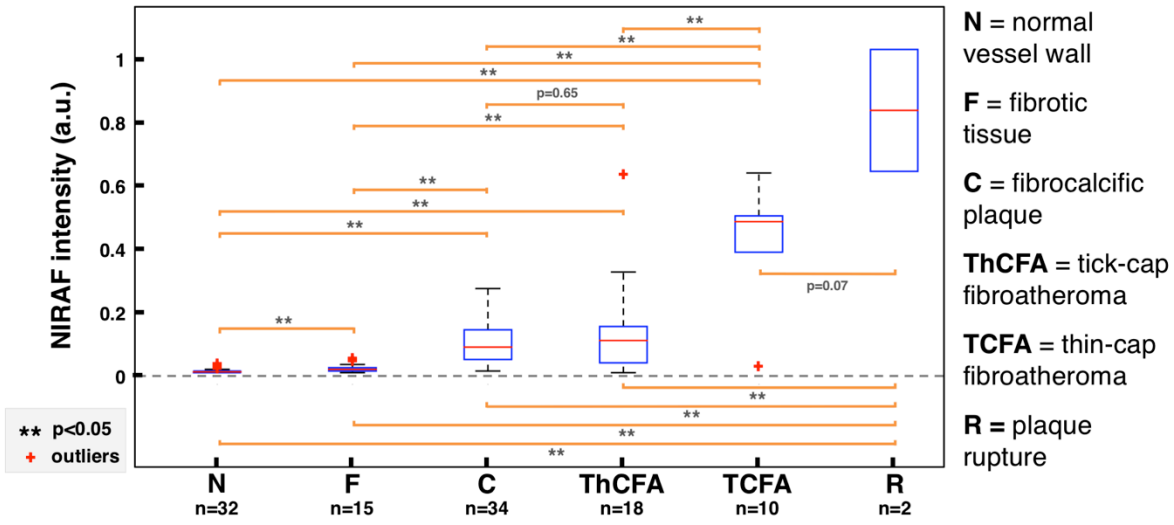

Fig. 4. Analysis of maximum NIRAF plaque intensities for different plaque types. Values from normal vessel wall and fibrotic plaques were significantly different from each other ($p<0.05$), demonstrating a lower signal intensity than that of fibrocalcific plaques ($p<0.05$). Fibrocalcific plaques and ThCFA showed moderate maximum NIRAF signal intensities that were not significantly different from each other ($p=0.65$). A higher maximum NIRAF signal was detected from sites of plaque rupture ($p<0.05$) and TCFA ($p<0.05$). Whisker lengths are defined as +/-2.7σ, and points are drawn as outliers if outside the range [q1 – w(q3 – q1)] and [q3 + w(q3 – q1)], where q1 and q3 are the 25th and 75th percentiles, respectively. a.u. = normalized NIRAF intensity.

SUPPLEMENTARY MATERIALS for:

Clinical Characterization of Coronary Atherosclerosis With Dual-Modality OCT and Near-Infrared Autofluorescence Imaging

Giovanni J. Ughi, PhD,[1] Hao Wang, PhD,[1] Edouard Gerbaud, MD,[1] Joseph A. Gardecki, PhD,[1] Ali M. Fard, PhD,[1] Ehsan Hamidi, PhD,[1] Paulino Vacas-Jacques, PhD,[1] Mireille Rosenberg, PhD,[1] †Farouc A. Jaffer, MD, PhD, FACC,[1,2] and †Guillermo J. Tearney, MD, PhD, FACC, FCAP*[,1,3,4]

[1]Wellman Center for Photomedicine, Harvard Medical School and Massachusetts General Hospital, Boston, MA, USA

[2]Cardiovascular Research Center and Cardiology Division, Harvard Medical School and Massachusetts General Hospital, Boston, MA, USA

[3]Department of Pathology, Massachusetts General Hospital and Harvard Medical School, Boston, MA

[4]Harvard-MIT Health Sciences and Technology, Boston, MA

[†]Dr. Jaffer and Dr. Tearney share senior authorship.

This document includes:

- **Dual-modality OCT-NIRAF imaging catheter**
- **Supplementary Figure 1**: Schematic of the OCT-NIRAF system
- **Supplementary Figure 2**: Reproducibility between different human intracoronary OCT-NIRAF acquisitions *in vivo*
- **Supplementary Figure 3**: Macrophage density analysis (NSD) over fibrotic caps of OCT fibroatheromas, and compared to co-localized NIRAF
- **Supplementary Figure 4:** OCT-NIRAF imaging of TCFA

Dual-modality OCT-NIRAF imaging catheter

The catheter transmits and receives light using a newly developed double clad optical fiber (DCF) with a reduced fiber-generated fluorescence background (FUD-4305, NUFERN, East Granby, CT). NIRAF signal was detected between 675 and 900 nm, which excluded the detection of stimulated Raman scattering from the catheter's optical fiber. The core of the DCF transceives OCT and transmits NIRAF excitation light, while the NIRAF emission is relayed from the artery to the fluorescence detector through the inner cladding of the DCF (6,11). Light is transmitted between the system and the spinning optics within the catheter, by the means of a dual-modality optical rotary joint fabricated in-house (**Supplementary Figure 1**). The single mode optical throughput variation during a full rotation was measured to be ±0.3 dB. While our DCF rotary joint performed well, DCF optical rotary joints are relatively new components and may be less reliable than single-mode fiber rotary joints used in conventional intravascular OCT. We do not anticipate that this limitation will remain following the introduction of DCF rotary junctions in commercial multimodality systems. The NIRAF excitation spot size was ~35 μm with a power of 5 mW and the NIRAF system was capable of detecting <10 nM of a standard fluorescent dye (i.e., Alexa Fluor® 633 NHS Ester). After the clinical imaging procedure was finished, NIRAF was measured by inserting each catheter in a standard solution containing a known concentration (100 nM) of a fluorescent dye (Alexa Fluor® 633 NHS Ester). For all the catheters used in this study, inter-catheter NIRAF emission detection variability was <5%.

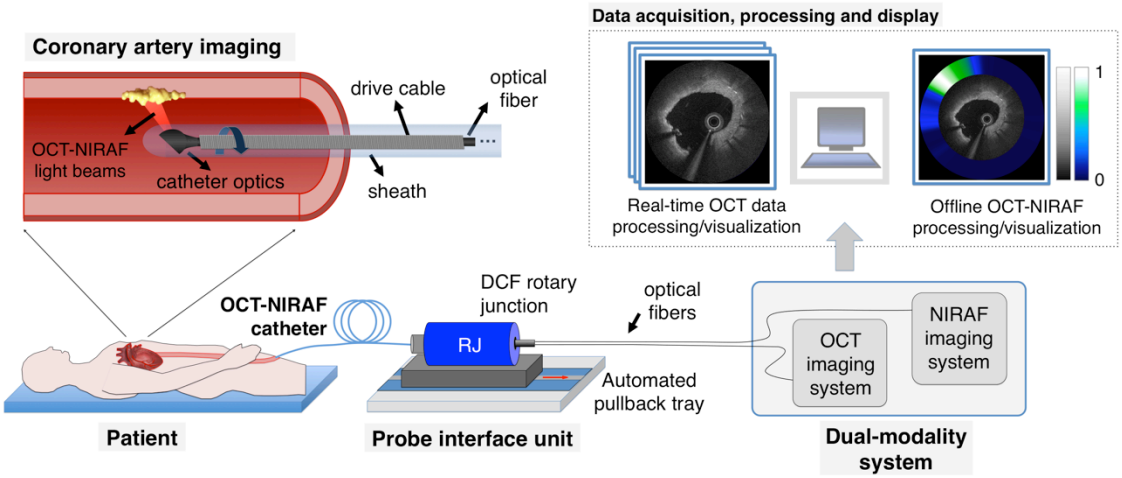

Supplementary Fig. 1. Schematic of the OCT-NIRAF system. Imaging of coronary arteries *in vivo* is accomplished by focusing OCT and NIRAF excitation light from the tip of the catheter onto the artery wall. Three-dimensional OCT and NIRAF datasets are simultaneously obtained by helically scanning the artery wall through rotation and translation of the driveshaft within the catheter's sheath at a constant speed. OCT and NIRAF light is combined at the dual-modality rotary joint that separates the OCT and NIRAF excitation and emission light by the means of dichroic mirrors. Data from both modalities are collected using a computer workstation, processed, and the OCT image is displayed in real time. NIRAF data are processed with a distance-dependent algorithm and displayed offline as 2D NIRAF maps and as multimodality cross-sectional OCT-NIRAF images.

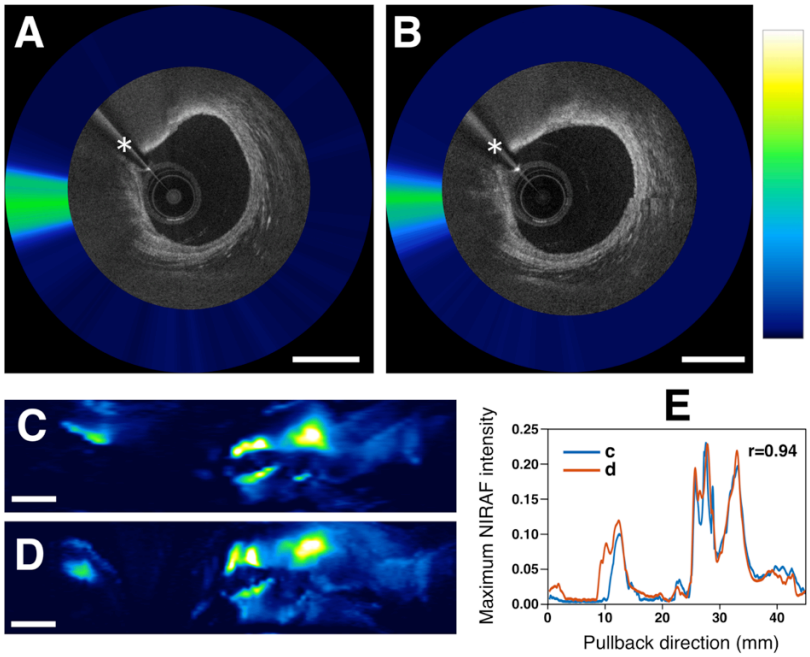

Supplementary Fig. 2: **Reproducibility between different human intracoronary OCT-NIRAF acquisitions *in vivo*.** (**A**, **B**) An example of reproducibility among cross-sectional OCT-NIRAF images (20 mm per second pullbacks), where both similar OCT image features and NIRAF signal intensities can be observed from the same vessel wall locations. (**C, D**) 2D NIRAF maps of the same artery acquired sequentially and (**E**) quantitative NIRAF signal analysis (maximum NIRAF signal per frame) showing a high correlation r=0.94 (p<0.001) between the two acquisitions illustrated in (**C**) and (**D**). Scale bars in (**A**) and (**B**) are equal to 1 mm; scale bars in (**C**) and (**D**) are equal to 5 mm; (*) indicates guide-wire shadowing artifact.

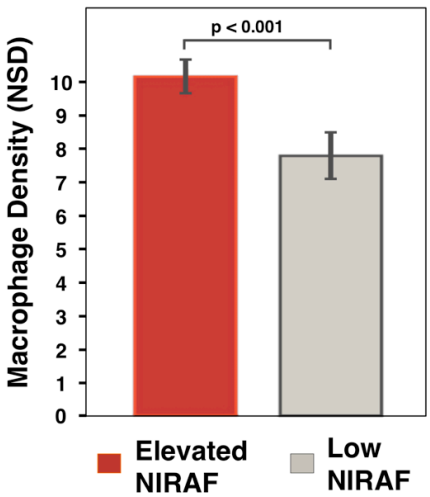

Supplementary Fig. 3. Macrophage density analysis (NSD) over fibrotic caps of OCT fibroatheromas, and compared to co-localized NIRAF. Caps of lipid plaques with elevated NIRAF showed significantly higher NSD than caps with low NIRAF (p<0.001).

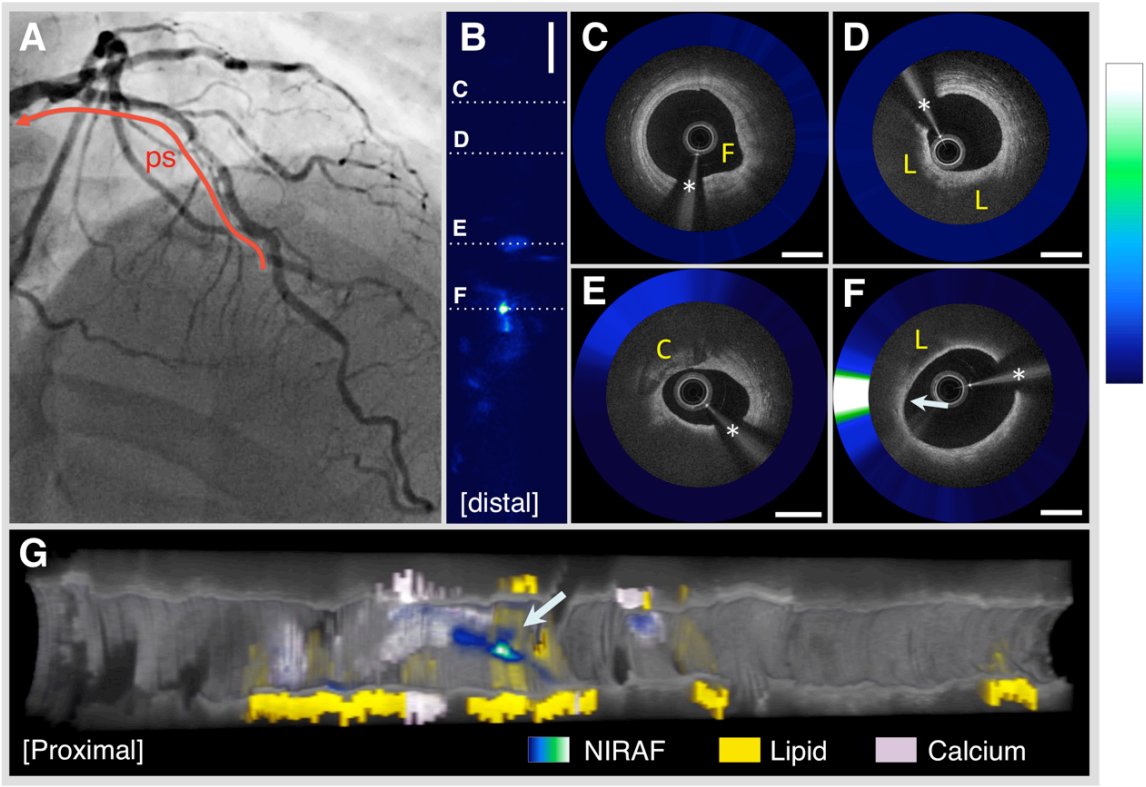

Supplementary Fig. 4. OCT-NIRAF imaging of TCFA. (**A**) Coronary angiogram of LAD and (**B**) 2D NIRAF map showing a single, focal spot exhibiting elevated NIRAF. (**C**) OCT-NIRAF cross-sectional image showing a fibrotic plaque with no NIRAF; (**D**) lipid-rich lesion negative for NIRAF; and (**E**) fibrocalcific plaque showing low NIRAF signal. (**F**) Cross-sectional OCT-NIRAF image taken from the location in (**B**) with high NIRAF, demonstrating a circumferential OCT fibroatheroma with a thin (<65 μm) fibrous cap from 7 to 2 o'clock and focal very high NIRAF signal (9 o'clock) (arrow). (**G**) 3D rendering of the OCT pullback dataset with overlaid NIRAF, showing that the NIRAF was only elevated focally over a specific location of the lipid-containing OCT fibroatheroma (arrow). Scale bars on OCT-NIRAF images are equal to 1 mm; scale bar in (**B**) is equal to 5 mm; ps, pullback segment; C, calcium; F, fibrotic; L, lipid.

General conclusion

In several circumstances, intravascular imaging including IVUS and OFDI have clearly an additional value when they are used as a diagnosis tool in case of angiographic ambiguities. We recently reported the first observation to describe a coronary dissection of a septal perforating branch causing AMI. Another adjunctive tool of these technologies is when they are used as a strategy to guide PCI. However, in our work, we observed that in the measurement of lumen CSA, maximum and minimum lumen diameters, stent CSA, maximum and minimum stent diameters by analysts from 2 different laboratories, inter-institute reproducibility of OFDI was found to be more consistent than IVUS. Inter-institute agreement was substantial using both technologies for plaque composition. These findings may have important implications for the design of future studies evaluating PCI optimization using intravascular imaging and pooling several parameters measured by multiple institutions.

The next objective for the physician is to perform precision medicine in PCI: local therapy tailored to each given target lesion in an individual patient. In this context, detecting vulnerable plaques in order to propose a preventive strategy is of major interest, i.e. local (mechanical or pharmacological) treatment of future culprit lesions or seeing a heart attack before it happens. Today one dual-probe catheter has been commercialized, i.e. infrared spectroscopy-intravascular ultrasound (NIRS-IVUS). And several intravascular hybrid imaging technologies have been introduced including combined IVUS-optical coherence tomography (OCT), the OCT-near infrared fluorescence (NIRF) molecular imaging, IVUS-NIRF, IVUS intravascular photoacoustic imaging and combined fluorescence lifetime-IVUS imaging. These multimodal approaches may be able to overcome limitations of standalone imaging and provide comprehensive visualization of plaque composition and plaque biology. In the same way, some new modalities like micro-OCT at bench are able to improve the spatial resolution of standard intravascular OCT imaging. In this thesis, we presented 2 new robust hybrid intravascular imaging technologies developed in Dr. Tearney's laboratory i.e. OFDI-NIRS and OFDI-NIRAF, which may have offer supplementary criteria for vulnerability. First-in-human OFDI-NIRS imaging procedures are anticipated in the near future. First-in-human OFDI-NIRAF imaging procedures have been performed in a first pioneering series of 12 stable patients between July 2014 and January 2015. Findings of this pilot study showed that NIRAF was focally elevated in plaque

locations where most high-risk morphologic phenotypes were evident. The contrast mechanism in NIRAF - tissue fluorescence is physically distinct from OCT - optical scattering and other modalities. Whether the information it presents is also independent still debated: the biochemical substrates of the signal still have to be elucidated. Future investigations will clarify the specific molecular nature of the NIRAF signal.

Furthermore, the next step to evaluate the additional value of NIRAF in human patients, would be to test this hybrid catheter in patients presenting with acute coronary syndrome. We may expect that new NIRAF phenomena or signatures will appear. In addition to NIRAF, this work paves the way for demonstrating intravascular OCT and targeted molecular fluorescence in human patients. Finally, the future of intravascular imaging may be a multi-modality intravascular OCT catheter including NIRAF, NIRS and others modalities in order to better characterize atherosclerotic plaques in stable and unstable patients, improving their prevention and survey, and guiding the treatment.

Summary

Intravascular imaging technologies i.e. IVUS and IV-OCT are valuable tools for intervention guidance and diagnostic plaque imaging. The aim of this thesis is to evaluate the additional value of several different IV-OCT modalities to explore atherosclerotic plaque.

Chapter 1 introduces the drawbacks of coronary angiography in the clinical practice. In several circumstances, IVUS and IV-OCT have clearly an additional value when they are used as a diagnosis tool in case of angiographic ambiguities. We recently reported the first observation using IV-OCT to describe a coronary dissection of a septal perforating branch causing AMI.

Chapter 2 focuses on the inter-institute reliability of IV-OCT to determine qualitative and quantitative parameters of atherosclerotic plaque. Consensus document guidelines have been published for IVUS and IV-OCT techniques in order to harmonize their use and analysis. Both technologies are increasingly used for the assessment of the natural history of atherosclerosis, vascular remodelling, and pharmacological and percutaneous interventions. Although one study underlines the necessity to centrally analyse IVUS data obtained in multi-centre studies, the evaluation of inter-institute reliability for IV-OCT is currently lacking. Accordingly, the purpose of our study was to investigate further inter- and intra-observer reproducibility, the inter-institute variability for IV-OCT (OFDI) quantitative and qualitative measurements vs. IVUS measurements using published consensus document definitions. In our work, we observed that in the measurement of lumen CSA, maximum and minimum lumen diameters, stent CSA, maximum and minimum stent diameters by analysts from 2 different laboratories, inter-institute reproducibility of OFDI was found to be more consistent than IVUS. Inter-institute agreement was substantial using both technologies for plaque composition.

Chapter 3 present 2 new robust hybrid intravascular imaging technologies developed in Dr. Tearney's laboratory i.e. OFDI-NIRS and OFDI-NIRAF, which may offer supplementary criteria for plaque vulnerability. Detecting vulnerable plaques in order to propose a preventive strategy is of major interest, i.e. local (mechanical or pharmacological) treatment of future culprit lesions or seeing a heart attack before it happens. First-in-human OFDI-NIRS imaging procedures are anticipated in the near future. First-in-human OFDI-NIRAF imaging procedures have been performed in a first pioneering series of 12 stable patients between July 2014 and January 2015. Findings of this pilot study showed that NIRAF was focally elevated in plaque locations where most high-risk morphologic phenotypes were evident. The contrast mechanism in NIRAF - tissue fluorescence is physically distinct from OCT - optical scattering and other modalities. The biochemical substrates of the NIRAF signal still have to be elucidated.